Zulhice MEHMEDI

Magnetic and Microwave Properties of Ba- and Sr- Hexaferrites Prepared by Solid State Reaction Route with Boron Addition

M.S.
2015

FATİH UNIVERSITY

The Graduate School of Sciences and Engineering

Master of Science in
Bio and Nano Technology Engineering Department

Magnetic and Microwave Properties of Ba- and Sr-Hexaferrites Prepared by Solid State Reaction Route with Boron Addition

by

Zulhice MEHMEDI

July 2015

Magnetic and Microwave Properties of Ba- and Sr- Hexaferrites Prepared by Solid State Reaction Route with Boron Addition

by

Zulhice MEHMEDI

A thesis submitted to

the Graduate School of Sciences and Engineering

of

Fatih University

in partial fulfillment of the requirements for the degree of

Master of Science

in

Bio and Nano Technology Engineering Department

July 2015
Istanbul, Turkey

APPROVAL PAGE

This is to certify that I have read this thesis written by Zulhice MEHMEDI and that in my opinion it is fully adequate, in scope and quality, as a thesis for the degree of Master of Science in Bio and Nano Technology Engineering Department.

_____
Prof. Abdülhadi BAYKAL
Thesis Supervisor

_____
Assoc. Prof. Hüseyin SÖZERİ
Co-Supervisor

I certify that this thesis satisfies all the requirements as a thesis for the degree of Master of Science in Bio and Nano Technology Engineering Department.

_____
Prof. Ayhan BOZKURT
Head of Department

Examining Committee Members

Prof. Abdülhadi BAYKAL _____

Assoc. Prof. Hüseyin SÖZERİ _____

Assoc. Prof. Uğur TOPAL _____

Prof. Bayram ÜNAL _____

Asst. Prof. Yakup BAKIŞ _____

It is approved that this thesis has been written in compliance with the formatting rules laid down by the Graduate School of Sciences and Engineering.

_____
Prof. Ayhan BOZKURT
Director

July 2015

MAGNETIC AND MICROWAVE PROPERTIES OF Ba- and Sr-HEXAFERRITES PREPARED BY SOLID STATE REACTION ROUTE WITH BORON ADDITION

Zulhice MEHMEDI

M.Sc. Thesis – Bio and Nano Technology Engineering
July 2015

Thesis Supervisor: Prof. Abdulhadi BAYKAL

Co-Supervisor: Assoc. Prof. Hüseyin SÖZERİ

ABSTRACT

The aim of this research is to investigate effect of boron addition on magnetic and microwave properties of $MFe_{12}O_{19}$ (M=Ba, Sr) hexaferrites. Several diavalent cations (Mn^{+2}, Zn^{+2}, Co^{+2}, Cu^{+2}, Mg^{+2}) were substituted to these hexaferrites to change ferromagnetic resonance frequency of the samples. Solid state reaction route was used during the study and 1 wt% B_2O_3 was added to initial mixture to improve the crystal growth at lower temperatures. Structural properties of the synthesized samples studied using XRD, SEM, FT-IR and magnetic properties determined using vibrating sample magnetometer. Microwave reflection/transmission measurements were done using network analyzer in waveguide or coaxial line in the frequency range of 0-26 GHz. NRW algorithm was used to obtain real and complex permeabilities and permittivities of samples. Then, reflection losses (RL) of samples were calculated using the standard formula.

Keywords: Radar Absorbing Material; Hexaferrites; Microwave Properties; Magnetic Properties, Reflection Loss

KATI HAL YÖNTEMLE SENTEZLENMİŞ BOR KATKILI Ba- VE Sr- HEKZAFERRİTLERIN MANYETİK VE MİKRODALGA ÖZELLİKLERİ

Zulhice MEHMEDI

Yüksek Lisans Tezi – Biyo ve Nano Teknoloji Mühendisliği
Temmuz 2015

Tez Danışmanı: Prof. Dr. Abdülhadi BAYKAL

Eş Danışman: Doç. Dr. Hüseyin SÖZERİ

ÖZ

Bu çalışmanın amacı bor katkısının M – tipi hekzaferitelerin ($MFe_{12}O_{19}$; M = Ba ve Sr) manyetik ve mikrodalga özelliklerine etkisini araştırmak. Numunelerin ferromanyetik rezonans frekanslarını değiştirmek amacıyla çeşitli divalent katyonlar (Mn^{+2}, Zn^{+2}, Co^{+2}, Cu^{+2}, Mg^{+2}) hekzaferrit yapılara katkılandı. Hekzaferritelerin sentezi için katı hal sentez yöntemi kullanıldı. Sentez karışımına, düşük sıcaklıklarda kristal yapı oluşumunu desteklemek için %1 B_2O_3 eklendi. Numunelerin yapısal değişiklikleri XRD, SEM/TEM, FT-IR cihazlarıyla, manyetik özellikleri ise VSM cihazıyla ölçüldü. Mikrodalga yansıma / geçirgenlik ölçümleri netvörk analizör cihazıyla dalga klavuzu ya da koaksiyal hat yardımıyla 0 – 26 GHz frekans aralığında ölçüldü. Elektriksel ve manyetik geçirgenlik katsayılarının gerçel ve kompleks bileşenlerinin hesaplanması için NRW algoritması kullanıldı. Yansıma kayıpları standart formül kullanılarak hesaplandı.

Anahtar Kelimeler: Radar Soğurucu Malzeme; Hekzaferritler; Mikrodalga Özellikler; Manyetik Özellikler; Yansıma Kayıpları.

To my mother

ACKNOWLEDGEMENTS

I express sincere appreciation to Prof. Abdülhadi BAYKAL, Assoc. Prof. Hüseyin SÖZERİ and Assoc. Prof. Hüseyin KAVAS for their guidance and insight throughout the research.

I especially would like to thank to Prof. Metin BALCI, Prof. Bayram ÜNAL, Assoc. Prof. Uğur TOPAL, Asst. Prof. Yakup BAKIŞ, Asst. Prof. Hüseyin SAĞKOL and Assoc. Prof. Mehmet ŞENEL their academic support and motivation.

I express my thanks and appreciation to my one and only, to my mother, for her understanding, motivation and patience.

Lastly, but in no sense the least, I am thankful to Fazilet GENÇ, İbrahim ÜNVER, Sercan TANRISEVEN, Hava CAN POLAT, Sinem ESİR, Duygu YAZICI, Ümran KURTAN and all other colleagues of mine and friends who made my stay at the university a memorable and valuable experience.

This thesis was supported by TUBITAK (the Scientific and Technological Research Council of Turkey) with Project number 213M174.

TABLE OF CONTENTS

LIST OF TABLES

TABLE

LIST OF FIGURES

FIGURE

LIST OF SYMBOLS AND ABBREVIATIONS

SYMBOL/ABBREVIATION	
(B)	Boron Added
BaM	Barium Hexaferrite
BM	Ball Milled
DUT	Device Under Test
EMW	Electromagnetic Wave
MW	Microwave
NRW	Nicolson – Ross – Weir Algorithm
PbM	Lead Hexaferrite
RCS	Radar Cross Section
RL	Reflection Loss
SrM	Strontium Hexaferrite
Zin	Incident Impedance

CHAPTER 1

INTRODUCTION

1.1 FERRITE THEORY

Interesting brain storming can be done for a thinker, student, inventor, researcher to think whether the electric field or the magnetic field is invented for the first time in history. Since almost all equations and descriptions lean on electrical field, a misconception arises among people that electrical field invented first. However, not the electricity but the magnetism is naturally found. First inventor of navigator was used the lodestone in Neolithic age to achieve his aim by means of magnetism. Lodestone is a natural iron-containing magnet. By deriving equations to identify electric and magnetic field, magnetic field, magnetism, became clearer theoretically and conseptionally. After first invention of magnet, no other element is found to be better than iron in magnetism. Iron is a special element for magnetism. For a material to be ferromagnetic, it should have a net magnetic dipole moment different than zero value. Net magnetic dipole is generated by spin moment of electrons. According to Hund's and Pauli rule, electrons in orbital disperse through to have maximum number of unpaired electron, after all available states are filled with unpaired electrons excess electrons placed to pair the unpaired ones. In order to have high magnetic moment, number of unpaired electron should be high. Orbital of d has highest number of available states for electrons, B group elements; and, highest number of unpaired electrons (in outer shell) belongs to Mn (d^5). Although main component of net magnetic dipole moment is number of unpaired electrons, exchange interaction, energy needed for exchange interaction takes important role for net magnetic dipole moment. One less unpaired electron belongs to Fe(d6) and ideal exchange interaction energy belongs to Fe

atom. Subsequently, Fe element has the highest magnetic net dipole moment; because, optimum values of both number of unpaired electrons and exchange interaction energy belongs to Fe. Since the strongest magnetic element is Fe, “ferromagnetics” are named by “ferrite”. Moreover, bohr magneton values, which represent the magnetization values of an elements, of transition metals which is mostly used as dopant are given as; Mn^{+2} 5 µB, Co^{+2} 3 µB, Ni^{+2} 2 µB, Cu^{+2} 1 µB, Zn^{+2} 0 µB. In addition, although zinc has no unpaired electrons, the element may have net magnetic dipole moment; because, constitutional deformation in zinc crystals causes to have a net dipole moment.

1.1.1 Crystal Classification

First magnetic material, the lodestone is basically iron-oxide. There are many types of iron oxides according to their functions, magnetic properties, physical and chemical structures. There are three different crystal types of ferrite: spinel, garnet and magnetoplumbite. Crystal classification is done according to ratio of Fe_2O_3 content to other metal oxides. Numeric representations of these ratios are stated in Table 1.1.

Table 1.1 Classification of ferrites by changes in the Fe_2O_3 – MeO modifier oxide ratios.

Spinel	Fe_2O_3	MeO = transition metal oxide
Garnet	$5Fe_2O_3$ - $3Me_2O_3$	Me_2O_3 = rare earth metal oxide
Magnetoplumbite	$6Fe_2O_3$ - MeO	MeO = divalent metal oxide from group II A - BaO, CaO, SrO

Spinel ferrites have cubic close-packed crystal structure, face centered cubic type (fcc). Bragg and Nishikawa first mentioned this type of crystal in 1915 (Bragg 1915; Nishikawa 1915). There are 64 sites available in tetrahedral sites, which is called A sites, and 32 available sites in octahedral one, called B sites (Carta, Casula et al. 2009). Cation doping into the structure provide several advantages, functionalities to the material. Response of the material to external magnetic field is generated by atoms of it; therefore,

any change in atom location or addition of atoms or absence atoms directly affects the magnetic characteristics of the whole material.

Garnet types of ferrites include rare earth ions like Pm, Sm Eu, Gd, etc. $Y_3Fe_5O_{12}$ (YIG) is the chemical formula of that kind. They are used in microwave applications due to their advantages; they work in below range of 1 to 2GHz (Durmuş 2013).

Magnetoplumbite ferrites are also known as M-type ferrites, hexaferrites. In 1930, Yogoro Kato and Takeshi Takei invented hexaferrites first. Hexaferrites, as they have the name, are hexagonal form of crystal structure which can be seen in Figure 1.1 in detail. In figure, octahedral sites are colored to red, tetrahedral sites are blue and trigonal bipyramidal sites are underlined with green color. Tetrahedral sites are blue and trigonal bipyramidal sites are underlined with green color. For barium hexaferrites, there are two BaM molecules for each hexagonal closed pack. Other than that, there are two types of unit cells, structural block, in hexaferrite crystal that are R=$BaFe_6O_{11}$ (Hexagonal) and S=Fe_6O_8 (Spinel) by combination of these blocks several types of hexaferrites are identified.

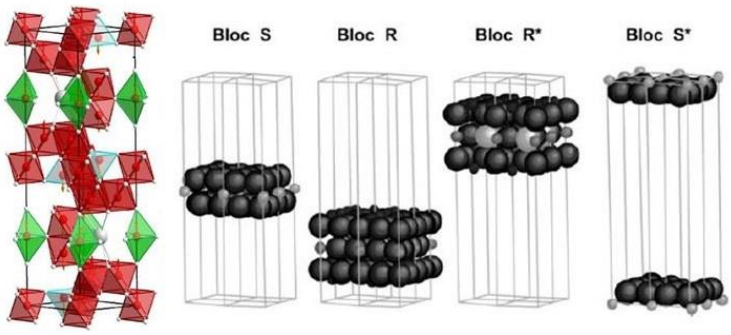

Figure 1.1 Crystal structure of hexafferite (Pullar 2012) .

Cation doping to that crystal structure can be preferable because of decreasing the resonance frequency down to the microwave region (Sözeri, Deligöz et al. 2014). In addition, cation doping affect the magnetic properties of the structure; because, the

orientation of magnetic anisotropy is influenced by cations and interactions between cations and other crystal structure elements (exchange, super-exchange interaction). Since microwave absorption properties are directly related to magnetic properties, cation doping manipulates not only the magnetic properties but also microwave absorption properties (Okamoto 2009). In order to have differences in magnetic and microwave absorption properties, doped elements should replace with an element which is in the crystal structure. For example, Ti, Ni and Co ions prefer to locate octahedral sites of the crystal structure and Mg ions prefer to replace with Fe ions in tetrahedral sites (Iqbal, Ashiq et al. 2009; Soman, Nanoti et al. 2013). Different doping results different manipulations on magnetic and microwave absorption properties.

Hexaferrites are used in many different areas due to their unique properties such as they have low hysterical loss, high coercivity, they are insulator, they have low reflection microwave losses, light in weight and ease on handling, very large working area, region of frequencies, they can be synthesized with so many different routes, they are chemically stable and they have corrosion resistance and with other advantages of hexaferrites, they are so much popular in several areas. For instance, hexaferrites can be used as magnetic core for inductors/coils; magnetic memories also use hard magnetic characteristic of hexaferrites. In addition, some kind of modern electronic devices need to have biased magnets in them; since the hexaferrites can be used as self-biased and low microwave loss magnets, for these types of usage areas are willing to have the hexaferrites to be embedded in (Sözeri, Mehmedi et al. 2015). Moreover, defense industries are also use magnetoplumbite ferrites to shield the radar, i. e. to build invisible, stealth and low observable devices (eg. F117 Nighthawk aircraft). M type hexaferrites are widely used in industry, in science so on so forth, detailed classification and representation of these areas are shown in Figure 1.2.

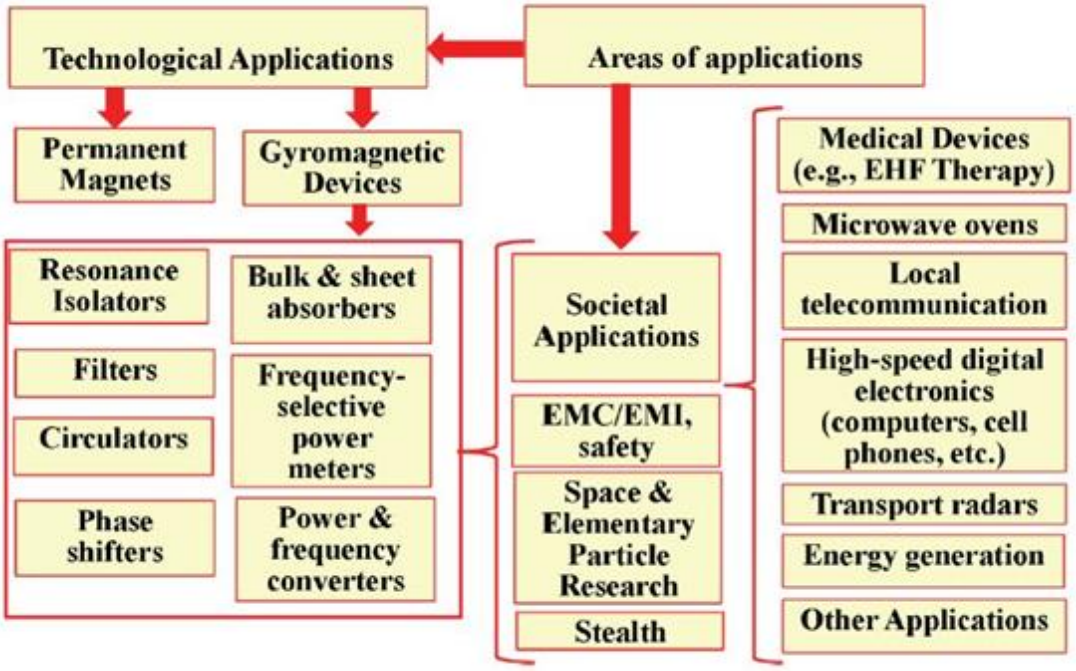

Figure 1.2 Usage areas of hexaferrites (Pullar 2012).

1.1.2 Magnetic Classification

Another classification can be done according to magnetic properties of ferrites. In order to classify ferrites by their magnetic properties, hysteresis loops data will be commented. Hysteresis loops reflect several magnetic properties of the material. For instance, coercivity of a material is shown in its hysteresis loop. Coercive force is the measure of resistance of a ferromagnetic material to external field without demagnetization. Depend on this parameter; the material can be classified as hard or soft magnets. Larger the coercivity magnetically harder the material, this classification is visually represented in Figure 1.3. Magnetically hard means the ferromagnetic material resistance to external magnetic field is high. Moreover, by the slope of hysteresis loops, one can determine the type of magnetic material.

There are three main types of magnetic materials. They are classified as diamagnetic, paramagnetic and ferromagnetic materials. Diamagnets reply to applied external field by aligning to the opposite direction of external field, which means they do not show magnetism. In other word, when you apply a certain value of H you will get less than that of value as B, that leads us to have permeability less that one. Paramagnets have only magnetism under external magnetic field. They only orient because of external magnetic field. So, you get B value same as you apply, the H value which has a slope of around one. In ferromagnetic case, spins affect each other, and after applying external field, it is observed that the material has magnetism, that means all spins are aligned to the external field direction and these spins are correlated with each other so that, after external magnetic field they survive as they were aligned. Additional to applied external magnetic field, aligned spins contribute; therefore, for permeability value we should have more than one. In some cases (eg. Hexaferrites/M-type ferrites), one can observe 10^5 multiplication of H comparing to the B.

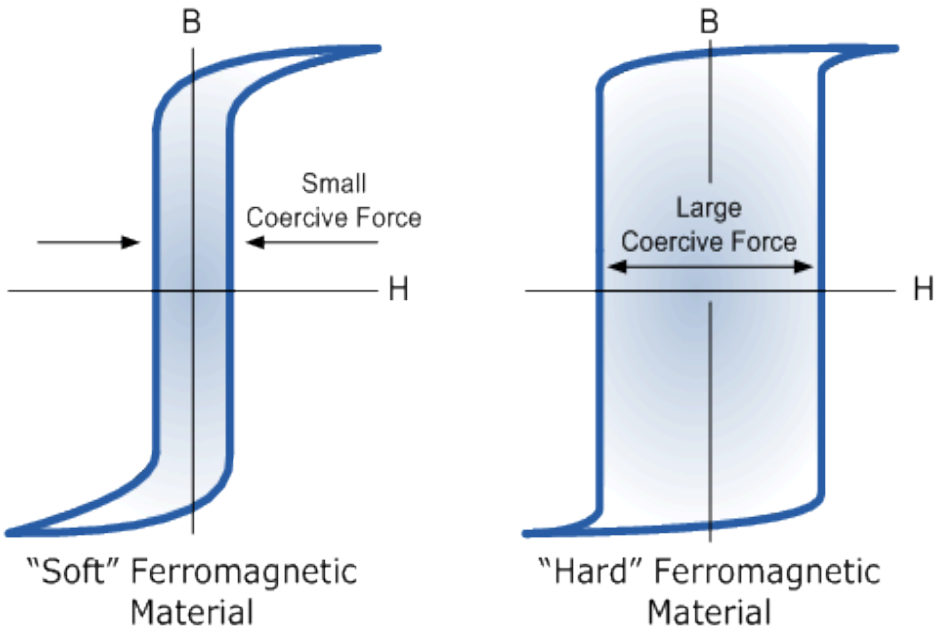

Figure 1.3 Magnetic classification via hysteresis loops (Durmuş 2013).

1.1.3 Exchange-Super Exchange Interaction

Once a material is exposed to an external magnetic field, all surface spins are affected according to that applied field directly. However, external magnetic field does not penetrate itself to inner regions. Effect of external magnetic field is carried into the material by means of material's spins. Exchange interaction term is defined for this situation. There are some sorts of exchange interactions, such as direct-exchange interactions, indirect-exchange interactions and super-exchange interaction. Direct exchange interaction refers to direct effect of spins to each other. If two spins are close enough they are effected directly from each other; for instance, if two spins are oriented parallel, they will repel each other according to Pauli principle and this interaction will be called as negative exchange interaction; on the other hand, if two spins are oriented antiparallel, they will attract each other called positive exchange interaction. If two spins are not close each other enough, i.e. there are some space or another type of spins in between, they will be interacted through that spins in between and that interaction will be called as indirect exchange interaction. Super exchange interaction is interaction of two spins through diatomic anion. Exchange interaction types affect microwave and magnetic properties directly (Kneller and Hawig 1991; Maeda, Sugimoto et al. 2004; Shen, Song et al. 2015).

1.2 RADAR ABSORBER MATERIAL DESIGN THEORY

1.2.1 Theory and Methods

In radar absorbing technology fundamental aim is the fact that incident electromagnetic wave (EMW) should neither reflect back to the source nor transmit through the material. Incident electromagnetic wave absorption should occur through the radar absorbing material (RAM).

There are two main ways to absorb the incident EMW. One is to absorb by means of characterization properties of the filling material. There are three main characterization parameters of a RAM that absorbs the EMW, ferromagnetic resonance, magnetic properties and dielectric properties. Ferromagnetic resonance is similar to all other types of resonances. A spin rotates in a frequency, if an incident EMW with same frequency meet that spin, spin rotation is supplied by that energy; hence, the incident EMW energy is

absorbed by that way. That magnetic property is called as spin rotation. Since the spin rotation frequencies are high, MW absorption peaks in high frequencies is commented that due to spin rotation. Lower frequency absorption can be altered by domains that slide on each other. All domains have their own net magnetic moment, in junction points of these domains, resonance of ferromagnetism occur. Since the domain size is larger than the spin, the resonance which is due to domain sliding, should have lower frequency Therefore, lower frequency MW absorption is due to domain wall motion.

Other type of absorbing is to absorb EMW mechanically. It is classified as follows.

In order to define the area on RAM that incident radar wave interact, a term is used: Radar Cross Section (RCS). "RCS is a measure of how detectable an object is with radar." In order to reduce RCS, two basic theoretical obligation should by matched by RAM.

First of all, reflection coefficient should decrease to decrease RCS. Impedance (Z) is closely related with reflection coefficient; therefore, impedance of the material is one of the fundamental parameters for a material to be criticized as a RAM. Desirable behavior for EMW in RAM is to be same as in the air. In other word, impedance of RAM should be equal to the one of the airs, as perfect condition; or, impedance of RAM should be close to the value of air impedance which is 377 ohms.

Second obligation is about parameters that responsible for absorbing the incident EMW are ε''and μ''; they absorbs magnetic component of EMW and electric component of EMW respectively. These parameters should be decreased to have high absorption. Moreover; these two parameters should be decreased simultaneously. Otherwise, in the case of one component of EMW is decreased and other one is not, according to Maxwell equations and Lenz rule, non-decrease component of EMW is multiplied. Therefore, for this situation it cannot be said absorbing of EMW is reached. In other words, this obligation, as other one, is crucial for absorbing EMW.

1.2.2 Radar Absorber Classifications and Types

Radar absorbing materials are designed according to demand. Therefore, classification of them is hard to make. In order to make easier to get the main conception of RAMs and understand main approaches to that field, two main classifications are highly convenient. First classification is based on working principles of RAMs. Second one is branched due to working band range. First classification enable us to get inner understanding of working principles of RAMs, second one rearrange same fundamental examples of RAMs according to frequency ranges which makes us to have an idea of application areas of fundamental examples.

1.2.2.1 Classification 1: Absorbing Behavior Classification

1.2.2.1.1 Impedance matching absorbers

As it is mentioned in previous parts, reflection coefficient is directly related with impedance of surface. Actually, it is also understandable and explainable not only theoretical view, but also it is possible through practical view: EMW travel through material, this travel is directly oriented by nothing else but materials electric and magnetic permition to travel of incoming electrical and magnetic media; this permition, in a way, can be said analog to the impedance.

1.2.2.1.1.1 Pyramidal absorbers

These types of absorbers are preferred populously for commercial purposes nowadays. They have basically pyramidal shape. Geometry of these types of absorbers provides large surface area to incident EMW to reduce RCS. In addition, pyramidal absorbers can absorb incident EMW not only by characteristic property but also by geometry. By adjusting the height, distance between pyramids, thickness and frequency certain wavelength can be omitted due to geometric specifications of these absorbers. Pyramidal absorbers are made up of polymer substances, generally polyurethane. Sponge, porous structure of the polymer can be filled by matching absorber material in order to have broadened band of absorbing and reduce RCS on some other region of wavelength.

Sponged structure can be manipulated to a fixed shape to have further improving performance of absorber (Liu, Drew et al. 2012).

1.2.2.1.1.2 Tapered Layer Absorbers

One cannot achieve satisfying results just by using ultrahigh performance material. High absorbance value of a material does not mean that you can use it in any form and any design with full performance; in practical life, material which has high absorbance value may not absorb EMW. Incident EMW cannot be absorbed directly by an absorber; it can be reflected as it is due to high absorbance value of absorber material. In order to overcome this problem, different absorbance, impedance valued materials can be used by arranged from the least value to the highest value of impedance. Tapered design of different impedance valued of absorbers enable incident EMW to go through absorber material easily.

1.2.2.1.1.3 Matching Layer Absorber

Matching layer absorbers can be called improved version of Tapered Layer Absorbers. By adding "matching thickness" property to tapered layer absorbers, it can be got matching layer absorbers.

1.2.2.1.2 Resonant absorbers

Resonant absorber basic working principle leans on wave characteristics. First RAM design is history is also an example of this type of absorber. By using the advantage of "constructive interference" phenomena, first RAM design is basically consist of d=ʎ/4 spaced metal-RAM powdered plate or curtain (it is called as Salisbury curtain)(Pullar 2012). Incident EMW is faced with ʎ/4 gap to the metal substrate and omitted with reflection of EMW from metal substrate, since ʎ/4 inverse of a wave and the original wave summation results nothing. Omitting of these waves, in this example omitting a wave itself by reflection from metal substrate, is called constructive interference.

1.2.2.1.2.1 Salisbury Screen

EMW has maximum value of its electric component at lambda over 4 away from a reflected substrate. At this distance, if one has a dielectric absorber screen, can get maximum absorbance. Salisbury Screen works over this idea. Since magnetic component has maximum value on the surface of substrate layer, Salisbury Screen has deficiency to absorb magnetic component of EMW. In order to get improved performance of Salisbury Screen, Dallenbach layer should be concerned.

1.2.2.1.2.2 Dallenbach Layer

Dallenbach layer cancels the deficiency of Salisbury screen by magnetic absorbance material. From very beginning of substrate surface absorber material enables absorbance of not only electric component of EMW but also magnetic component is absorbed by this way.

1.2.1.2.3 Jaumann absorber

Jaumann layer is invented in 1943. This kind of absorber consists of two low loss dielectric sheets with a distance in between. It is very like as Salisbury screen with one more additional screen (simpler version of Salisbury). Two absorbance area increases the total absorbance. Resistive sheet addition provides larger bandwidth in absorbance. On the other hand, this kind of absorber is lead to physical disadvantages; more components need more design and calculation, volume, weight and money.

1.2.2.2 Classification 2: Absorbing Range Classification

Radar absorbers are conflict in classification. According to classification parameter million types of classifications can be done. Working principle and the absorbance range of absorbers are two major fundamentals; therefore, these two major parameter-classifications should be mentioned even the absorber types are same. Since, it is mentioned in the previous section the working principle of main absorbers, only the names will be classified in this section.

1.2.2.2.1 Broadband Absorber

Absorbers can be got several features by mechanical design only. In addition, chemical improvement and additional properties also can make different aspect. For an absorber one of the most important properties is having broadband absorber range. By several ways bandwidth of absorbance can be enlarged; for instance, adding one more resistive sheet to the absorber system to improve the efficacy (Jaumann), etc. Names of broadband absorbers are listed below:

Jaumann

Inhomogenous absorber

Geometric transitions absorber

Bulk absorbers

Low density absorber

Chiral absorber

1.2.2.2.2 Narrowband Absorber

Salisbury screen

Magnetic absorber

Dallenbach layer

Circuit analog RAM

1.3 SYNTHESIS METHODS of RADAR ABSORBING MATERIALS

Hexaferrite synthesis is much more complex and difficult comparing to spiner ferrites due to their high atom content, large unit cell; in addition, in one hexaferrite unit cell there are also another types of unit cells like cubic ones. Proposed mechanism of hexaferrite synthesis is that cubic block of a spinel ferrite is self-assembled first and then by this core hexagonal unit cell begins to be formed; taking account many critical properties of synthesis reactions and as a final product, the hexaferrite, synthesis routes can be improved (Liu, Drew et al. 2012). There are several synthesis methods of hexaferrite particles there

are disadvantages and advantages of them. This section will cover widely-used synthesis methods and their bringing.

1.3.1 Sol-Gel Auto-combustion Method

Experimental route of this method is as follows, additional to main chemicals (like Ba/Fe-contain chemicals), and mostly citric acid is added to the reaction medium as a fuel of reaction. Solution of mixture is prepared in a fixed pH value and heated, solvent evaporates, solution becomes gel form in this step; afterwards, drying process continues and by the help of fuel mixture getting hot, product is synthesized by this way of route (Mu, Chen et al. 2008). After all, annealing of products (approximately at 1000°C) are done to have ready to use product and more stable chemical compounds at the end. This method can be classified in chemical synthesis methods; i.e. , synthesis carries on a more controlled way, smaller particle size of product can be got comparing to solid state synthesis method. Although chemical ways are more controlled and in low temperature process they are, chemicals' handling and reaction setup conditions are not cheap and practical comparing to solid state reaction methods.

1.3.2 Co-precipitation Method

This method is used from the years of 1960s (Pullar 2012). As another chemical synthesis method, Co-precipitation method carry on in a wet chemistry way, salts of main containing chemicals reacts with a base (mostly NaOH) and precipitation occurs. Precipitation and drying maintains at fixed pH and precipitation media is ionic. Drying process is held on approximately 100°C and annealing process needs 1000°C (Iqbal, Ashiq et al. 2009). For almost all chemical synthesis methods, non-stoichiometric ratio of Ba/Fe or Sr/Fe etc. is needed (Pullar 2012).

1.3.3 Hydrothermal Method

Third chemical synthesis method is hydrothermal method. In this method reaction maintains under pressure in autoclave. As reaction medium is in controlled pressure, temperature of reaction is not high (approximately 100°C -300°C) (Drofenik, Ban et al. 2011). In order to indicate the disadvantages of this method, addition to be a chemical

reaction, extra instrument is needed as autoclave. On the other hand, since the reaction media is under high control of pressure, chemically manipulations can be easily done to have desired features for products. For instance, non-stoichiometric ratio of Ba/Fe or Sr/Fe leads to have nanoparticles (Pullar 2012).

1.3.4 Solid State Method

This method is preferred especially by commercial uses because of ease of preparation steps of reaction. All oxides of ingredients are mixed in a mortar in ethanol media and then this mixing is let to dry in room temperature, powder mixing pelletized under optimized pressure, pellets are put in an oven approximately 1000°C for approximately 2 hours. After this procedure, final product is mortared to get powdered form. Beside other methods of synthesis, solid state method is more applicable for large amount of particle in more practic(al) way. Moreover, comparing to chemical methods, that kind of synthesis is preferred in commercial manufacture; because, less types and amount of chemicals and devices are used in that method (Mehmedi et al. 2014).

In order to have more efficient yield by solid state method, boron addition was investigated (Topal 2011). Boron inhibits the growth of crystal at low temperatures. B_2O_3 is melted approximately at 200°C and supply more homogeneous medium for the powder mixture to make easy hexaferrite crystal to be grown. Boron addition improves magnetic properties of barium hexaferrite crystal. Optimum boron addition percentage was also investigated by many ways in literature (Topal 2011, Sözeri, Baykal et al. 2012, Topal 2012).

CHAPTER 2

EXPERIMENTAL

2.1 MATERIALS

Starting chemicals are as follows, barium carbonate ($BaCO_3$), iron (III) oxide (Fe_2O_3), magnesium oxide (MgO), manganese(II) oxide (MnO), cobalt(II) oxide (CoO), nickel(II) oxide (NiO), copper(II) oxide (CuO), zinc(II) oxide (ZnO), lead oxide (PbO), titanium dioxide (TiO_2) and boron trioxide (B_2O_3) and ethanol (C_2H_5OH). They are obtained from PI-KEM, Reade International, Alfa and Sigma Aldrich and used as received without further purification.

2.2 INSTRUMENTATIONS

2.2.1 X-Ray Powder Diffraction (XRD)

The structural properties and fractions of different phases of the samples were investigated using a Rigaku Smart Lab operated at 40 kV and 35 mA using Cu Kα radiation (λ = 1.54059 Å). Powder X-ray diffraction data were used to analyze phase investigation, lattice parameter and average crystallite size of BaM and SrM samples.

2.2.2 Scanning Electron Microscopy (SEM)

The surface morphology and microstructure of the samples were examined with a scanning electron microscope (JEOL6335F, Field Emission Gun).

2.2.3 Vibrating Sample Magnetometer (VSM)

The magnetic characterization of the samples was performed at room temperature using a vibrating sample magnetometer (LDJ Electronics Inc.,Model 9600) in an applied field of 15kOe.

Figure 2.1 LDJ Electronics Inc.,Model 9600 VSM Instrument.

2.2.4 Network Analyzer

MW analyses are done by Agilent, E8364B PNA model Network Analyzer (10 MHz to 50 GHz [Obsolete]).

Network Analyzer instrument sends electromagnetic wave to the sample and take the feedback of the sample in electromagnetic wave unit it sends, by this way, indicating the incident and reflected waves, one can express how much of electromagnetic wave is absorbed. Working principle of network analyzer is also seen in Figure 2.3; MW is

generated by source and it goes through DUT, reflected, incident and transmitted waves are operated and calculated to get scattering parameters (S parameters).

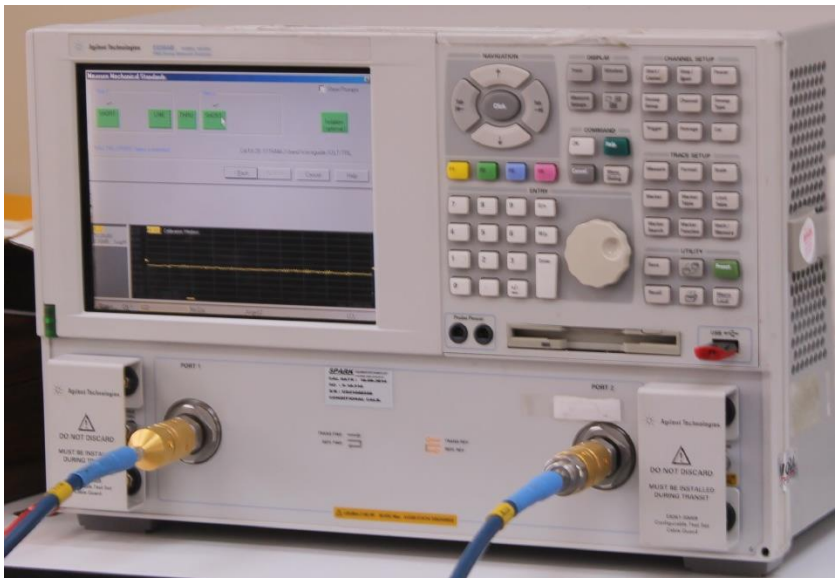

Figure 2.2 Agilent, E8364B PNA model Network Analyzer Instrument.

S parameters describe electrical behavior of path of any electrical networks. For instance S_{12} describes the scattering parameter which is got by port 1 source of this EMW is port 2. Other S parameters are shown in Figure 2.4.

There are complex handling hardware and software of this instrument since very large range of frequency of electromagnetic waves can be send and detected. Detected S parameters is not end of analysis, to get more precious parameters are μ(permeability) μ' (real part of permeability), μ''(imaginary part of permeability), ε(permittivity), ε' (real part of permittivity), ε'' (imaginary part of permittivity) and to calculate these parameters complex algorithms and expensive software are needed; semi-embedded hardware parts of instrument is so sensitive, waveguides are so responsive and have high-end prices.

Reflection loss of a material can also be calculated and commented by ε and μ with both their real and imaginary parts.

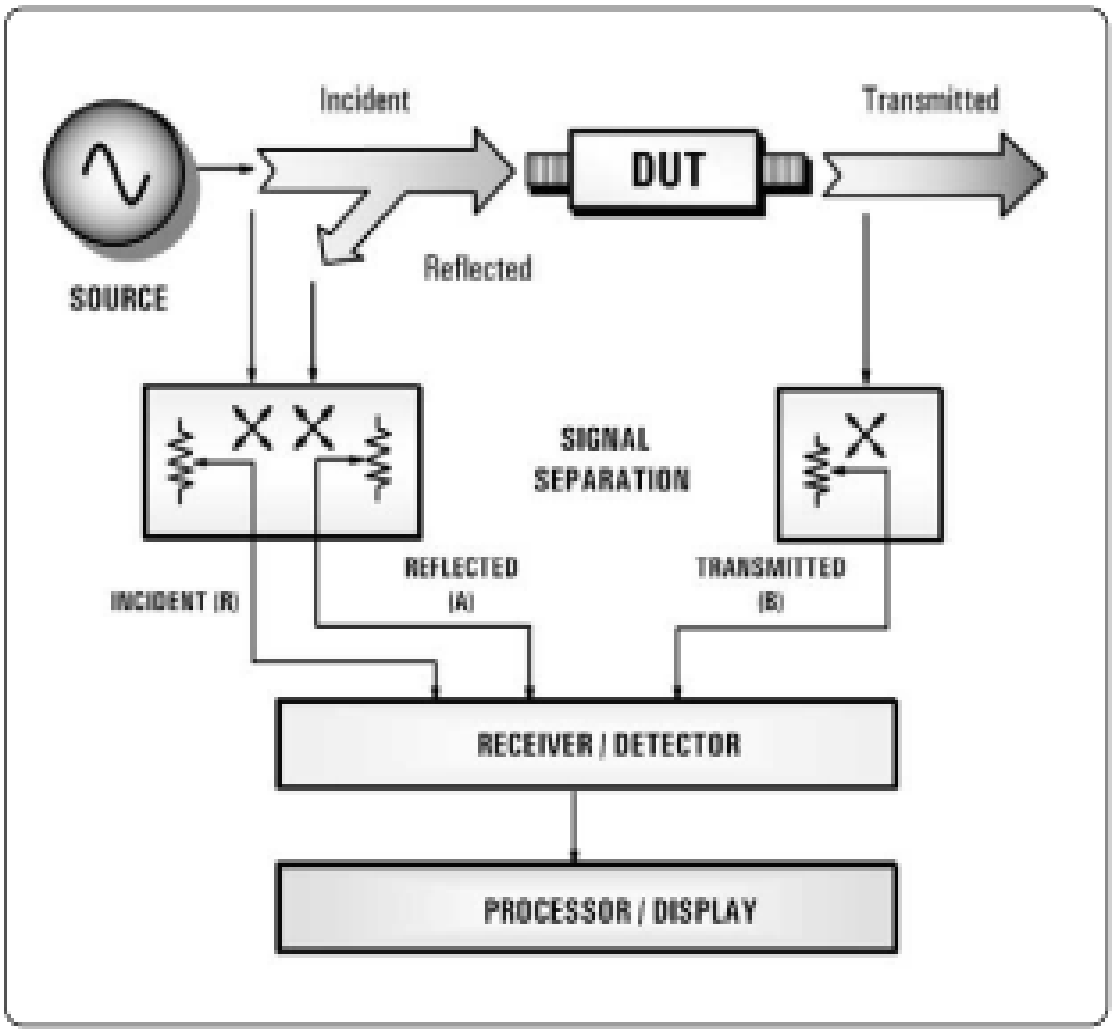

Figure 2.3 Block diagram of Network Analyzer.

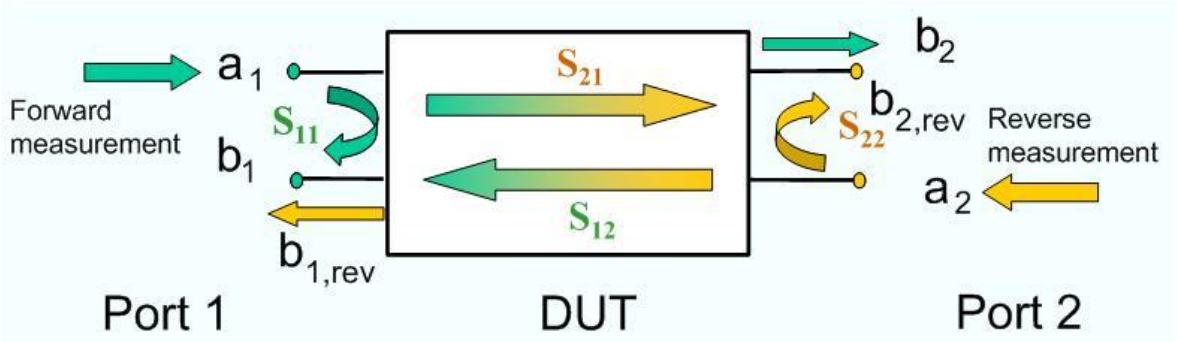

Figure 2.4 S parameters in network analyzer.

2.2.5 Ball Milling

In this study, Fritsch planetary micro mill Pulverisette 7 premium line ball mill instrument is used.

2.2.6 Furnace

Annealing processes done by Carbolite RHF 1400 model furnace.

2.3 SYNTHESIS of HEXAFERRITES

For the solid state reaction of X (Mn, Co, Ni, Cu, Zn), Pb, $BaCO_3$, Fe_2O_3 and B_2O_3 to form doped $BaFe_{12}O_{19}$, powders, ingredients were weighted stochiometrically. In addition, for boron-substituted samples, B_2O_3 1 wt % was added. Then, all powders were grounded and grinded all together in an agate mortar, first in solid phase then in ethanol for 15 min. The powder mixture was pelletized with 200 MPa pressure. Pellets were heat treated at temperatures between 800 and 1200°C for 2 hrs.

2. 4 PELLETING AND BALL MILLING PROCEDURE

2.4.1 Pelleting for Network Analyzer (MW Absorption Analysis)

In Figure 2.5, toroidal shape of pellet and its dye for MW absorption analysis is shown, different shapes of pellets are prepared by means of unique dyes, powder mixtures were pelletized under 1 ton pressure. Pellets that are rectangular shaped are used for the range of [18, 26.5] GHz (K band); toroidal shaped of pellets are used for the range from 10 MHz to 18 GHz.

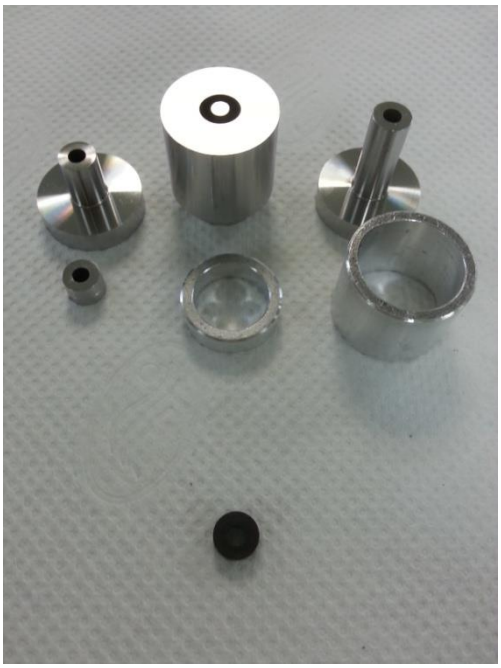

Figure 2.5 Toroidal shaped pellets and dye components.

2.4.2 Ball Milling

Optimized program of ball mill for this study is 900 rpm 4 cycles 15 minute breaks 1mm zirconium balls are used. Particle size distribution decreased from 1mm to 5-10 μm by this mode of ball mill instrument.

CHAPTER 3

RESULTS and DISCUSSION

3.1 SYNTHESIS OF BORON ADDED STRONTIUM HEXAFERRITE BY SOLID STATE METHOD AT DIFFERENT TEMPERATURE

3.1.1 XRD Analysis

As it is seen in Table 3.1, temperature promotes the hexaferrite formation. As temperature increasing, hexaferrite phase dominates. For both barium and strontium hexaferrite, 1000 °C is optimum temperature for hexaferrite formation. Boron addition to barium media decreases the annealing temperature for dominated hexaferrite phase. On the other hand, in strontium case, boron takes role to increase the ratio of hexaferrite phase comparing to other one. Moreover, boron addition prevents mono ferrite occurrence as a second phase in barium hexaferrite.

Phase ratio of both BaM and SrM samples were calculated by reference intensity ratio (RIR) method (PDXL, Rigaku, Japan) (Bish and Howard 1988) (Table 3.1).

Lattice parameters (a, c) of both BaM and SrM samples (Table 3.2) is calculated by following equation (Thompson and Evans 1993; Mariño-Castellanos, Somarriba-Jarque et al. 2005)

$$\frac{1}{d^2} = \frac{4}{3} * \frac{h^2 + hk + k^2}{a^2} + \frac{l^2}{c^2}$$

By fitted six peaks of XRD data and Eq. (1) (Wejrzanowski, Pielaszek et al. 2006) average crystallite size, D_{XRD}, and standard deviations σ are calculated (Figure 3.3 and Table 3.2). Line profile was fitted through six peaks with following Miller indices:

for BaM: (305) (214) (610) (110) (610) (325); for SrM: (300) (220) (612) (104) (610) (404). All data has same value of standard deviation σ, which is (±) 1nm. Both fitted and experimental profiles of XRD data are shown in Figure 3.1 and Figure 3.2.

Table 3.1 Phase ratio of BaM and SrM

Temperature (°C)		800	900	1000	1100	1200
Pure	BaM	-	72	97	100	100
	Fe_2O_3	73	27	2.8	0.3	0
	$BaFeO_3$	27.4	1.6			
1 wt% B_2O_3	BaM	84	93	95	96	98.4
	Fe_2O_3	15.9	7	5	4	1.6
Pure	SrM	37	67	84	92	97
	Fe_2O_3	63	33	3+13	8	2.9
1 wt% B_2O_3	SrM	0	54	89	89	99
	Fe_2O_3	100	46	11	10.7	1.03

BaM samples prepared with boron addition and sintered at temperatures between 800 and 900 have exactly the same lattice parameters with the one sintered at 1000 °C. This means that crystal structure of the BaM was formed at temperatures as low as 800 °C with boron addition. The lattice parameters of both hexaferrites are exactly the same with the pure and boron added samples, as seen in Table 3.2.

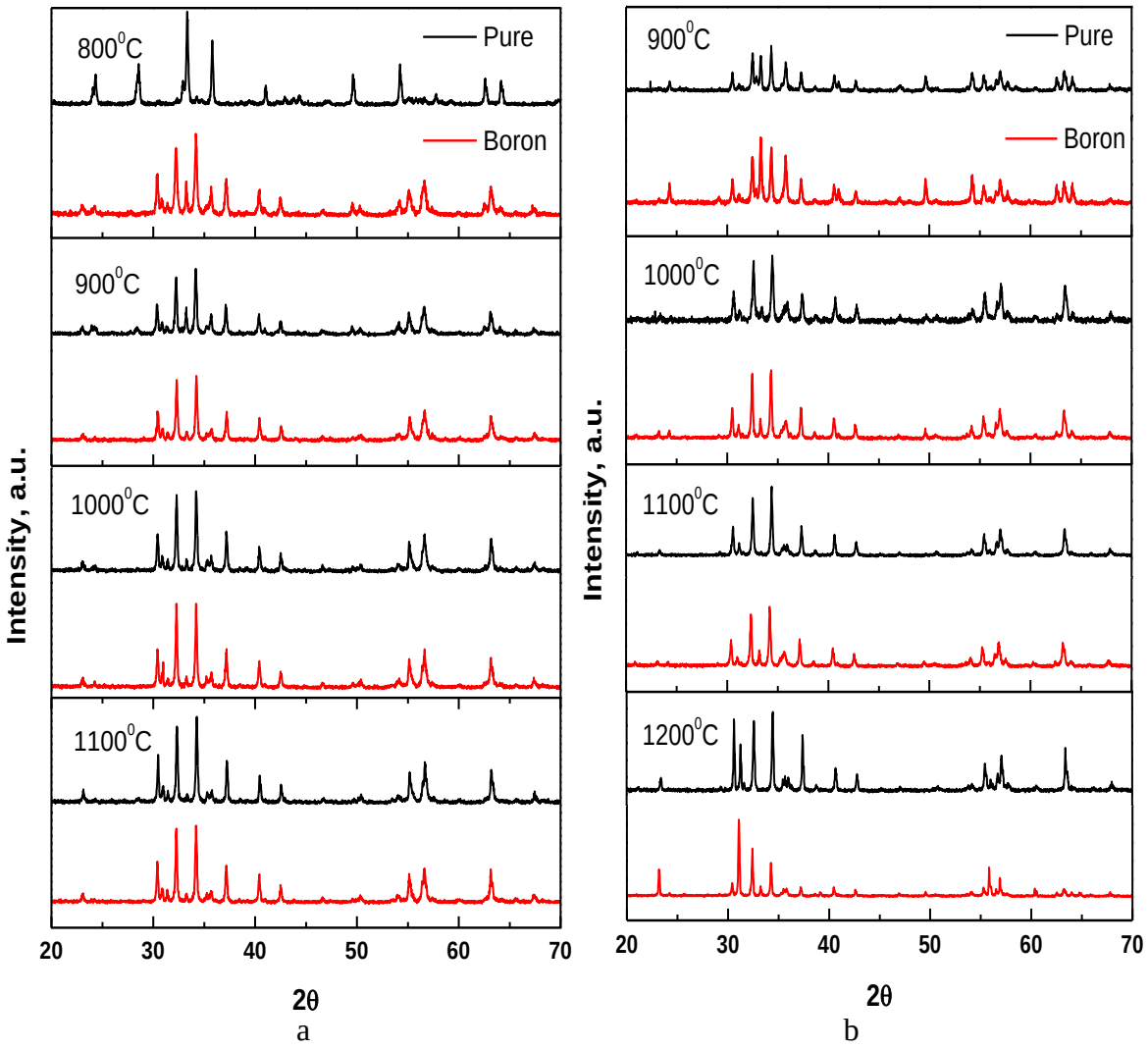

Figure 3.1 XRD patterns of a) BaM, b) SrM prepared by with and without boron addition.

It is well-known fact that the higher temperature makes the bigger crystallite size (Solanki, Packiaraj et al. 2014). Crystallite grows by energy; in this study, temperature supplies this energy for the medium to have bigger crystallite particles, comparing to lower degrees of temperature that is also seen in Figure 3.3. As seen from the figure, crystallite grows sharply with temperature. Fitted curve reveals that there is a quadratic relation between crystallite size and annealing temperature.

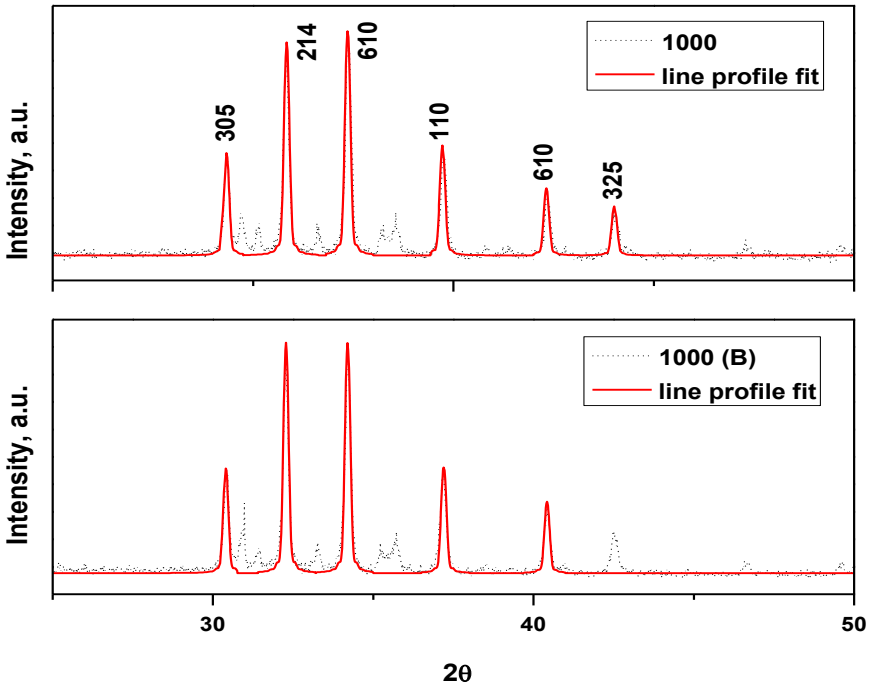

a

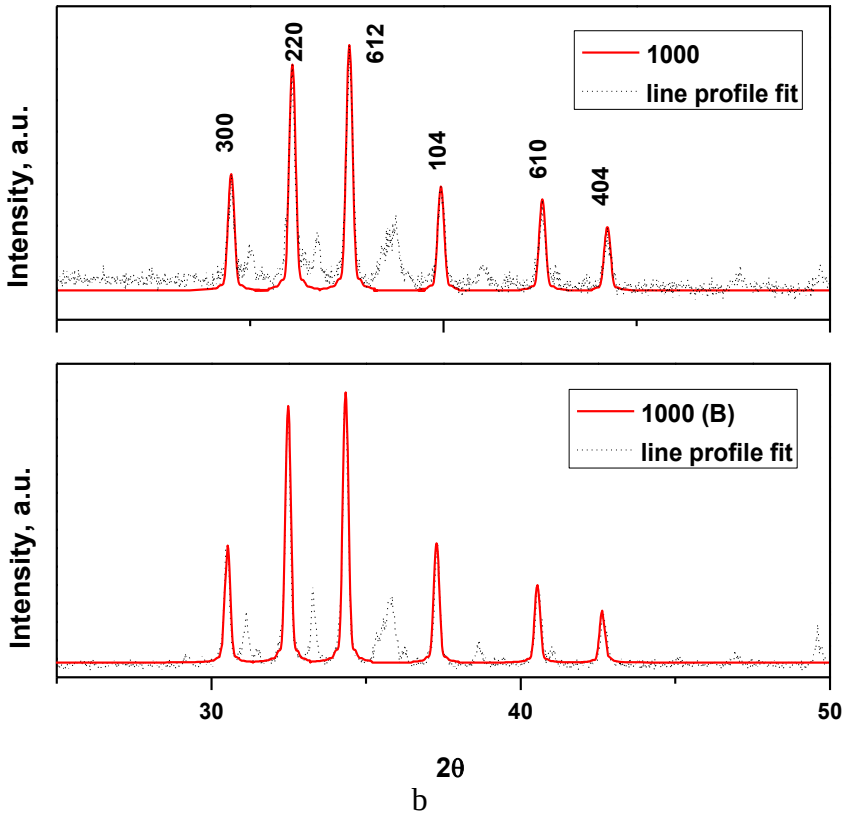

b

Figure 3.2 Experimentally measured and theoretically line profile fitted XRD patterns of a) BaM, b) SrM.

Table 3.2 Lattice parameters of BaM and SrM samples sintered at 1000°C.

	BaM 1000	BaM 1000B	SrM 1000	SrM 1000B
a (Å)	5,893	5,893	5,882	5,882
c (Å)	22,942	22,942	22,942	22,942

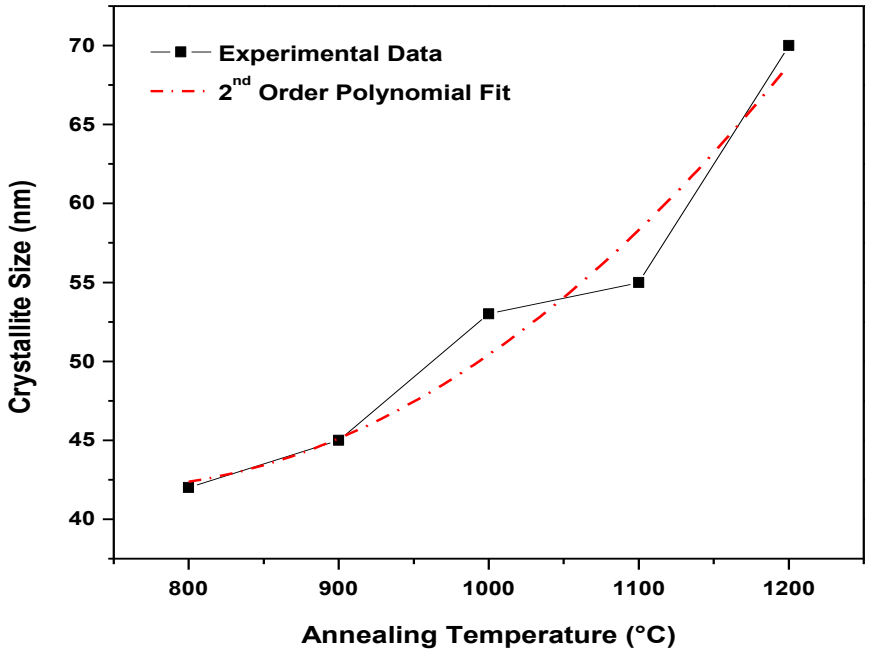

Figure 3.3 Crystallite size of BaM with boron substitution according to temperature.

3.1.2 VSM Analysis

Figure 3.4 shows magnetic hysteresis curves (M-H) of pure and boron added SrM and BaM samples synthesized at different temperatures between 800 and 1200°C. as Table 3.3 shows, magnetic parameters, both Ms and Hc, is very close to each other in the pure and boron added SrM samples in the sintering temperatures between 900 and 1100°C. Sintering

at 1200°C destroys grain boundaries and causes melting of powders, as seen in Figure 3.4, while pure sample has a coercivitiy of 2.4 kOe. Thus, soft ferromagnetic behavior appears in boron containing SrM sample. The pure BaM sample sintered at 800°C has almost no magnetization indicating that hard ferromagnetic phase was not formed at this temperature. However, boron containing sample has quite high magnetization (~ M_s= 50 emu/g) and coercivity of higher than 1 kOe, which reveals that $BaFe_{12}O_{19}$ phase was formed successfully as a major phase. At higher temperatures, saturation magnetization of the boron added samples are again higher compared to pure samples, see Figure 3.5. Coercivities of the both types of BaM have very similar trends with increasing sintering temperature. In pure sample, Hc first increases up to 1100°C then starts to decrease at higher temperatures. In the boron containing sample this decrease occurs at 1000°C and indicates that mechanism of magnetization changes from single to multi domain like, which was reported to occur when grain size exceeds 1 μm (Zhong, Ding et al. 1997; Xu, Ma et al. 2006; Li, Wang et al. 2009).

During the synthesis of hexaferrites, independent of the preparation technique followed, usually certain amount of barium/strontium surplus is used to eliminate α-Fe_2O_3 phase (Zhong, Ding et al. 1997; Mali and Ataie 2005; Xu, Ma et al. 2006; Li, Wang et al. 2009). The optimal Fe/(Ba,Sr) molar ratio depends on the preparation method and it may vary in a wide range. For instance, it is reported as for co-precipitation (Janasi, Rodrigues et al. 2000), in the hydrothermal (Liu, Wang et al. 1999; Pullar 2012) and sol-gel (Sözeri, Durmuş et al. 2012), in the ammonium nitrate melt methods (Sözeri, Küçük et al. 2011). Liu et al. (Liu and Wu 2001) observed that when Fe/Ba is 2.28, magnetic properties of BaM thin films were better in the sol-gel route. During the ammonium nitrate melt route, Fe/Ba = 2 lead to the highest Ms and Hc values in BaM. When low Fe/Ba ratios (<10) are used another impurity phase ($BaFe_2O_4$) inevitably appears and decreases the fraction of hard phase leading to low Ms values. Fortunately, this mono ferrite phase can be removed with etching the powders in diluted HCl (Sürig, Hempel et al. 1996; Liu and Wu 2001; Sözeri, Küçük et al. 2011). Therefore, we tried to determine optimal Fe/Ba,Sr molar ratios between 10 and 12, when standard ceramic method is used together with %1 B_2O_3 catalyst. As Fe/Sr ratio increases coercivity has an increasing tendency with some fluctuations. It is

3.2 kOe when Fe/Sr =10 and 4.kOe if Fe/Sr molar ratio is 12. As seen in Figure 3.6, the saturation magnetization decreases from 57.5 to 53 emu/g with increasing Fe/Sr molar ratio until it reaches to 11.5. Then, it sharply increases to 58.5 at Fe/Sr = 12.

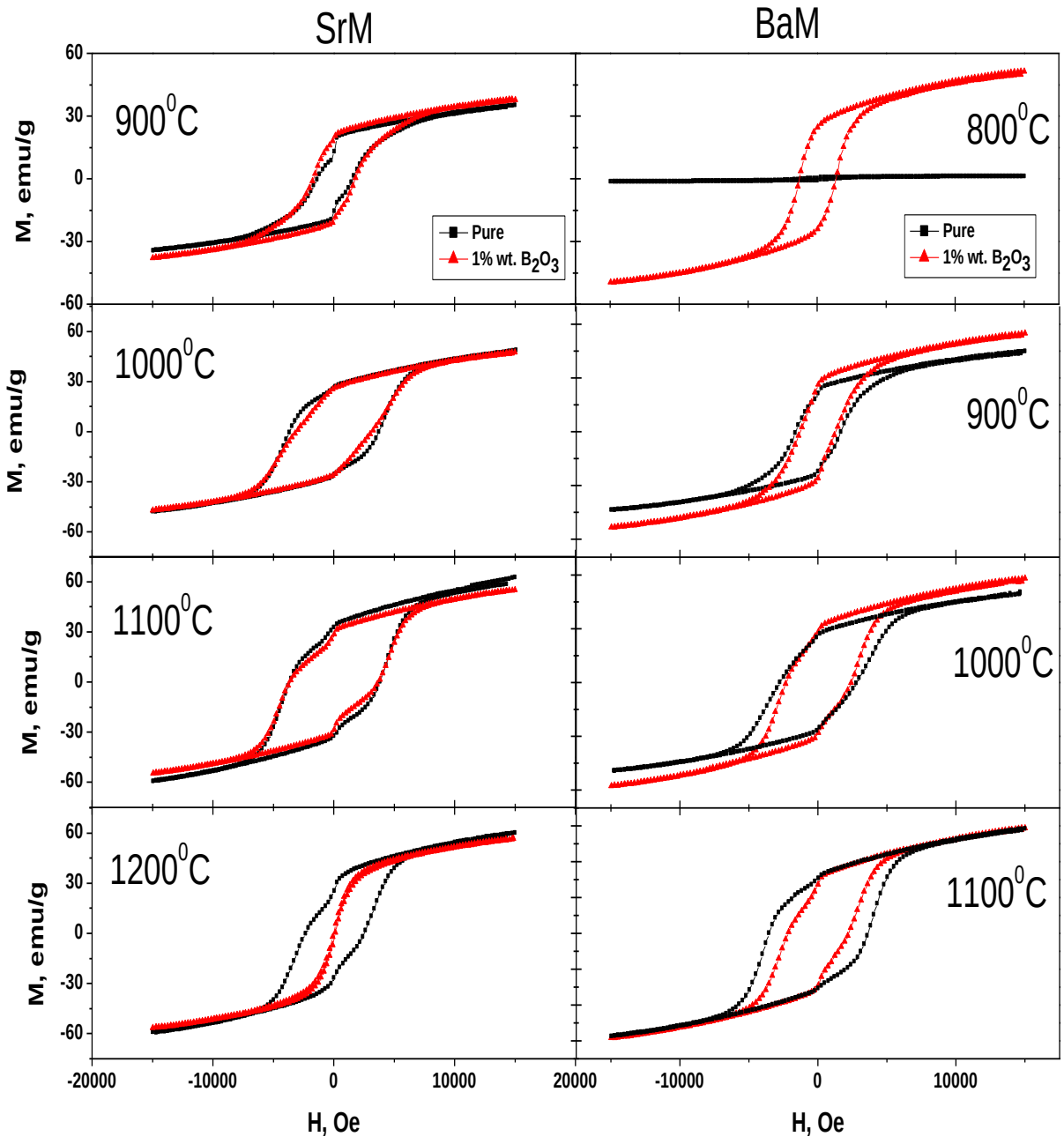

Figure 3.4 M-H curves of BaM and SrM samples.

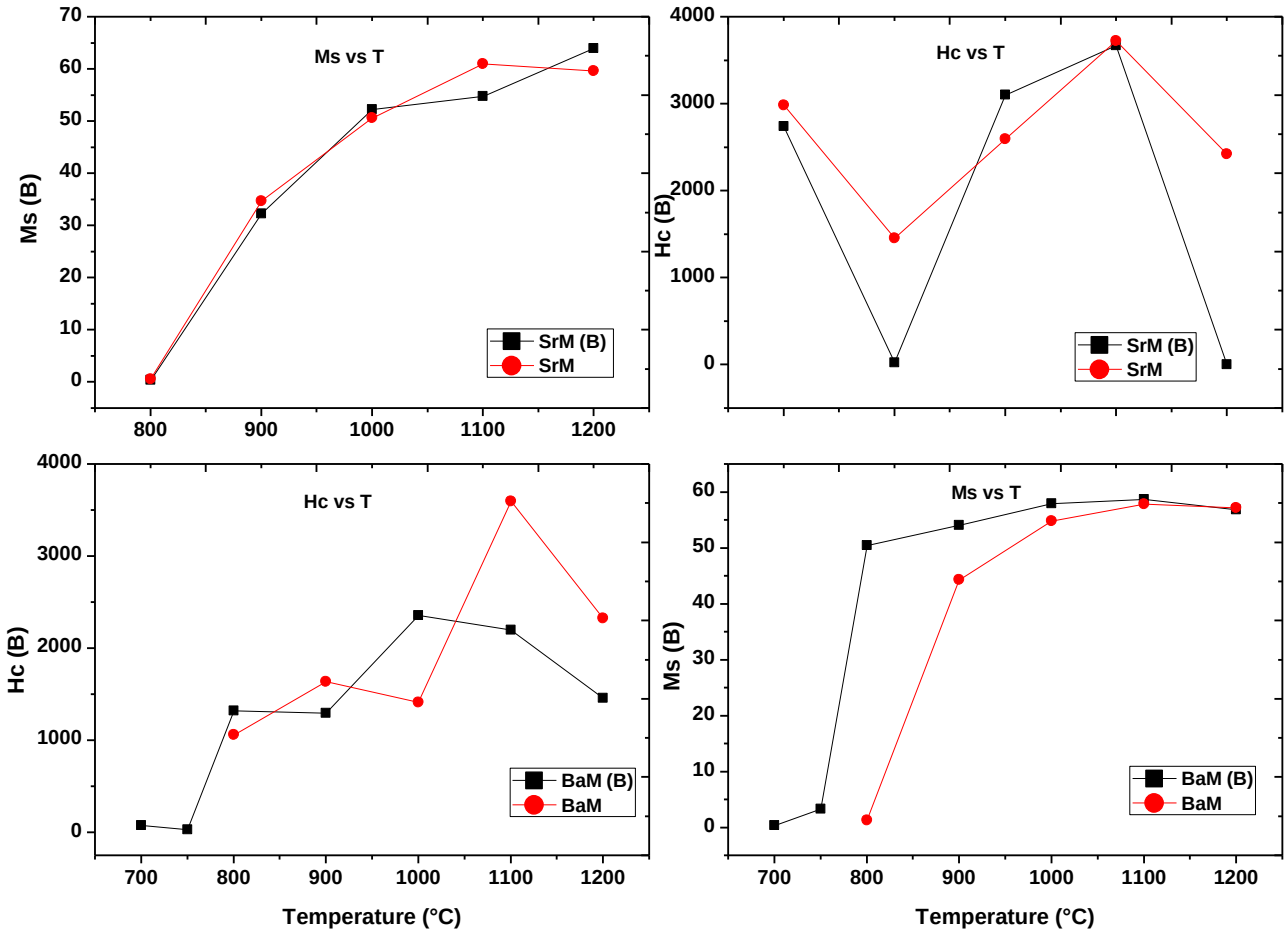

Figure 3.5 Variation of Ms and Hc with sintering temperature of BaM and SrM samples.

As a result, optimal Fe/Sr ratio appears to be 12 for SrM. In the case of BaM, coercivity first increases from 2.14 to 2.8 kOe as Fe/Ba ratio raises from 10 to 10.5 and then decreases continuously with increasing molar ratio up to 1.3 kOe at Fe/Ba = 12. Ms increases first sharply between molar ratios 10 and 10.5, then steadily up to 11.5 at which, it becomes maximum at 62 emu/g and decreases at 12. The optimal Fe/Ba ratio seems to be 10.5 for BaM. At this molar ratio, coercivity is maximum and Ms is very close to the maximum value.

The Stoner-Wohlfarth equation (Eqn.1) (Wohlfarth 1958) was used to understand type of magnetic interactions between domains at different sintering temperatures.

$$M_d(H)/M_r(\infty) = 1 - 2\,M_r(H)/M_r(\infty) + \delta M(H) \qquad (1)$$

where $\delta M(H)$ is the interaction term, M_d represents demagnetization remanence at external field H, $M_r(\infty)$ is the isothermal remanent magnetization term at saturation.

Table 3.3 Magnetic parameters of BaM and SrM samples synthesized with and without B_2O_3.

		Pure				With B_2O_3		
SrM	**T (ºC)**	**Ms (emu/g)**	**Mr (emu/g)**	**Hc (Oe)**		**Ms (emu/g)**	**Mr (emu/g)**	**Hc (Oe)**
	800	0,56	0,20	2985		0,44	0,11	2741
	900	34,72	14,37	1458		37,95	19,44	1743
	1000	50,68	25,78	2595		52,28	25,30	3105
	1100	60,99	32,49	3726		54,79	28,54	3671
	1200	59,64	25,94	2425		63,97	0,25	5
BaM	**800**	1,34	0,55	1064		50,49	24,40	1322
	900	44,29	21,67	1639		54,07	26,09	1297
	1000	49,9	23,44	2771		57,90	28,32	2360
	1100	57,90	30,69	3597		58,66	28,11	2201
	1200	57,17	27,64	2327		56,88	19,53	1461

The importance of δM(H) term is that, it is proportional to the fraction of the particles switched along or opposite to the field direction in a particular field, H. Positive (negative) values of δM(H) corresponds to the magnetizing-like (demagnetizing-like) interactions. For non-interacting systems δM(H) is a horizontal line passing through origin. As it is seen in Figure3.7, SrM samples sintered at 900°C, both pure and boron added, δM(H) is positive in a whole field range meaning that magnetic interactions are constructive that try to stabilize remanent magnetization state. As sintering temperature rises, destructive type interactions occur in pure SrM samples at fields higher than 5 kOe. Meanwhile, SrM samples prepared

with boron magnetic interactions are constructive in the whole range and at all temperatures. In addition to this, fraction of domains aligned in the field direction is higher in boron containing samples, except the one sintered at 900°C. There are both constructive and destructive type interactions for BaM samples, pure and boron added, at all temperatures. It can be stated that fraction of domains contributing destructively to remanent magnetization is lower in boron added samples. Besides, the optimal sintering temperature seems to be 1000°C for BaM at which, destructive interactions are minimum in both pure and boron added samples.

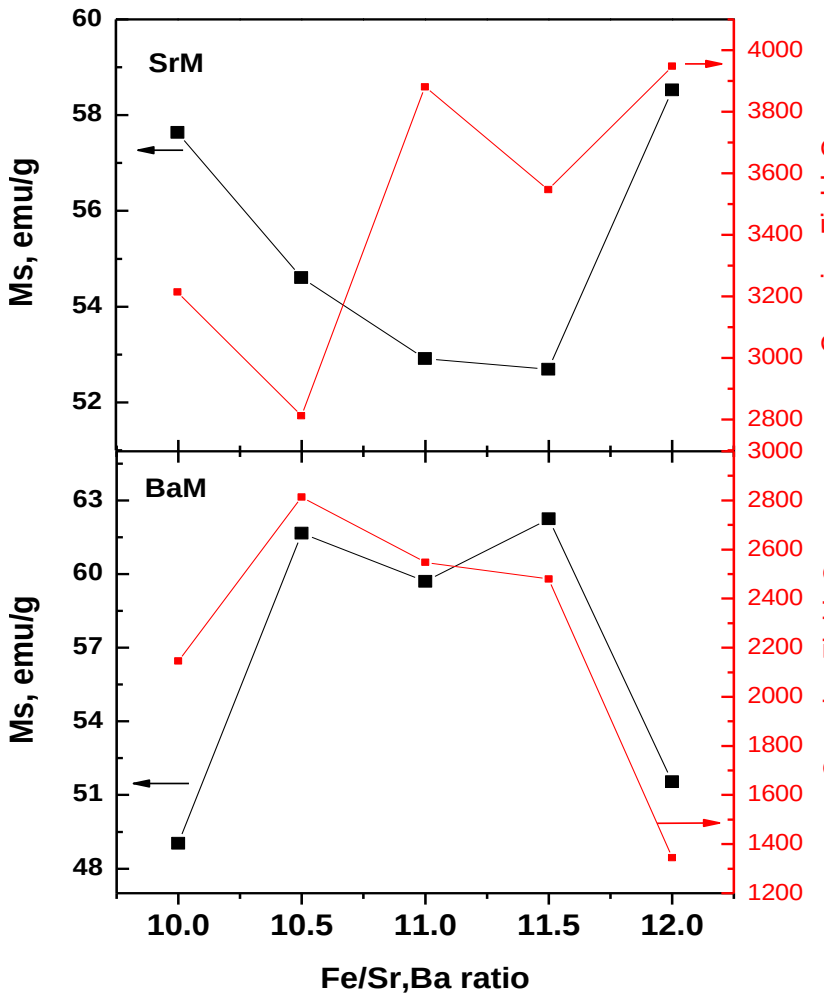

Figure 3.6 Variation of the magnetic parameters Ms and Hc of BaM and SrM samples with Fe/(Ba,Sr) ratio.

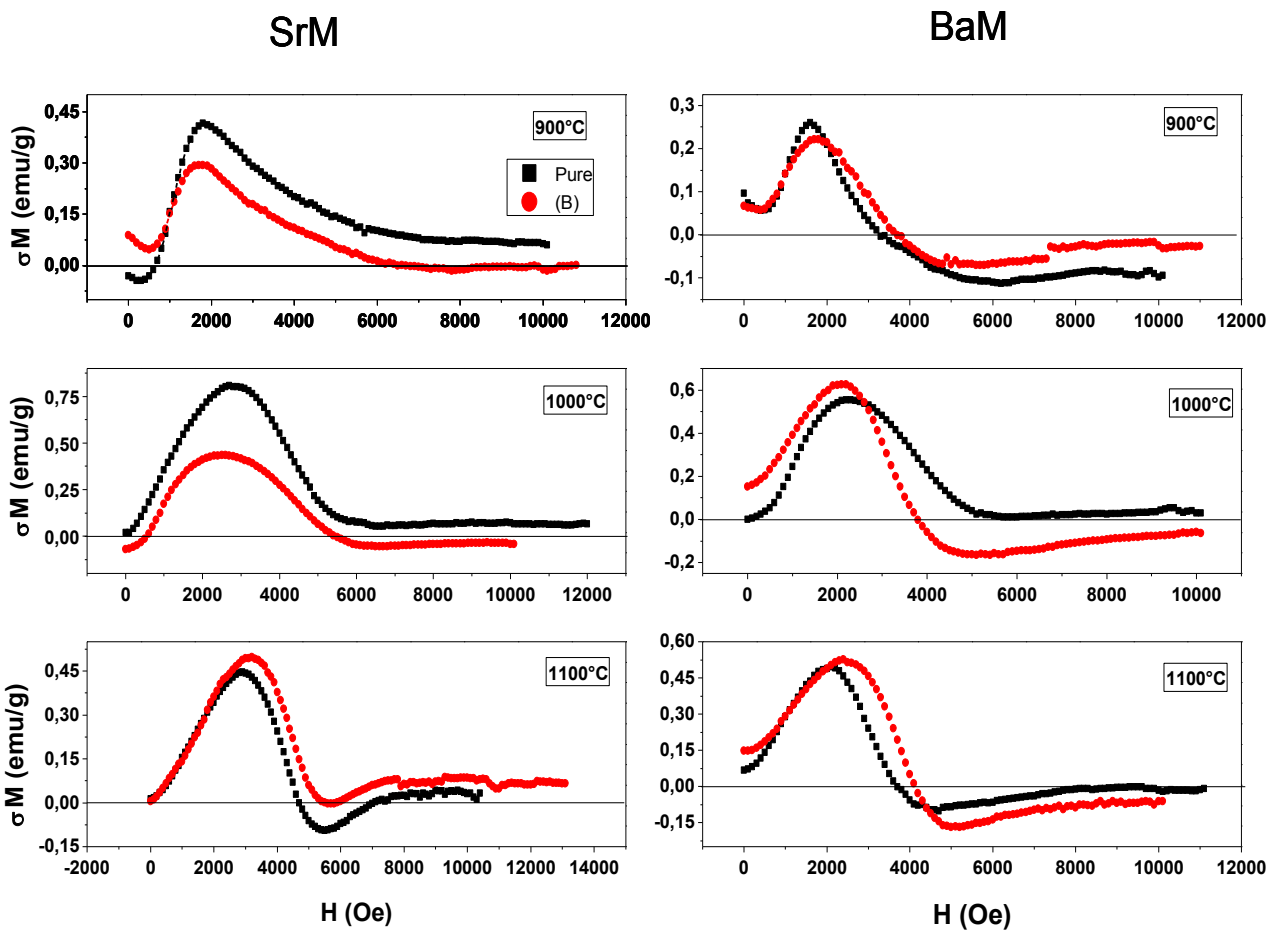

Figure 3.7 δM vs H. Magnetic interactions in BaM and SrM prepared with and without boron addition.

In conclusion, BaM and SrM samples were successfully synthesized with boron addition using solid state reaction method. The hard BaM phase was obtained in the boron added sample at 800C with quite good magnetic parameters. While boron free sample has negligible magnetization, which indicates that fraction of BaM phase is very low or not formed at all. The optimal Fe/Ba ratio was determined as 10.5 and 11.5 for boron added and pure samples, respectively. Single to multi domain transition occurred at 1000°C for boron included and 1100°C for pure samples. Above these threshold temperatures magnetization reversal occurs through domain wall motion. Magnetic parameters (both Ms and Hc) of pure and boron added SrM samples are close to each other at all temperatures, except 1200°C at which coercivity of boron added samples decreases very sharply. Sample

shows almost soft ferromagnetic type behavior due to the increasing domain size. Finally, determination of magnetic interactions revealed that boron addition reduces the strength of the destructive type interactions in both SrM and BaM. Thus, it helps to stabilize the remanent state of the samples at all sintering temperatures.

3.1.3 SEM Analysis

SEM images, shown in Figure 3.8, of both pure BaM and SrM shows the fact that temperature makes grains definite. Higher the temperature, more the significant and individual grains formed. At 800°C, it can be claimed that hexaferrite grains does not start to be formed. At 1000°C, hexagonal geometry starts to be appeared. At 1200°C, separated, individual, shaped grains are clearly seen.

For the samples which B_2O_3 added, very similar trend is observed. From 900°C, which the grains start to be formed, to 1100°C, where grains are well-shaped and individual; as temperature increases, grains become shaped and separated compare to other samples that anneals at lower temperatures.

Barium hexaferrite grains with B_2O_3 addition form the hexaferrite geometry more definite than strontium samples at lower temperatures.

For the strontium sample annealed at 1200°C, the unique forming facing us: all grains are merged to each other which make that sample soft magnetic material.

As an additional comparison for these samples, effect of B_2O_3 on formation of grains can be examined. The samples which annealed at 900°C, 1000°C and 1100°C shows definitely the B_2O_3 addition makes the grains to be shaped and discrete and individual.

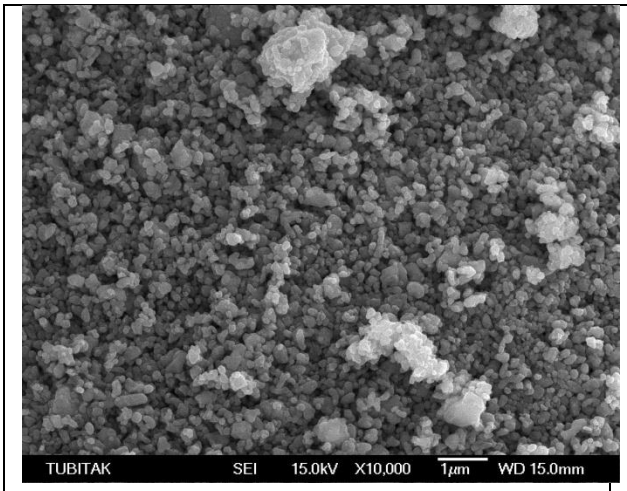

BaM-800

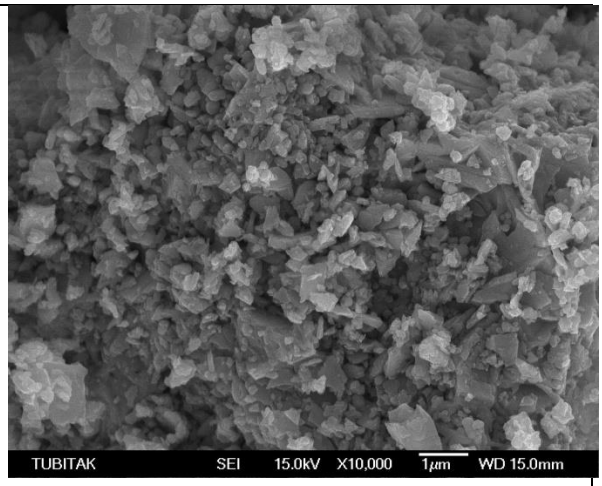

BaM-800B

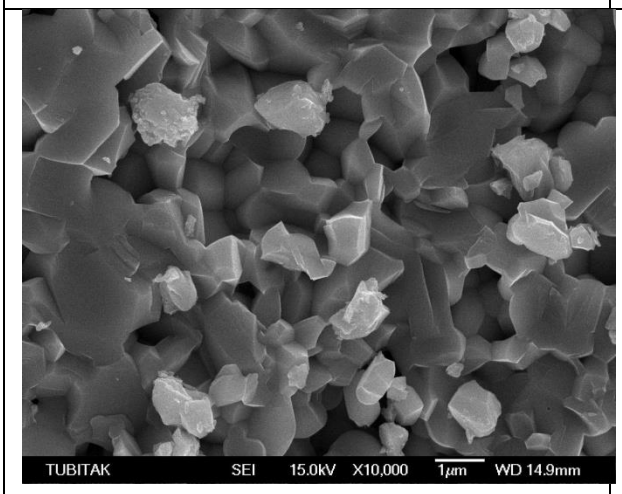

BaM-1200

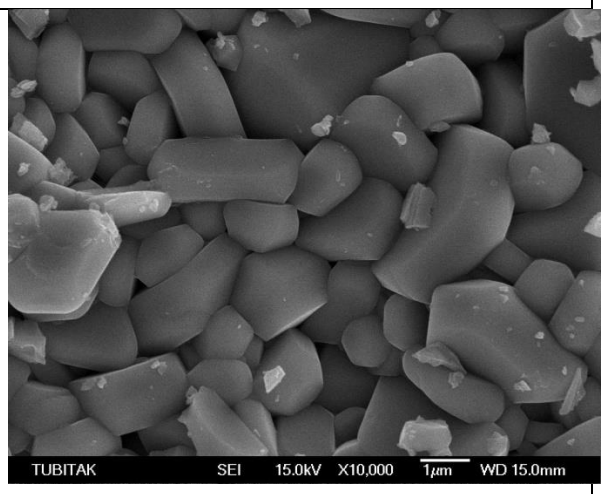

BaM-1200B

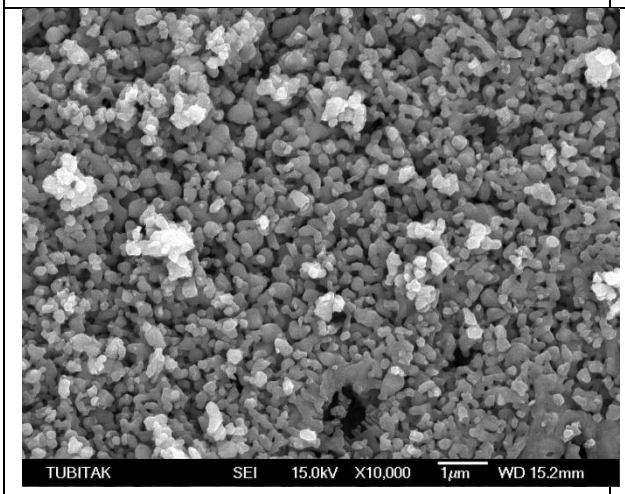

SrM 900

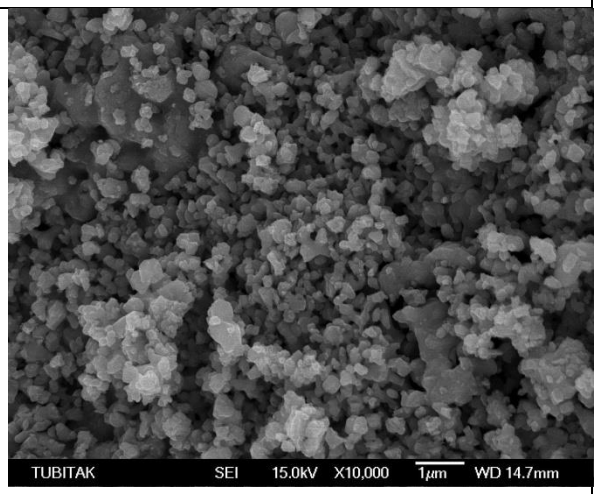

SrM 900B

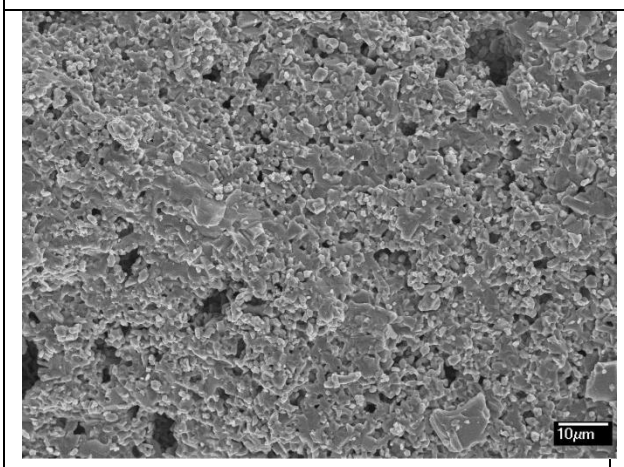

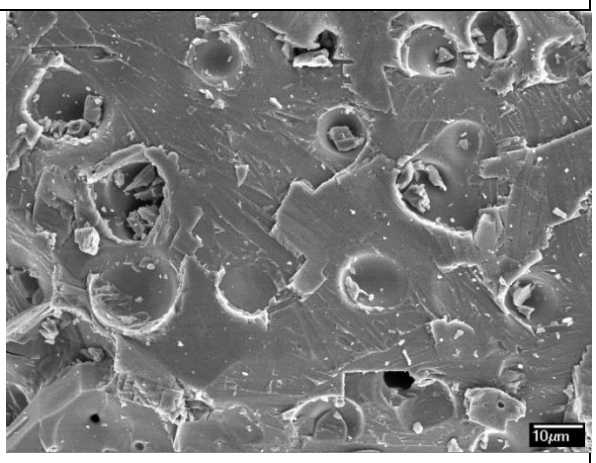

SrM 1200	**SrM 1200B**

Figure 3.8 SEM micrographs of BaM and SrM powders at different sintering temperatures.

In conclusion**,** barium and strontium hexaferrites were successfully synthesized with boron addition using solid state reaction method. The hard BaM phase was obtained in the boron added sample at 800C with quite good magnetic parameters. While boron free sample has negligible magnetization, which indicates that fraction of BaM phase is very low or not formed at all. The optimal Fe/Ba ratio was determined as 10,5 and 11,5 for boron added and pure samples, respectively. Single to multi domain transition occurred at 1000°C for boron included and 1100°C for pure samples. Above these threshold temperatures magnetization reversal occurs through domain wall motion. Magnetic parameters (both Ms and Hc) of pure and boron added SrM samples are close to each other at all temperatures, except 1200°C at which coercivity of boron added samples decreases very sharply. Sample shows almost soft ferromagnetic type behavior due to the increasing domain size. Finally, determination of magnetic interactions revealed that boron addition reduces the strength of the destructive type interactions in both SrM and BaM. Thus, it helps to stabilize the remanent state of the samples at all sintering temperatures.

3.2 SYNTHESIS of CATION / X (X=Co, Cu, Ni, Zn, Mn), MAGNESIUM and Ti DOPED BaM HEXAFERRITE with BORON ADDITION.

3.2.1 XRD Analysis

Crystal characterization of boron added $BaMg_{0.25}X_{0.25}Ti_{0.5}Fe_{11}O_{19}$ (X=Co, Cu, Ni, Zn, Mn) hexaferrites are done by means of XRD powder pattern. Sharp, intense and characteristic peaks are easily observed in Figure 3.9 graphs. There are six peaks hexaferrite crystal structure have, two theta values of these peaks are as follows, 30.4, 32.28, 34.2, 37.2, 40.42 and 42.5°. All calculations and comments are done by means of JCPDS file (27-1029). In Figure 3.9, all five hexaferrites correspond to these peaks and reflection sites. Although two theta values are matched with BaM original pattern, here are some differences are observed the samples got in intensity values and full width at half maximum (FWHM) which can be referred to doping to that of pure BaM structure with the help of original BaM XRD powder pattern, it can be said that samples do not have any phase as an extra. In Table 3.4, lattice parameters of the samples are shown. Original BaM's "a" and "c" value is taken as 5,89Å and 23,19Å respectively for lattice parameters and miller indices calculations. Other than $BaMg_{0.25}Cu_{0.25}Ti_{0.5}Fe_{11}O_{19}$ sample, all other samples' values are very same as original BaM hexaferrite crystal; on the other hand, "c" parameter value is not as same as the original BaM hexaferrite one, but 22.94Å value insists among them. According to Li et al. (Li, Chen et al. 2002), same lattice number of host material and guest one means that doped elements are placed exactly the same position that host crystal's ions occupied. In this case, Mn, Co, Ni and Zn ions replace with similar orientation with Fe ions in hexaferrite structure placed; however, Cu doped sample has larger "c" value, i.e. Cu ion does not place as same as Fe ion places.

By fitted nine peaks of XRD data and Eq. (3.1) (Wejrzanowski, Pielaszek et al. 2006) average crystallite size, D_{XRD}, and standard deviations σ are calculated (Figure 3.10 and Table 3.5). Line profile was fitted through nine peaks, miller indices are indicated in Figure 3.9. All data has same value of standard deviation σ, which is (±) 1nm. Both fitted and experimental profiles of XRD data are shown in Figure 3.10.

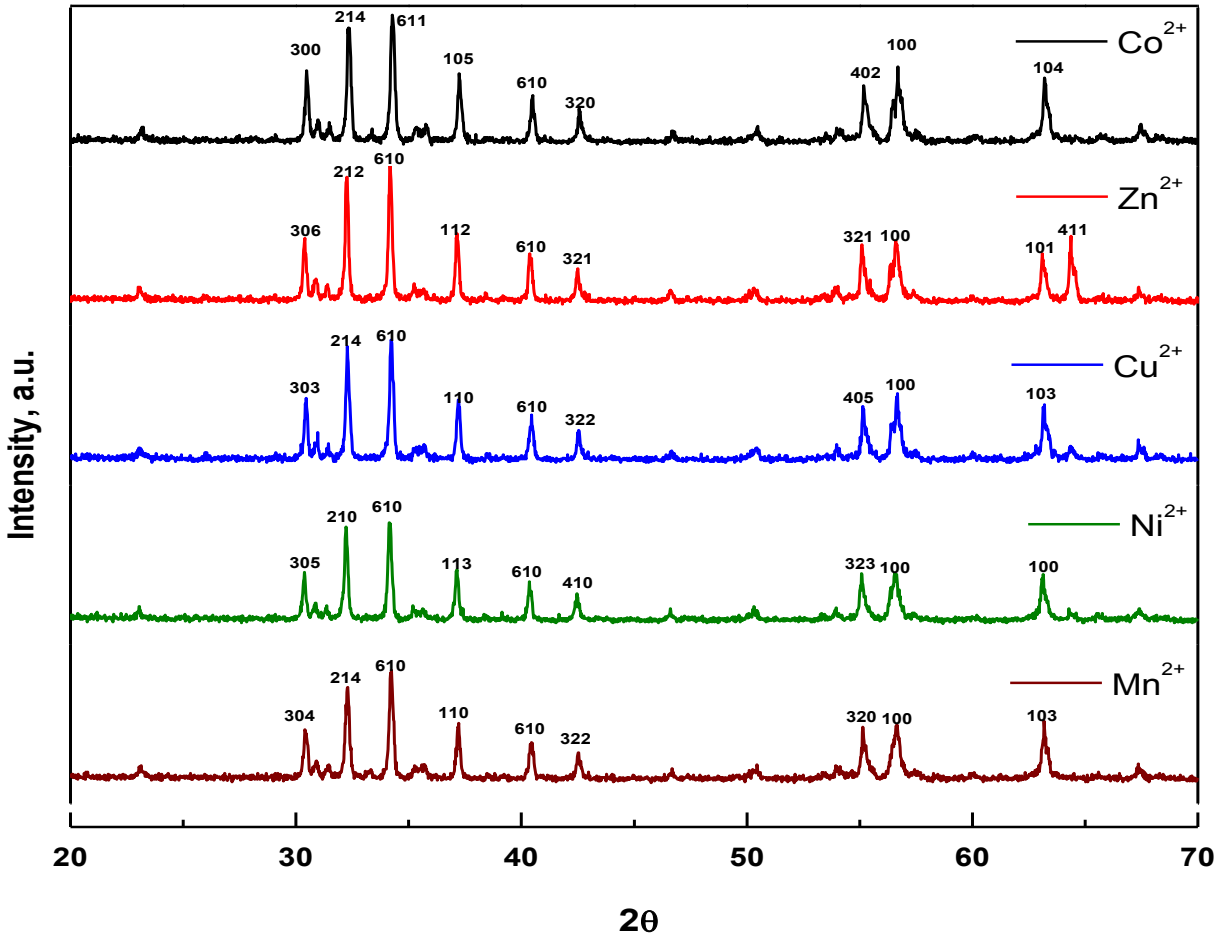

Figure 3.9 XRD powder patterns of $BaMg_{0.25}X_{0.25}Ti_{0.5}Fe_{11}O_{19}$ (B) (X=Co, Cu, Ni, Zn, Mn).

Table 3.4 Lattice constants of original BaM and $BaMg_{0.25}X_{0.25}Ti_{0.5}Fe_{11}O_{19}$(B) (X=Co, Cu, Ni, Zn, Mn).

$BaMg_{0.25}X_{0.25}Ti_{0.5}Fe_{11}O_{19}$(B)	a (Å)	c(Å)
Original BaM Hexaferrite	5.89	23.19
Mn^{+2}	5.89	22.94
Co^{+2}	5.89	22.94
Ni^{+2}	5.89	22.94
Cu^{+2}	5.89	24.25
Zn^{+2}	5.89	22.94

Table 3.5 Average crystallite sizes and standard deviations of $BaMg_{0.25}X_{0.25}Ti_{0.5}Fe_{11}O_{19}$ (B) samples.

$BaMg_{0.25}X_{0.25}Ti_{0.5}Fe_{11}O_{19}$ (B)	D_{XRD} (nm) (±) 1nm
X = Mn	44
X = Ni	50
X = Cu	50
X = Zn	55
X = Co	40

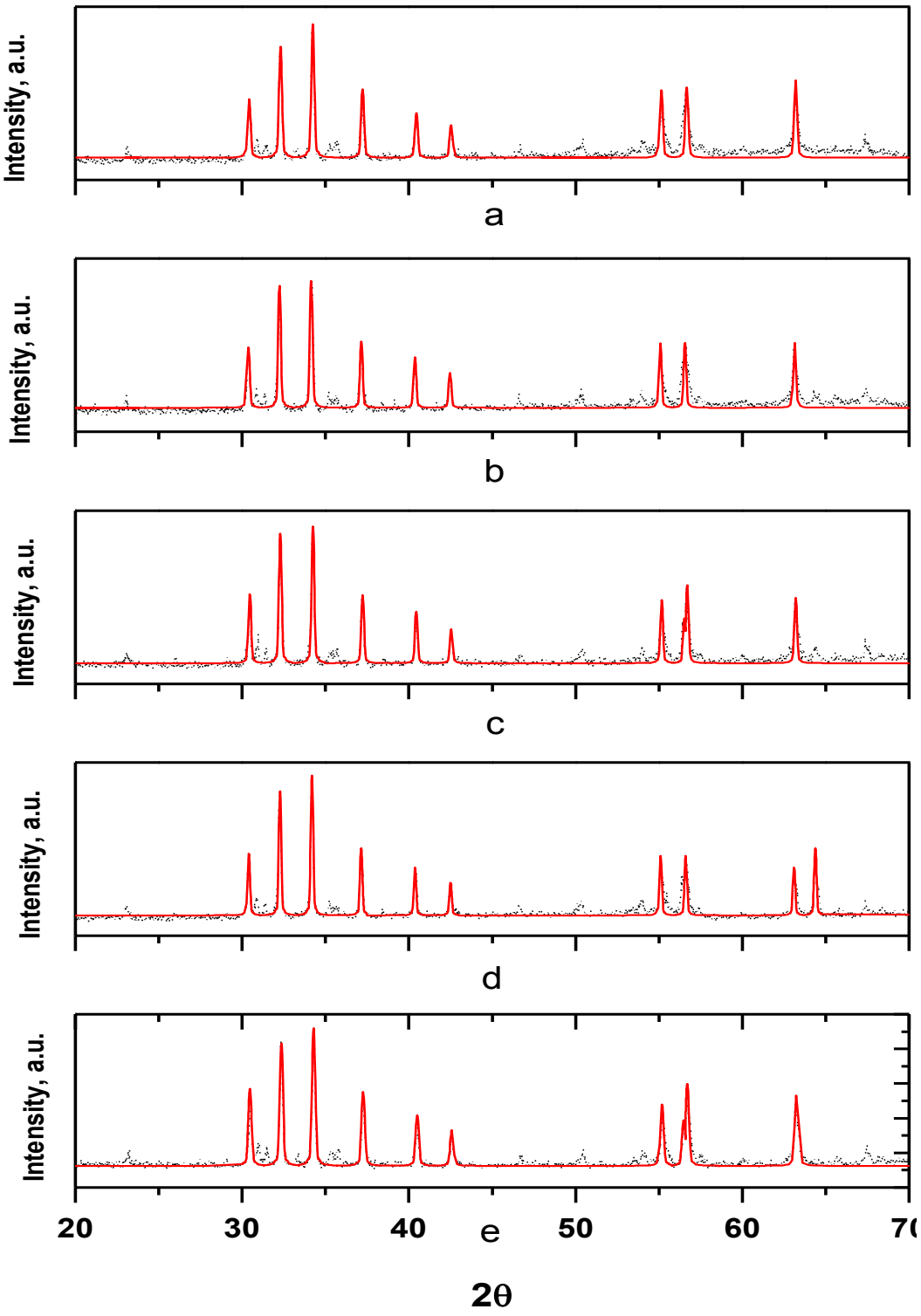

Figure3.10 Experimentally measured and theoretically line profile fitted XRD patterns of $BaMg_{0.25}X_{0.25}Ti_{0.5}Fe_{11}O_{19}$ (B) (a) X= Mn, (b) X= Ni, (c) X= Cu, (d) X= Zn, (e) X= Co.

3.2.2 VSM Analysis

Figure 3.11 shows the hysteresis curves of pure, doped and boron added BaM hexaferrite powders. Magnetic behaviors of serie members are very similar to each other. In Table 3.6 magnetic parameters can be observed by numerical values. All samples have coercivity (H_c) value at about range of 1000 – 1500 (Oe) that is hard magnet characterization. Resultant change in Ms values can be attributed to have different locations in crystal structure of BaM template. Smooth hysteresis loops are indicating the fact that there is only one dominated phase, due to resemblance of BaM hexaferrite hysteresis pattern and with contribution of other characterization results, one can say that dominated phase in these powders are hexaferrite phase; i.e. desired hexaferrite phase is successfully be synthesized.

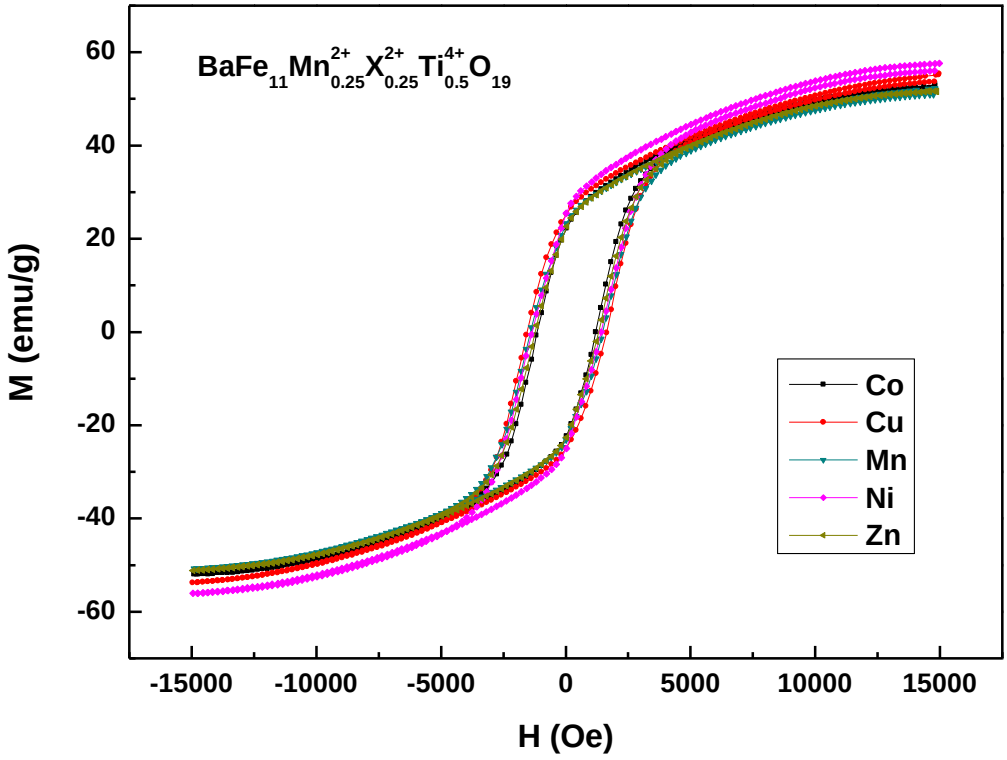

Figure 3.11 Hysteresis loops of $BaMg_{0.25}X_{0.25}Ti_{0.5}Fe_{11}O_{19}$ (B) (X=Co, Cu, Ni, Zn, Mn).

Table 3.6 Magnetic parameters of $BaMg_{0.25}X_{0.25}Ti_{0.5}Fe_{11}O_{19}$ (B) (X=Co, Cu, Ni, Zn, Mn).

$BaMg_{0.25}X_{0.25}Ti_{0.5}Fe_{11}O_{19}$(B)	H_c(Oe)	M_r(emu/g)	M_s(emu/g)
$BaMg_{0.25}Co_{0.25}Ti_{0.5}Fe_{11}O_{19}$(B)	1193	22	52
$BaMg_{0.25}Zn_{0.25}Ti_{0.5}Fe_{11}O_{19}$(B)	1306	22	51
$BaMg_{0.25}Ni_{0.25}Ti_{0.5}Fe_{11}O_{19}$(B)	1416	25	56
$BaMg_{0.25}Mn_{0.25}Ti_{0.5}Fe_{11}O_{19}$(B)	1476	23	51
$BaMg_{0.25}Cu_{0.25}Ti_{0.5}Fe_{11}O_{19}$(B)	1632	25	54

3.2.3 SEM Analysis

SEM images of BaM samples are shown in Figure 3.12. In hexaferrites, single domain limit is 1μm (Sözeri et al. 2015). BaM which is investigated in this study is in the range of that limit. Domain discreteness, shape and size directly affect magnetic anisotropy, directly the magnetic properties of the samples. As it is mentioned in the VSM analysis part, all serie member samples have very close magnetic properties. Therefore, very similar morphology observation in SEM analysis is not an unexpected result. Although all the samples have hexagonal shaped-domains, in some part of the sample, domain walls are not segregated well. In addition, agglomeration is incontrovertible fact that should be indicated for these samples.

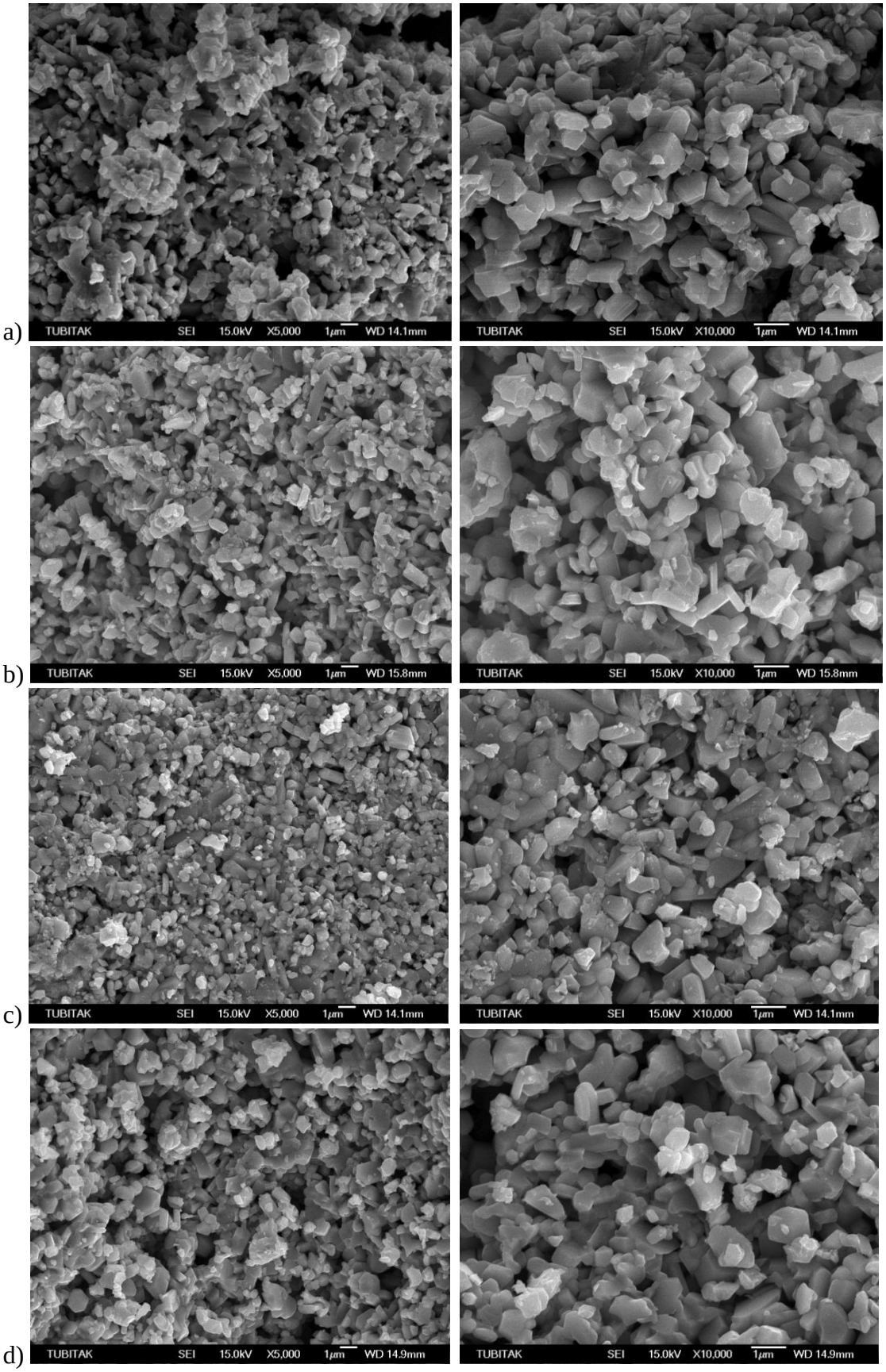
a)
TUBITAK SEI 15.0kV X5,000 1μm WD 14.1mm
TUBITAK SEI 15.0kV X10,000 1μm WD 14.1mm
b)
TUBITAK SEI 15.0kV X5,000 1μm WD 15.8mm
TUBITAK SEI 15.0kV X10,000 1μm WD 15.8mm
c)
TUBITAK SEI 15.0kV X5,000 1μm WD 14.1mm
TUBITAK SEI 15.0kV X10,000 1μm WD 14.1mm
d)
TUBITAK SEI 15.0kV X5,000 1μm WD 14.9mm
TUBITAK SEI 15.0kV X10,000 1μm WD 14.9mm

e) 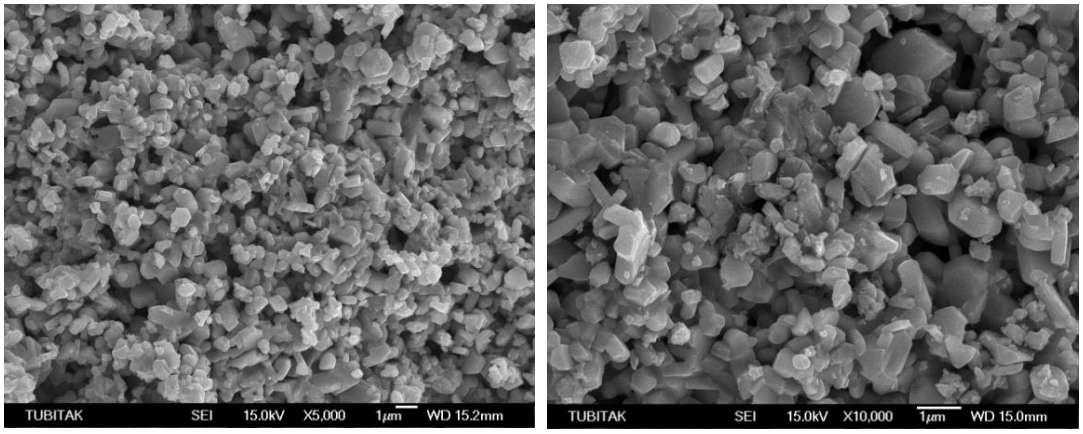

Figure 3.12 SEM micrographs of $BaMg_{0.25}X_{0.25}Ti_{0.5}Fe_{11}O_{19}$ (B) (a) X= Mn, (b) X= Co, (c) X= Ni, (d) X= Cu, (e) X= Zn.

3.2.4 MW Analysis

Reflection loss (RL) values for the samples were calculated using complex permittivity and permeability values using the equation below

$$RL(dB) = -20log|(Z - Z_0)(Z + Z_0)| \quad (3.3)$$

where $Z = Z_0\sqrt{\mu_r/\varepsilon_r} * \tan h * \left[\left(-j\frac{2\pi f d}{c}\right) * \sqrt{\mu_r/\varepsilon_r}\right]$, $\mu_r = \mu' - j\mu''$ and $\varepsilon_r = \varepsilon' - j\varepsilon''$. Z_0 is the impedance of free space which is 377 Ω, f is the frequency and d is the thickness of the absorber.

The absorption spectra of the samples between 2 and 18 GHz are shown in Figure 3.15. Mg-Mn-Ti substituted BaM sample having a thickness of 3 mm has two RL peak value of — 30 dB at 10 GHz and of — 29 dB at 19 GHz with 1.5 GHz and 2 GHz bandwidth at — 20 dB respectively. The minimum RL values of other samples vary between — 21 and — 34 dB with very close resonance frequencies. It appeared that impedance matching occurs at around 10 GHz for all samples with 3 mm thicknesses. It was succeeded to get quite high RL values at 10 GHz, which coincides with the working frequency of some military radars used for airborne and shipborne surveillance and navigation (Sözeri et al. 2015). For both peaks at about 10 GHz and at k-band region tan

loss contributes to reflection losses. As seen in Figure 3.13, larger the tan loss value, lower the reflection loss trend is followed by the samples. In addition, for Zn, Ni and Cu doped samples; there are two absorption peaks that second peaks are due only to tan losses. RL peaks can be commented through cations' occupying orientation in crystalline structure. Moreover, Figure 3.14 shows the fact that all samples have full penetration at the X band frequencies which MW absorption occurs.

In conclusion, $BaMg_{0.25}X_{0.25}Ti_{0.5}Fe_{11}O_{19}$ (B) samples are synthesized by solid state method with 1% boron addition. Nonmagnetic (Mg), dielectric (Ti) and varying magnetic valued cations (X=Mn, Co, Ni, Cu, Zn) are doped. According to VSM analyses, difference were observed in magnetic behavior between samples due to orientations of doped cations in hexaferrite crystal structure. All samples were classified as hard ferromagnet. Hexaferrite crystal formation is seen in SEM micrographs. RL values of samples vary between -21 dB (3.16% reflection in volt) and -34dB (2 % reflection in volt). Mn doped sample has two absorption peaks that 3.22% in volt (-30dB RL) and 3.57% in volt (-29dB RL) reflection the sample has at X band and k band respectively. All samples have full penetration at absorption frequencies at X band.

The RL spectra of Mg-Mn–Ti substituted barium hexaferrite for different thicknesses are shown in Figure 3.16 By means of 3mm thick sample's experimental RL result, other thickness RL graphs are calculated. 2 mm thick sample has a RL value of — 45 dB at 14 GHz with the resonance bandwidth of 3 GHz at — 20 dB. As the thickness of the sample increases, the resonance peak shifts to lower frequencies. For which 6 mm thick sample, there are two MW absorption peaks. Lower frequency absorption peak occurs due to matching thickness, second peak of that sample which is around 11 GHz is due to tan loss, dielectric tan loss is dominated.

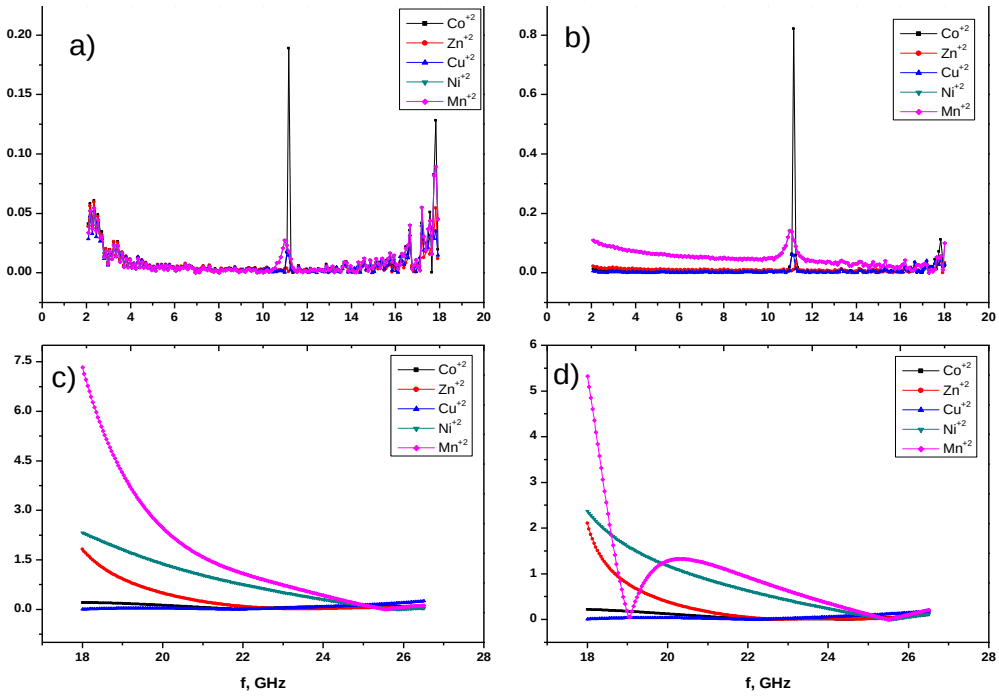

Figure 3.13 Tangent loss (μ''/μ' for dielectric tan loss, ε''/ε' for dielectric tan loss) graphs of $BaMg_{0.25}X_{0.25}Ti_{0.5}Fe_{11}O_{19}$ (B) (a,d) dielectric tan loss graphs (b,c) magnetic tan loss graphs.

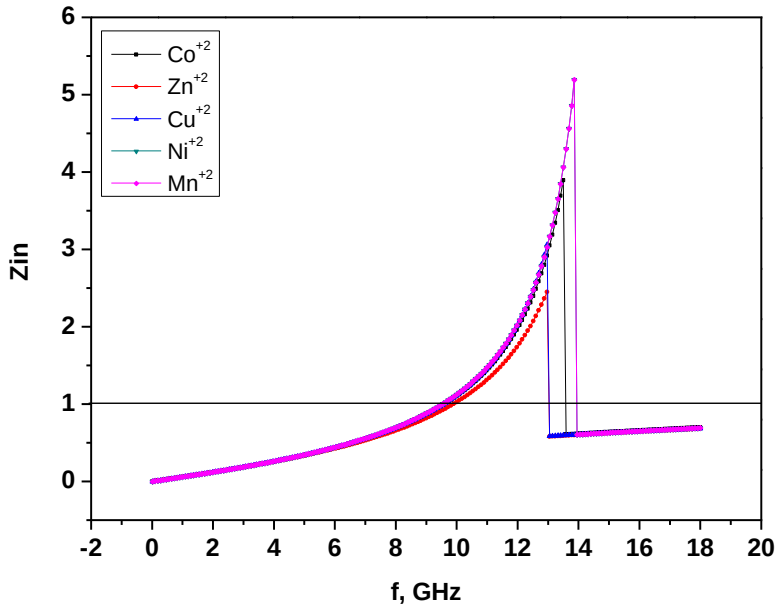

Figure 3.14 Zin graphs of $BaMg_{0.25}X_{0.25}Ti_{0.5}Fe_{11}O_{19}$ (B)

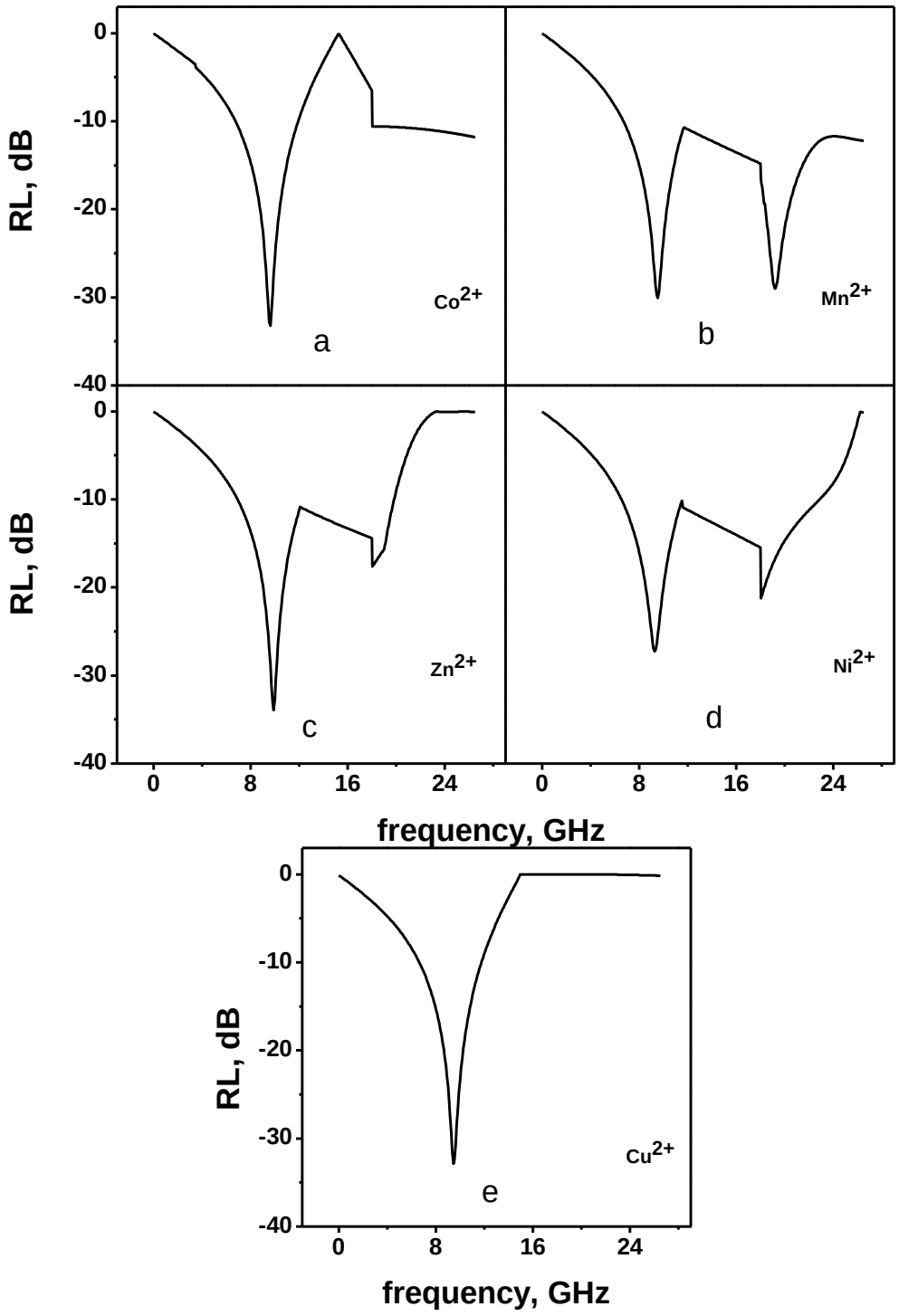

Figure 3.15 MW analysis of $BaMg_{0.25}X_{0.25}Ti_{0.5}Fe_{11}O_{19}$ (B) (a) X= Co (b) X= Mn, (c) X= Zn, (d) X= Ni, (e) X= Cu.

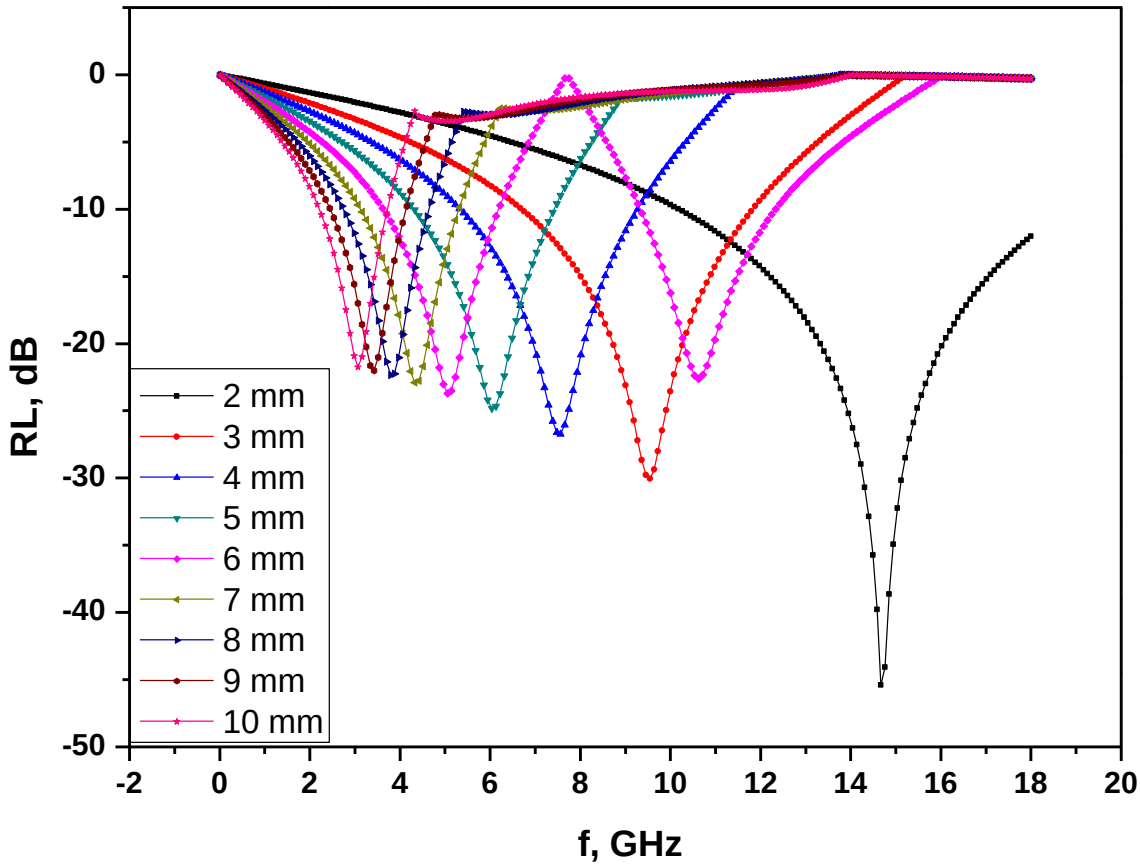

Figure 3.16 RL values of Mg-Mn-Ti substituted samples having various thicknesses between 2 and 10 mm.

3.3 SYNTHESIS of BORON ADDED CATION / X (X=Co, Cu, Ni, Zn, Mn) and Ti DOPED BaM HEXAFERRITE

3.3.1 XRD Analysis

The XRD powder patterns of all samples are presented in Figure 3.17, which shows sharp, high intensity peaks and matches well with the standard data obtained from M-type of $BaFe_{12}O_{19}$ (JCPDS Patterns no. 84-0757). All the reflections could be indexed well with the crystal cell of hexagonal ferrite. In the Co–Ti, Ni–Ti and Zn–Ti substituted sample, there is a very low intensity peak corresponding to α-Fe_2O_3 (JCPDS Patterns no. 86-0550). The peaks of the host material as well as the substituted hexaferrites appear at the same positions but with different Full Width at Half Maximum (FWHM) in this study. As it was mentioned by Soman et al. (Soman, Nanoti et al. 2013), this observation could be attributed to the occupation of crystallographic sites of Fe^{+3} ions by the substituted ions. The reflections were indexed as shown in Figure 3.17. The average crystallite sizes (*t)* were calculated from the diffraction line-width of XRD pattern, based on Scherrer's relation:

$$t = 0.9 / \cos(2)\lambda\beta\theta \qquad (3.3)$$

where, β is the full width at half maximum (FWHM).

The changes in the lattice parameters can be attributed to different ionic radii of substituted ions Zn^{2+} (0.74 Å), Ti^{4+} (0.61 Å), Co^{2+} (0.72 Å), Mn^{2+} (0.67 Å), Ni^{2+} (0.69 Å) and Cu^{2+} (0.85 Å) as compared to that of Fe^{3+} (0.67 Å). Unlike the lattice parameter "c", "a" remains almost constant (Sözeri, Deligöz et al. 2014). As it was indicated by Li et al. (Li, Chen et al. 2002), this may imply that substituted ions may preferentially occupy some sites in the five different crystallographic sites of M-type ferrite. Lattice parameters and crystallite sizes of all samples are shown in Table 3.7.

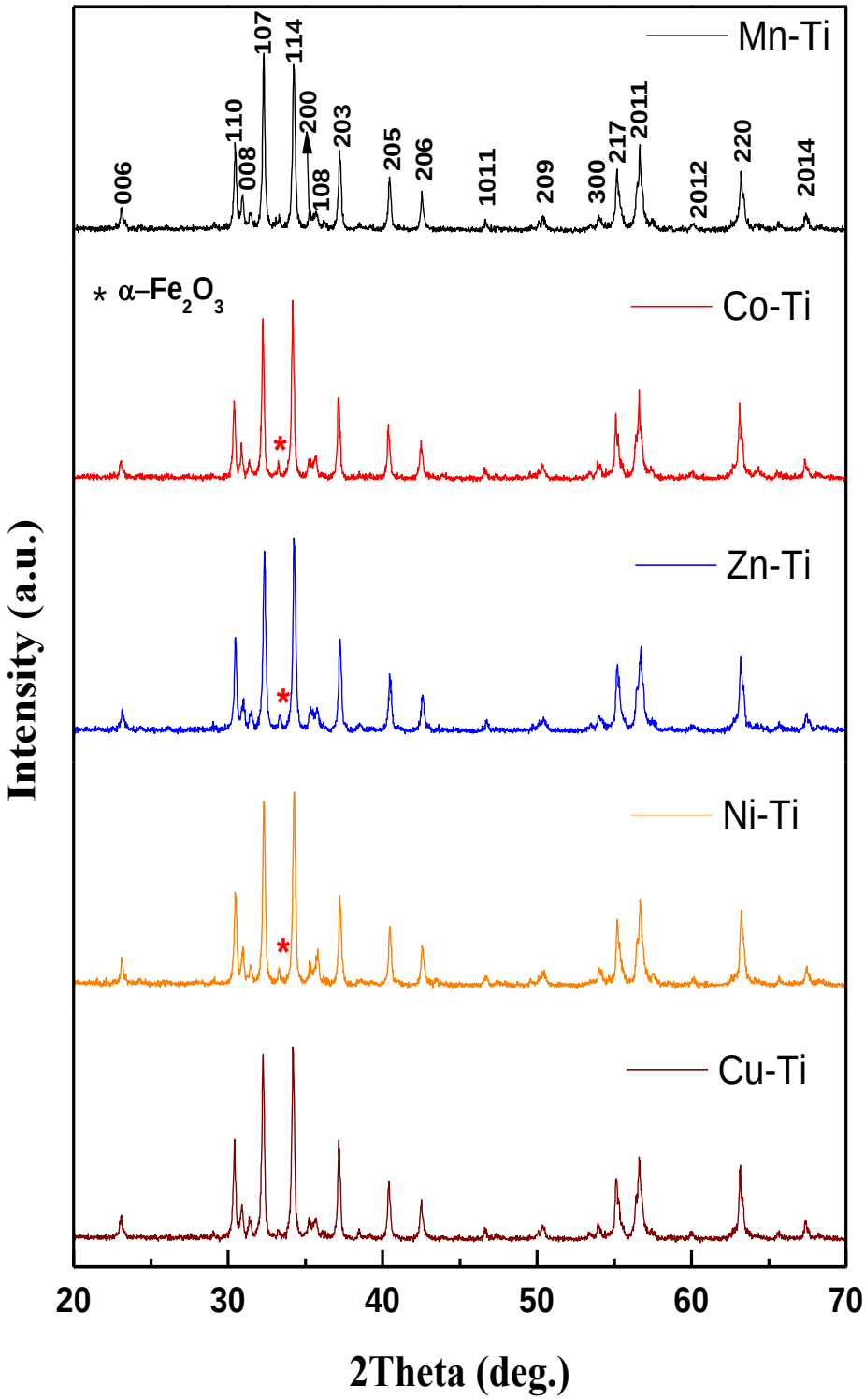

Figure 3.17 XRD spectra with Rietveld analysis patterns of Mn- Ti, Zn- Ti, Co- Ti, Cu- Ti and Ni- Ti substituted barium hexaferrites.

Table 3.7 Lattice constant of samples. Crystallite sizes of samples calculated using Scherrer's formula from (114) peak.

Sample	$a = b$ (Å)	c (Å)	D (nm)
$BaFe_{11}Ni_{0.5}Ti_{0.5}O_{19}$	5.890	23.203	77.161
$BaFe_{11}Zn_{0.5}Ti_{0.5}O_{19}$	5.901	23.204	77.410
$BaFe_{11}Co_{0.5}Ti_{0.5}O_{19}$	5.890	23.208	77.512
$BaFe_{11}Mn_{0.5}Ti_{0.5}O_{19}$	5.890	23.209	77.281
$BaFe_{11}Cu_{0.5}Ti_{0.5}O_{19}$	5.890	23.205	77.332

3.3.2 VSM Analysis

Magnetic properties of the composites have been determined by measuring M–H hysteresis curves at room temperature as shown in Figure 3.18. ın addition, magnetic parameters are listed in Table 3.8. Despite the substitution of non-magnetic ions, sample including Zn–Ti ions has high saturation magnetization (Ms) of 63.2 emu/g. This could be related to the site preferences of Zn^{2+} and Ti^{4+} ions among the five different Fe-sublattices: 12k, 4f2, 2a, 4f1 and 2b. Replacement of Zn^{2+} ions with anti- ferromagnetically ordered Fe^{3+} ions at 4f1 and 4f2 sites increases the net magnetic moment of barium hexaferrite (Yang, Wang et al. 2002; González-Angeles, Mendoza-Suarez et al. 2005). On the other hand, when Mn^{2+} ions were substituted together with Ti^{4+} ions (i.e., Mn–Ti substitution), saturation magnetization of the sample decreases to 56.7 emu/g. This is due to the occupation of Ti^{4+} ions at ferromagnetically ordered octahedral sites (Sözeri et al. 2015). As a result, net magnetization of the composite decreases. For instance, when Co^{2+} –Ti^{4+} ions were substituted, saturation magnetization of the sample decreased. It was reported that Co^{2+} –Ti^{4+} ions prefer to substitute Fe^{3+} ions at 4f2 and 2a sites, when small amounts are substituted (i.e., x= 0.0–0.2). If large amounts of Co–Ti ions are used, these ions prefer

to stay at ferromagnetically ordered 12k, 2a and 2b sites (Belous, V'Yunov et al. 2006; Tsutaoka and Koga 2013). Hence, replacement of Co^{2+} ions having magnetic moment of 3 m_B and non-magnetic Ti ions with Fe^{3+} ions at high spin states (i.e., 12k,2a and 2b sites) with magnetic moment of 5 m_B results in a decrease in magnetization of the sample. In addition to site preferences of substituted ions, the reason for the decrease in the magnetization of Mn–Ti and Co–Ti substituted samples can also be due to decrease in the superexchange interaction between Fe^{3+} and Fe^{2+} ions.

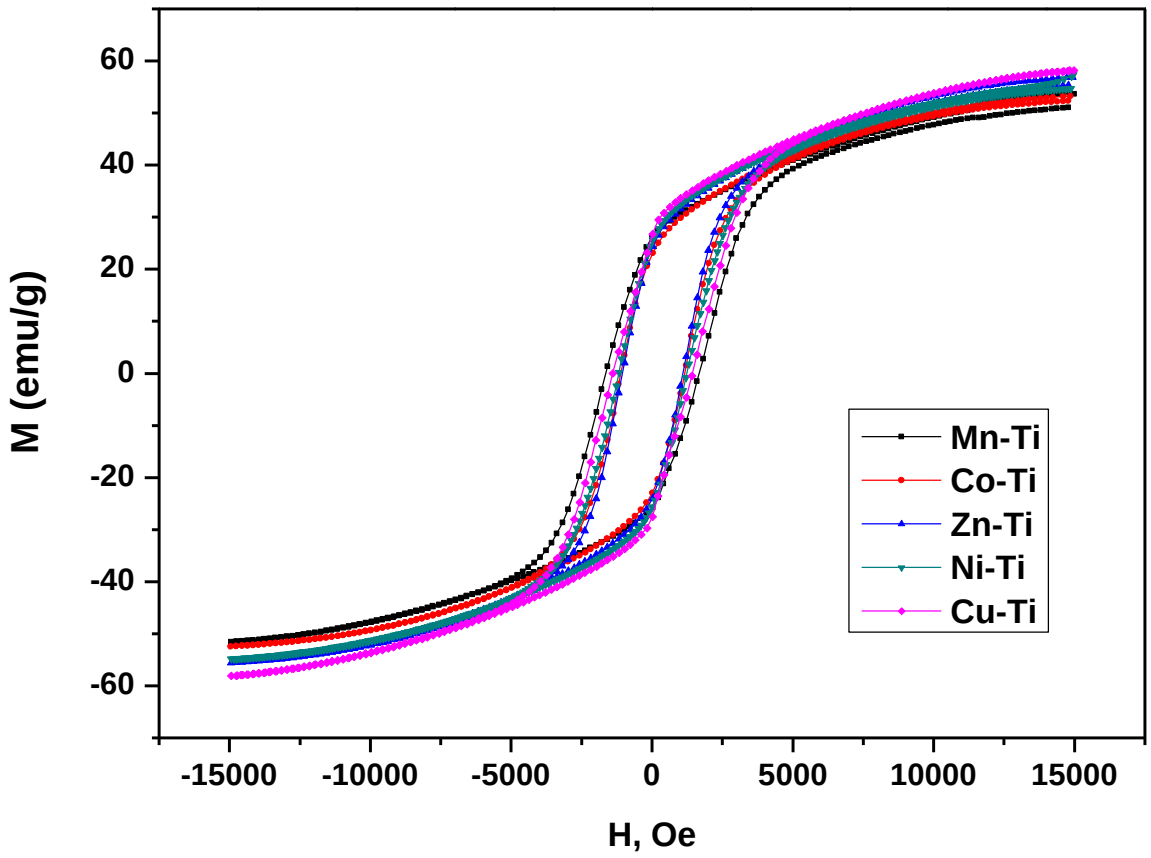

Figure 3.18 M-H hysteresis curves of Mn- Ti, Zn- Ti, Co- Ti, Cu- Ti and Ni- Ti substituted barium hexaferrites.

Cu^{2+} ions with magnetic moment of 1 m_B replace Fe^{3+} ions in octahedral sites at 12k↑, 4f2↓ and 2a↑ (Hemeda and Hemeda 2008). A slight decrease in magnetization can be expected since the number of Fe^{3+} ions in high spin states is more than that in low spin

states. On the other hand, the radius of Cu^{2+} ions is 0.73 Å, that is larger than that of Fe^{3+} (0.63 Å) ions, substitution of which increases the length of the c-axis. Thus, negative contribution of low spin states at 4f1 and 4f2 decreases. As a result, one may see no considerable change in magnetization as observed in Figure 3.18 Finally, Ni^{2+} ions having magnetic moment of 2 m_B replace Fe^{3+} ions at 4f2↓ site for small (~ 0.1 mol%) and 12k↑ site for larger amounts (Yang, Wang et al. 2002; Kanagesan, Jesurani et al. 2012). Therefore, it may be expected a decrease in magnetization not only due to the weakening of magnetization at 12k↑ site, but also due to the poor exchange interactions. Thus, magnetization of Ni–Ti substituted sample decreases to 57.5 emu/g. All magnetic parameters of the samples are shown in Table 3.8.

Table 3.8 Magnetic parameters of Mn- Ti, Zn- Ti, Co- Ti, Cu- Ti and Ni- Ti substituted samples.

$BaFe_{11}X_{0.5}Ti_{0.5}O_{19}$	M_s (emu/g)	M_r (emu/g)	H_c (Oe)
$BaFe_{11}Cu_{0.5}Ti_{0.5}O_{19}$	65.5	27.1	1420
$BaFe_{11}Zn_{0.5}Ti_{0.5}O_{19}$	63.2	24.2	1082
$BaFe_{11}Co_{0.5}Ti_{0.5}O_{19}$	59.6	22.8	1137
$BaFe_{11}Mn_{0.5}Ti_{0.5}O_{19}$	56.7	26.1	1660
$BaFe_{11}Ni_{0.5}Ti_{0.5}O_{19}$	57.5	25.6	1205

3.3.3 SEM Analysis

As the bulk properties of these materials mainly depend on the grain size, SEM micrographs were taken, which are shown in Figure 3.19. The sharp and well defined hexagonal grains (homo- geneous hexagonal-shaped) have prominent grain boundaries. Samples are composed of small grains with little porosity and have relatively dense microstructure. It should be noticed that grain sizes are less than 1 mm, which is the single domain limit of BaM particles (Kittel 1949; Goto, Ito et al. 1980; Haneda and Morrish 1989).

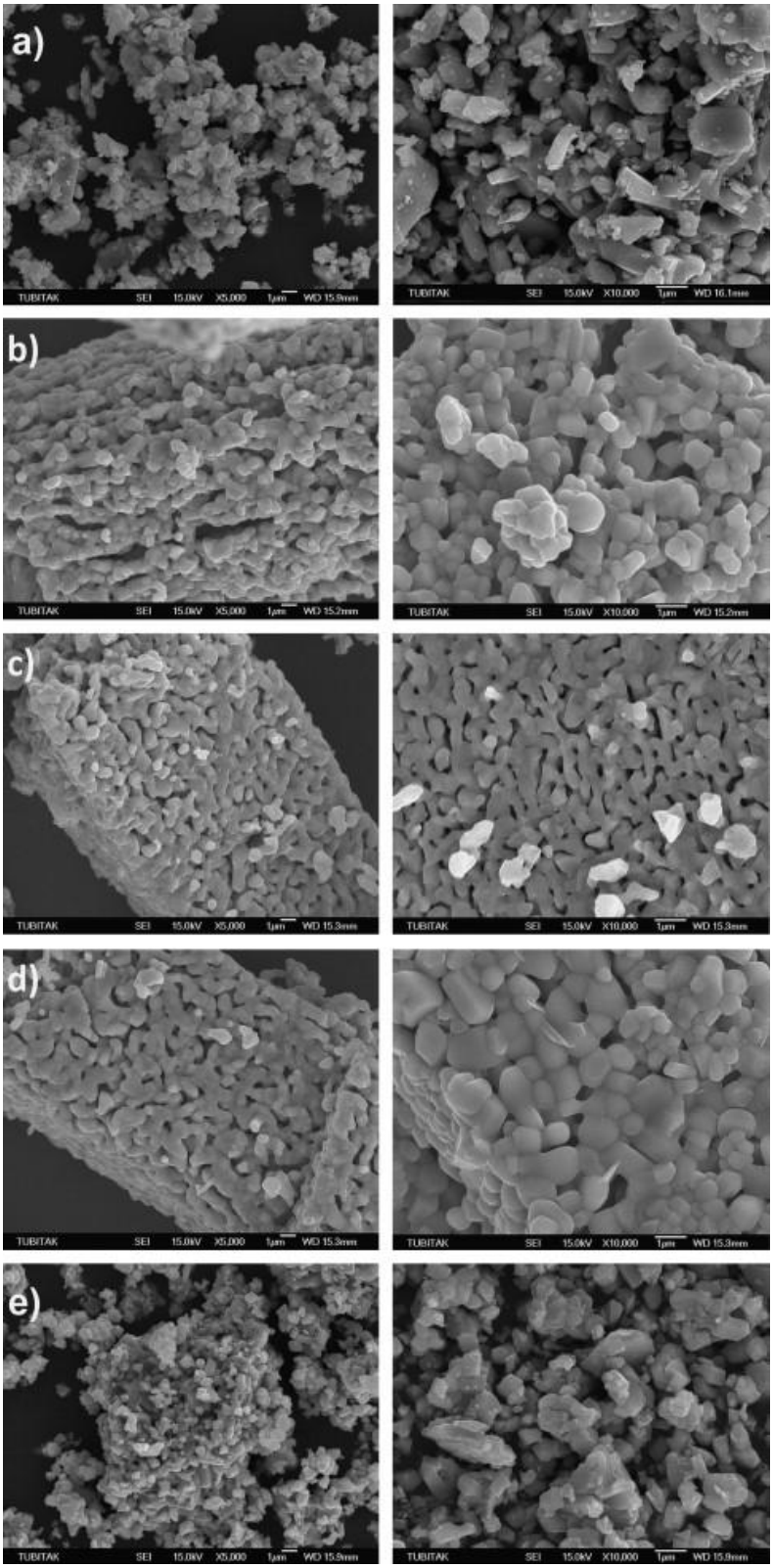

Figure 3.19 SEM micrographs of (a) Ni–Ti, (b) Zn–Ti, (c) Co–Ti, (d) Cu–Ti and (e) Cu–Ti sample.

3.3.4 MW Analysis

Figure 3.20 a and b show complex permittivity spectra between 2 and 18 GHz, which are determined from the S-parameters (S11 and S21) using the material measurement software. Real parts of permittivity and permeability values are related to the energy stored (i.e., capacitive part), while imaginary parts are related to the energy dissipation (i.e., losses) in the material.

The real and imaginary parts of the permittivity spectra are almost constant in the whole frequency range, except for the fluctuations at 11 GHz, for the Co–Ti, Cu–Ti and Zn–Ti substituted samples. Hovewer, both decreases with increasing frequency for Mn–Ti and Ni–Ti substituted specimens. Besides, real parts of the permittiviy values are considerably higher than the imaginary parts, which are very close to zero except for Mn–Ti and Ni–Ti substituted samples. This behavior is in parallel with the general tendency of hexaferrites at microwave frequencies (Ahmad, Grössinger et al. 2012; Tyagi, Verma et al. 2012; Meng, Xiong et al. 2015).

It is well-known that dielectric properties of ferrites are determined mainly by the interfacial polarization and intrinsic electric dipole polarization. The existence of low resistivity grains, which are separated by high resistivity grain boundaries, creates heterogeneous structure which causes interfacial polarization (Sözeri et al. 2015). Both formation and crystallization of ferrite particles were enhanced by sintering at high temperatures, which raises the interfacial polarization (Tyagi, Verma et al. 2012). Thus, it was observed that real and imaginary parts of permittivity increase as the sintering temperature of the ferrites increases (Haijun, Zhichao et al. 2003; Tyagi, Verma et al. 2012). The hopping of electrons between Fe^{2+} and Fe^{3+} ions on the octahedral sites causes electric polarization (Haijun, Zhichao et al. 2003). The smaller the number of electrons, the lower is the permittivity (Rado 1953; Kim and Kim 2002) which is favorable for the impedance matching condition. Figure 3.20b implies that hopping rate is high in Mn–Ti and Ni–Ti substituted samples, and thus dielectric loss is enhanced. However, strong resonance peaks were observed in complex permittivity spectra of Cu–Ti and Zn–Ti substituted samples at 11 GHz.

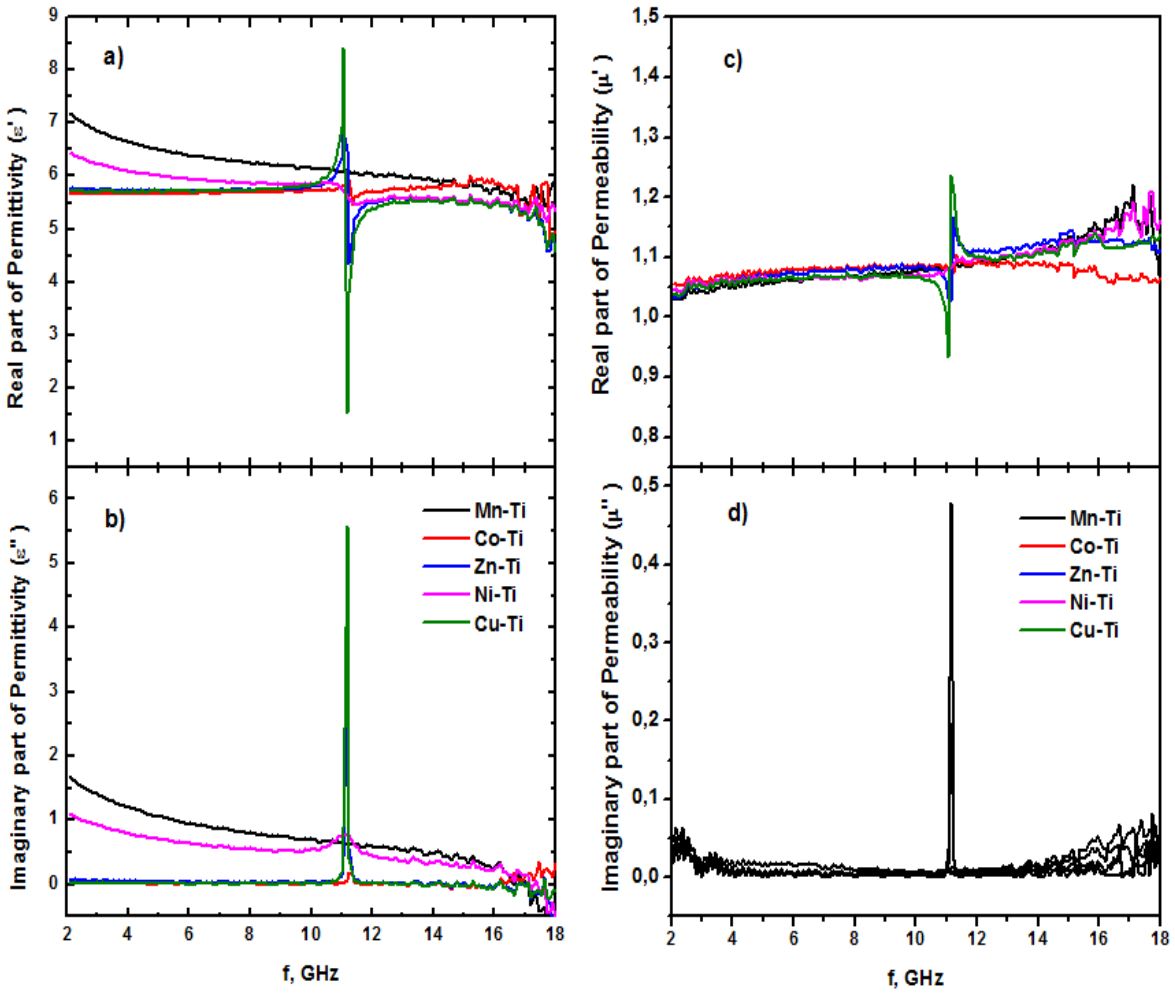

Figure 3.20 Real and imaginary parts of permittivity and permeability spectra of the samples between 2 and 18 GHz, (a) Real Part of Permittivity, (b) Imaginary Part of Permittivity, (c) Real Part of Permeability, (d) Imaginary Part of Permeability.

The real and imaginary permeability spectra of the samples are shown in Figure 3.20c and d. Both real and imaginary parts of the permeability values are constant within the 2–18 GHz range. At 11 GHz, strong resonance peaks were observed in Ni–Ti and Zn–Ti substituted samples. As the size of the ferrite particles increases, the domain wall length increases which leads to stronger domain wall vibrations (Rado 1953). It has been used solid state reaction route to synthesize barium hexaferrite particles, which may have bigger grains compared to the samples prepared with chemical routes. This could be the reason for having such strong peaks in the permeability spectra. Similarly, Ozah et al. also observed

such strong peaks in the permeability spectra of barium hexaferrite particles which were sintered at 900 °C (Ozah and Bhattacharyya 2013).

It is well-known that permeability of polycrystalline ferrites is related to two magnetizing mechanisms, namely spin rotation and domain wall motion (Stoppels 1996). The domain wall motion is affected by the grain size in such a way that as the number of domain walls increases their contribution to magnetization increases. The domain wall contribution to the permeability is of resonance type and depends on the square of frequency (Nakamura, Miyamoto et al. 2003). It decreases at low frequencies around 100 MHz (Nakamura, Miyamoto et al. 2003). On the other hand, spin rotational contribution is of relaxation type and is inversely proportional to the frequency. The complex permeability spectra at high frequencies can be described by spin rotation (Rado 1953). Thus, resonances observed in Figure 3.20c and d are most probably due to the spin rotation contribution. It should be also noticed that the value of m' is considerably smaller than that of ε', which is the case for ferrites at microwave frequencies (Tyagi, Verma et al. 2012; Ozah and Bhattacharyya 2013).

Reflection loss (RL) values for the samples were calculated using complex permittivity and permeability values using the equation (3.3)

The absorption spectra of the samples between 2 and 18 GHz are shown in Figure 3.21. Zn–Ti substituted sample having a thickness of 3 mm has the minimum RL value of — 34 dB at 10 GHz with 1.6 GHz bandwidth at — 20 dB. The minimum RL values of other samples vary between — 24 and — 30 dB with very close resonance frequencies, see Table 3.9. It appeared that impedance matching occurs at around 10 GHz for all samples with 3 mm thicknesses. It has been have succeeded to get quite high RL values at 10 GHz, which coincides with the working frequency of some military radars used for airborne and shipborne surveillance and navigation (Sözeri et al. 2015).

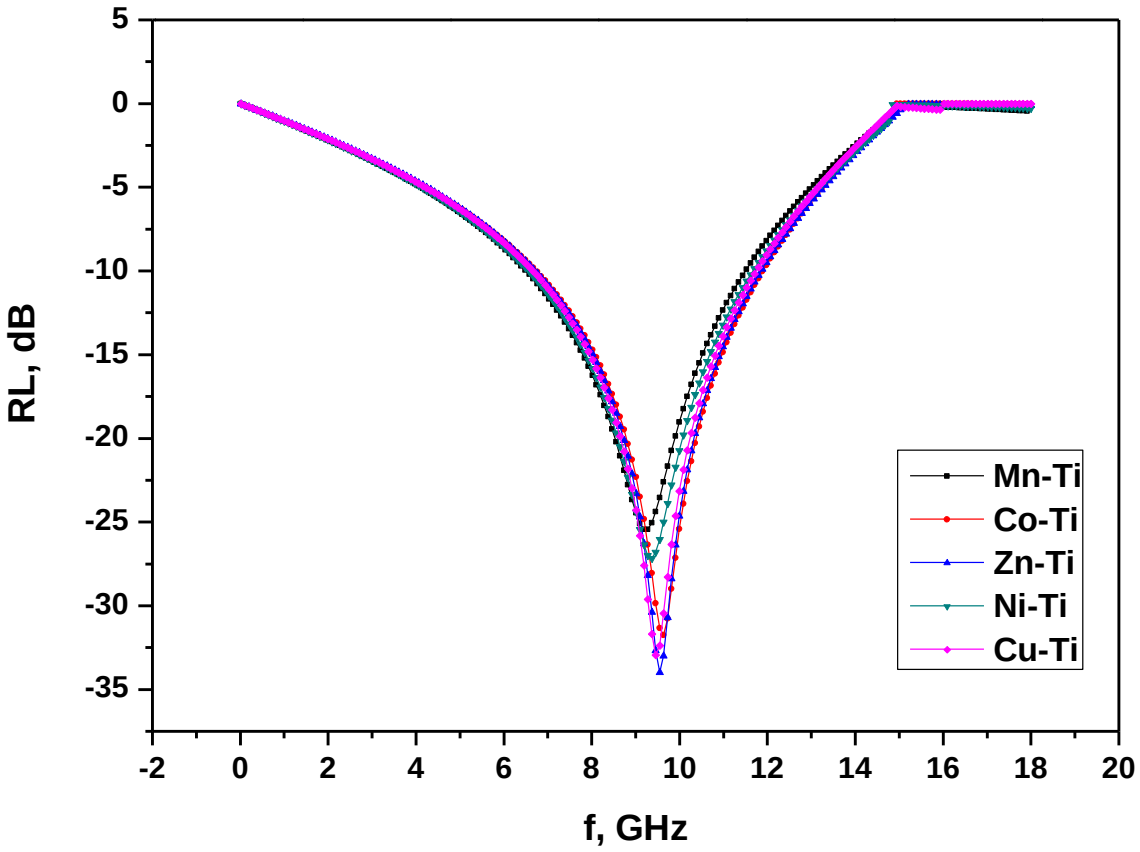

Figure 3.21 RL values of Cu–Ti, Zn–Ti, Co–Ti, Mn–Ti and Ni–Ti substituted barium hexaferrite samples in 2–18 GHz range.

Table 3.9 RL values, resonance frequencies and absorption bandtwidths of the samples in the 2–18 GHz range.

$BaFe_{11}X_{0.5}Ti_{0.5}O_{19}$	RL (dB)	Resonance frequency (GHz)	Bandwidth (GHz)
$BaFe_{11}Cu_{0.5}Ti_{0.5}O_{19}$	-32.9	9.45	1.6
$BaFe_{11}Zn_{0.5}Ti_{0.5}O_{19}$	-34	9.54	1.6
$BaFe_{11}Co_{0.5}Ti_{0.5}O_{19}$	-31.7	9.6	1.6
$BaFe_{11}Mn_{0.5}Ti_{0.5}O_{19}$	-25.5	9.2	1.4
$BaFe_{11}Ni_{0.5}Ti_{0.5}O_{19}$	-27.1	9.4	1.4

It is also possible to absorb microwave energy at two different frequencies with different dissipation mechanisms; one is, for example, due to the impedance matching and another is due to the tangent losses. Tabatabaie et al. (Tabatabaie, Fathi et al. 2009; Tabatabaie, Fathi et al. 2009) observed such two resonance peaks in RL spectra of Mn–Ti and Co–Ti substitutions to strontium hexaferrite (SrM). The resonances occur at 18.84 GHz with RL value of — 26 dB and at 19.5 GHz having RL value of — 42 dB. Similarly, Mg–Ti ions were substituted into three Fe^{3+} ions in barium hexaferrite and two resonance peaks were observed at 14.7 and 16.44 GHz with — 49.69 and — 45.65 dB values, respectively (Shams, Salehi et al. 2008).

The RL spectra of Zn–Ti substituted barium hexaferrite for different thicknesses are shown in Figure 3.22. 2 mm thick sample has a RL value of — 50 dB at 14.6 GHz with the resonance bandwidth of 2.6 GHz at — 20 dB. As the thickness of the sample increases, the resonance peak shifts to lower frequencies. Similarly, the same relation between the matching thickness and the resonance frequency was observed in W- type hexaferrite powders by Ahmad et al.(Ahmad, Grössinger et al. 2012), in $BaMg_{0.25}Mn_{0.25}Co_{0.5}Ti_{1.0}Fe_{10}O_{19}$ by Tehrani at al. (Tehrani, Ghasemi et al. 2011) and in $CaNi_xTi_xFe_{12}\ O_{19}$ by Singh et al. (Singh, Babbar et al. 2000). In addition, the resonance frequency decreases exponentially with matching thickness in 2–18 GHz range, as shown in Figure 3.23. Singh et al. reported that matching thickness varies linearly with resonance frequency in a narrow range between 9 and 12 GHz. The results in the same frequency range reveal that matching thicknesses varying between 2 and 4 mm can also be fitted linearly. However, when samples having thicknesses up to 10 mm are considered, it appears that there is an exponential type relation between the matching thickness and the resonance frequency.

Moreover, in Figure 3.23, Zin (impedance of the material that incident wave is faced) value graphs of the samples are drawn with respect to frequency. Zin implies how incident EMW penetrates to the sample. In order to be invisible to radars, incident EMW should penetrate to the sample just like as it is in the air. Air impedance for an incident EMW is taken as reference so that where Zin becomes 1, it is said the fact that, that sample have impedance just like in air; in other words, samples behaves just like air for incident

EMW, they have full penetration at the frequencies of which Zin value of that sample becomes 1. For X-Ti doped BaM samples, all samples have full penetration at their MW absorption frequencies but Co-Ti doped sample.

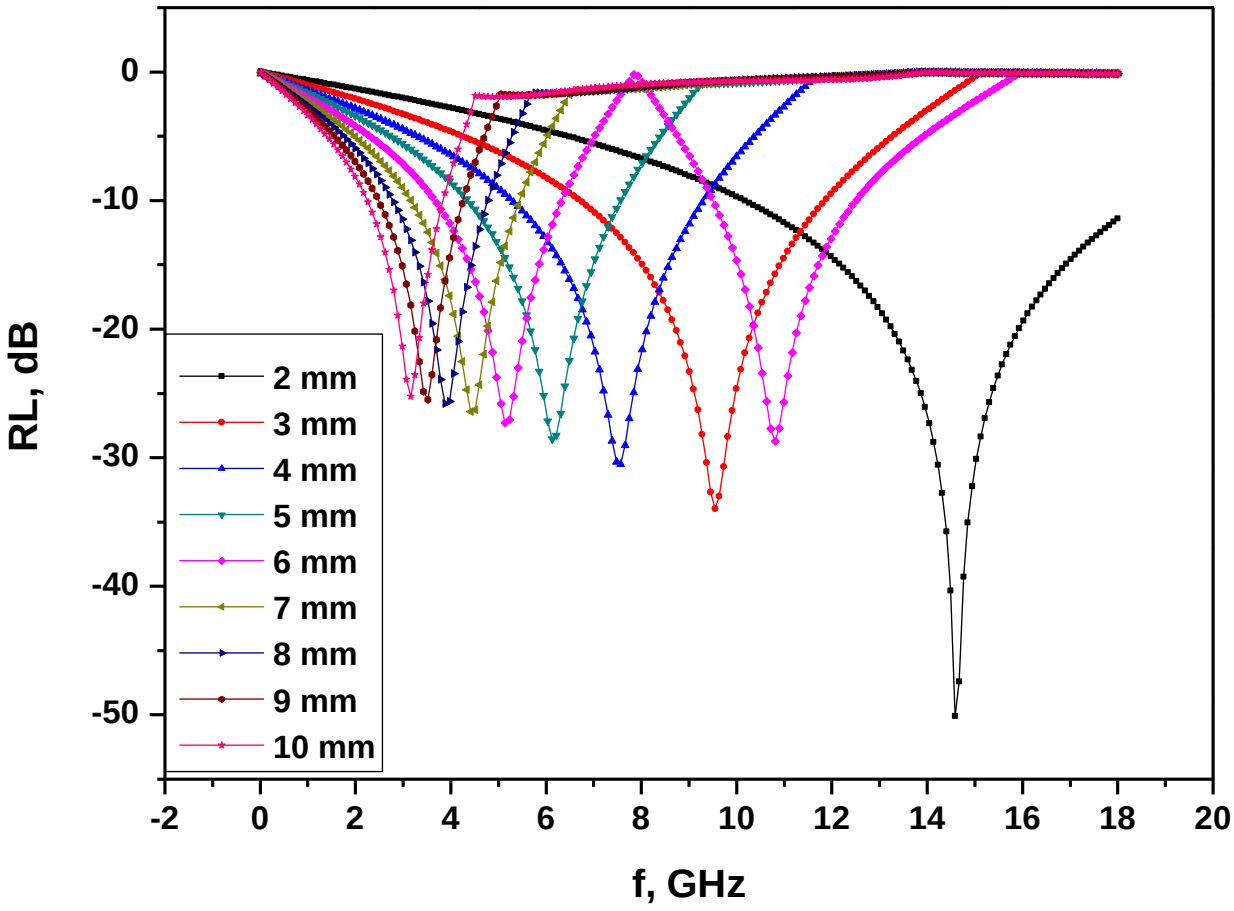

Figure 3.22 RL values of Zn-Ti substituted samples having various thicknesses between 2 and 10 mm.

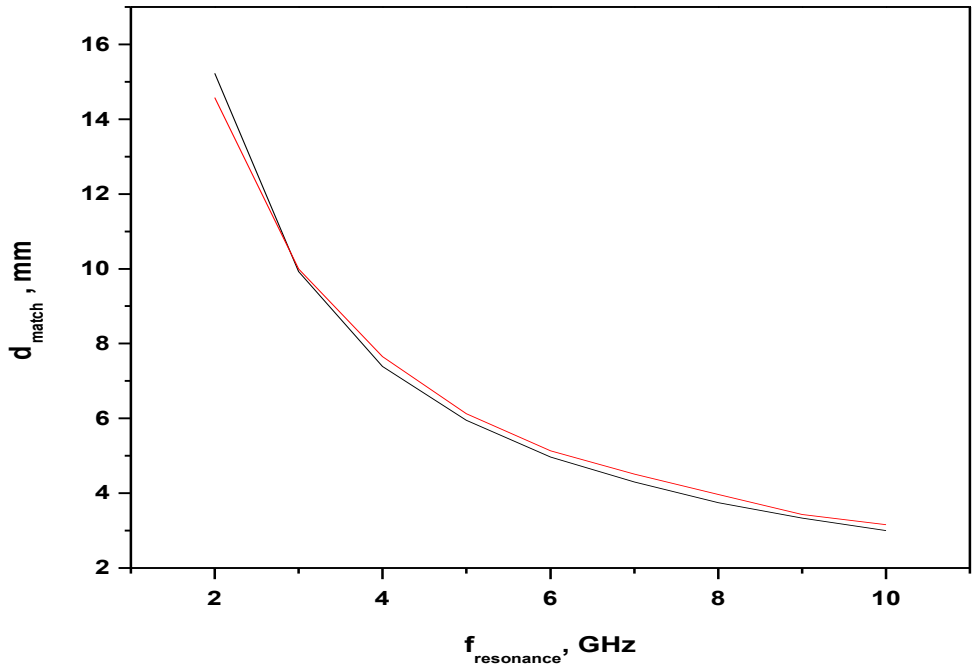

Figure 3.23 Resonance frequencies of Zn-Ti substituted samples at different sample thicknesses. The solid line represents the exponentially fitted curve.

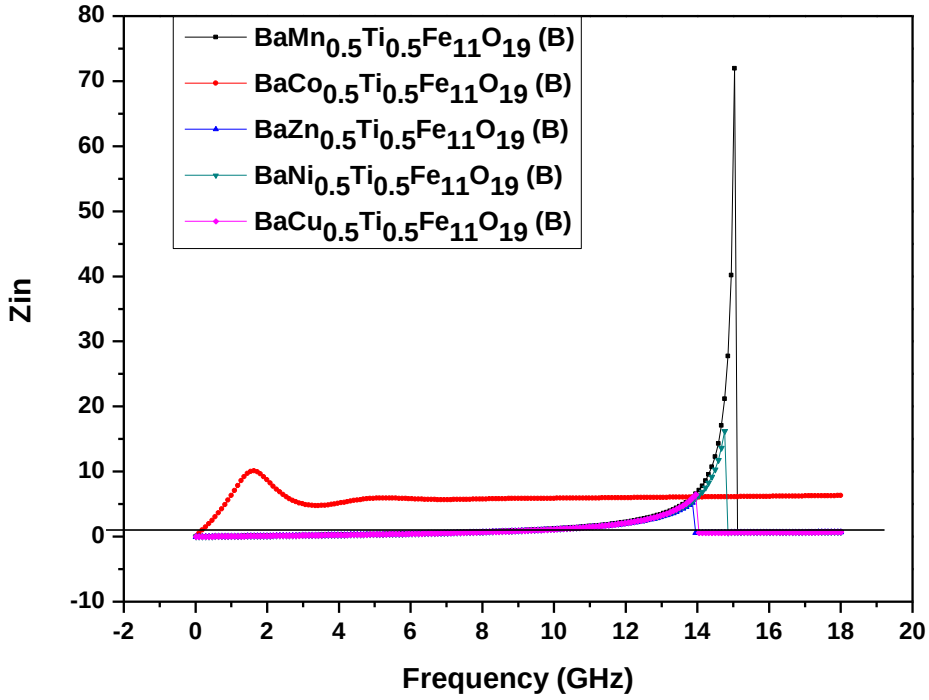

Figure 3.24 Zin values of the samples.

In conclusion, Cu^{2+} , Mn^{2+} , Zn^{2+} , Ni^{2+} , Co^{2+} and Ti^{4+} ions were replaced by one Fe^{3+} ion in barium hexaferrite in the form of $BaX_{0.5}Ti_{0.5}Fe_{11}O_{19}$ (X^{2+} = Cu, Ni, Mn, Co and Zn) which was synthesized by conventional solid state reaction. 1% B_2O_3 was added to inhibit crystal growth at low temperatures. XRD patterns showed that barium hexaferrite phase was successfully obtained with average grain sizes less than 1 μm, which is the single domain limit of this material. Magnetization measurements revealed that Cu^{2+}–Ti^{4+} and Zn^{2+} –Ti^{4+} substituted samples have higher magnetization values, compared to other samples, which has been explained by site preferences of substituted ions in Fe^{3+} sublattices and enhanced exchange interaction between Fe^{2+} and Fe^{3+} ions. Microwave characterization of the composites having a thickness of 3 mm showed that all the samples have nearly the same resonance frequency around 10 GHz with varying RL values between — 24 and — 34 dB. Resonance bandwidths of 1.6 GHz were obtained at — 20 dB. The mechanism of absorption is due to the impedance matching. In addition, it was also observed that when sample thickness varies between 2 and 10 mm, the resonance frequency decreases from 15 to 3 GHz exponentially. Finally, it is observed that by varying the thickness of the absorber, the resonance frequency of the hexaferrite material can be tuned to a specific value.

3.4 SYNTHESIS of BORON ADDED LEAD, BARIUM AND STRONTIUM DOPED HEXAFERRITE PREPARED with BALL MILLING

3.4.1 XRD Analysis

Figure 3.25 shows XRD powder patterns of samples. According to standard data obtained from M-type of $BaFe_{12}O_{19}$ (JCPDS Patterns no. 84-0757), XRD patterns show the fact that BaM hexaferrite structure is succesfully synthesized. Starred impurity is α-Fe_2O_3 (JCPDS Patterns no. 86-0550), for the samples which Sr doping is in high ratio comparing to other dopes, impurity intensity is high. The sample that has the highest Sr content (BM $Ba_{0,3}Sr_{0,4}Pb_{0,3}Fe_{12}O_{19}$(B)) has the highest impurity intensty.

In addition, by means of Eqn. (3.1), miller indices and lattice parameters of samples are calculated. There is no change in lattice parameters with doping Pb, Sr and Ba into the

original hexaferritte crystal (Table 3.10). In order to comment further, cation distribution and annealing temperature change study should be applied.

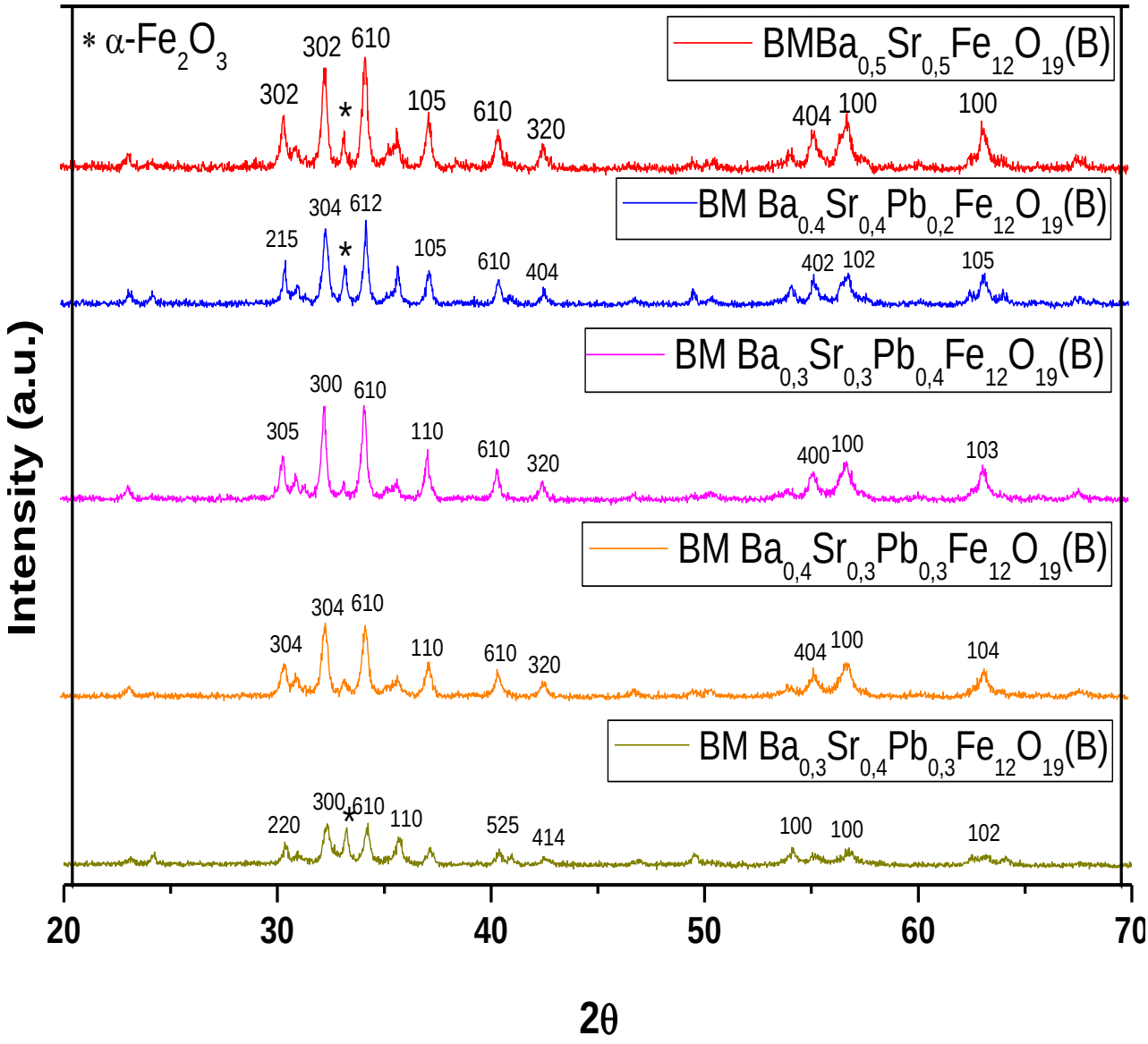

Figure 3.25 XRD spectra with Rietveld analysis patterns of Ba, Sr and Pb substituted hexaferrites.

Table 3.10 Lattice parameters of Ba, Sr and Pb substituted hexaferrites.

	a (Å)	c (Å)
$Ba_{0,5}Sr_{0,5}Fe_{12}O_{19}$	5,89	22,94
$Ba_{0.4}Sr_{0,4}Pb_{0,2}Fe_{12}O_{19}$(B)	5,89	22,94
$Ba_{0,3}Sr_{0,3}Pb_{0,4}Fe_{12}O_{19}$(B)	5,89	22,94
$Ba_{0,4}Sr_{0,3}Pb_{0,3}Fe_{12}O_{19}$(B)	5,89	22,94
$Ba_{0,3}Sr_{0,4}Pb_{0,3}Fe_{12}O_{19}$(B)	5,89	22,94

3.4.2 SEM Analysis

In Figure 3.26, SEM images of ball milled Ba, Sr and Pb substituted barium hexaferrites are shown with different magnifications for each samples. As seen in the micrographs, hexaferrite domains are less than 1μm which is defined as single domain limit. Since the samples in Figure 3.26 have been processed with ball mill, smaller domain size is observed. In addition, by also the contributions of both VSM (Figure 3.18) and XRD (Figure 3.25) analyses, as Sr substitution ratio increases, impurity phase is increases; the highest impurity content is in $Ba_{0,3}Sr_{0,4}Pb_{0,3}Fe_{12}O_{19}$(B) sample. Small impurity particles that are seen in the Figure 3.26 are α-Fe_2O_3. The samples shown in Figure 3.26 (c) and (d) have dominantly Ba content; therefore, in these samples, α-Fe_2O_3 is there with fewer amounts comparing to other samples.

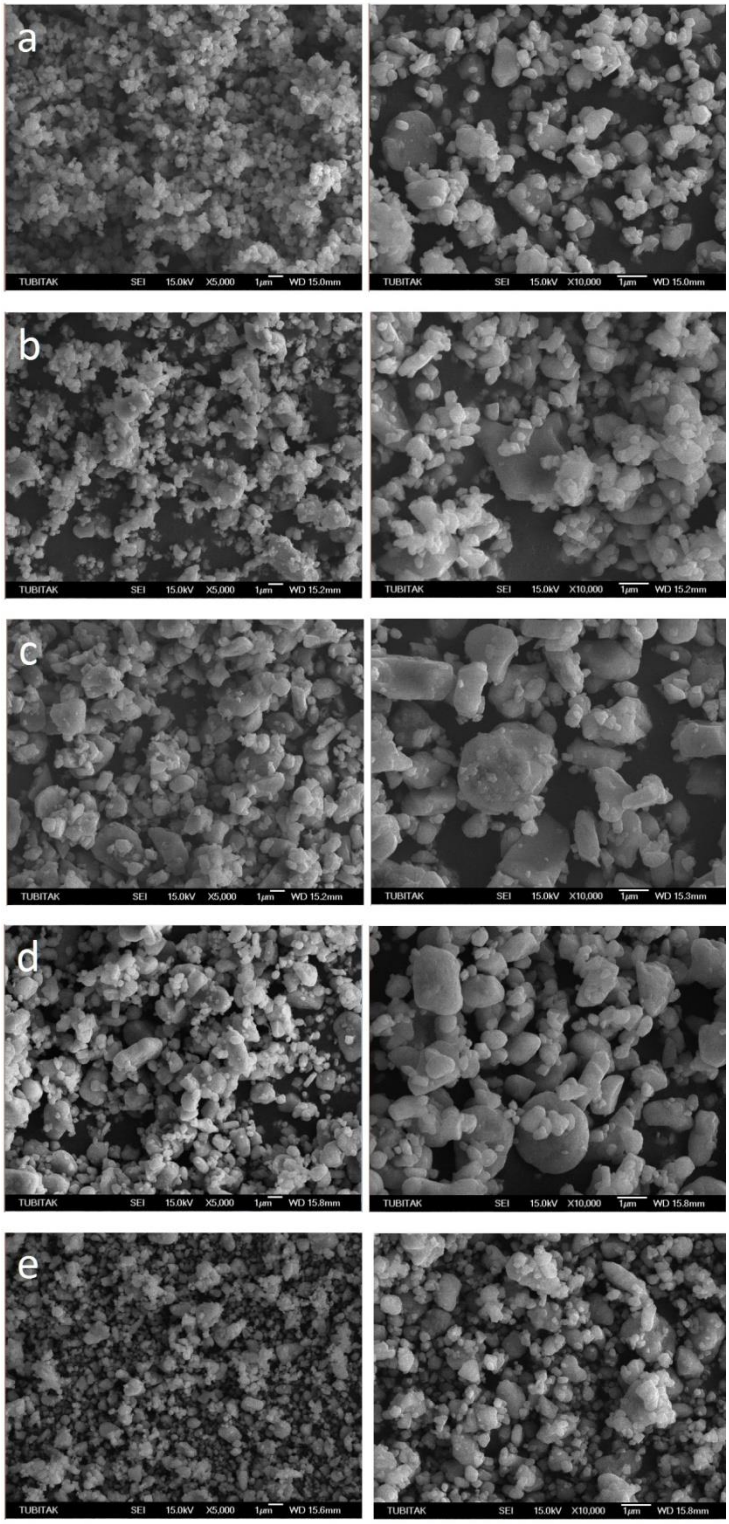

Figure 3.26 SEM micrographs of ball milled Ba, Sr and Pb substituted hexaferrites (a)$Ba_{0,5}Sr_{0,5}Fe_{12}O_{19}$(B) (b)$Ba_{0.4}Sr_{0,4}Pb_{0,2}Fe_{12}O_{19}$(B) (c)$Ba_{0,3}Sr_{0,3}Pb_{0,4}Fe_{12}O_{19}$(B) (d)$Ba_{0,4}Sr_{0,3}Pb_{0,3}Fe_{12}O_{19}$(B) (e)$Ba_{0,3}Sr_{0,4}Pb_{0,3}Fe_{12}O_{19}$(B).

3.4.3 VSM Analysis

As seen in Figure 3.27 doping lead ion into the hexaferrite structure decreases the magnetic saturation as well as coercive field. Ba and Sr ions have remarkably higher magnetization than other ions. Pb ion is used to improve dielectric properties of the samples; hence, when Pb replaces the position of Ba ad Sr ions in hexaferrite crystal structure, both the saturation magnetization and coercive field is decreased. Between Ba and Sr, Ba ion is preferred to be doped to hexaferrite structure because of its higher magnetization than Sr ion. As a result, doping lead ion with respect to decreasing the amount of barium content make sample have even lower saturation magnetization and coercive field.

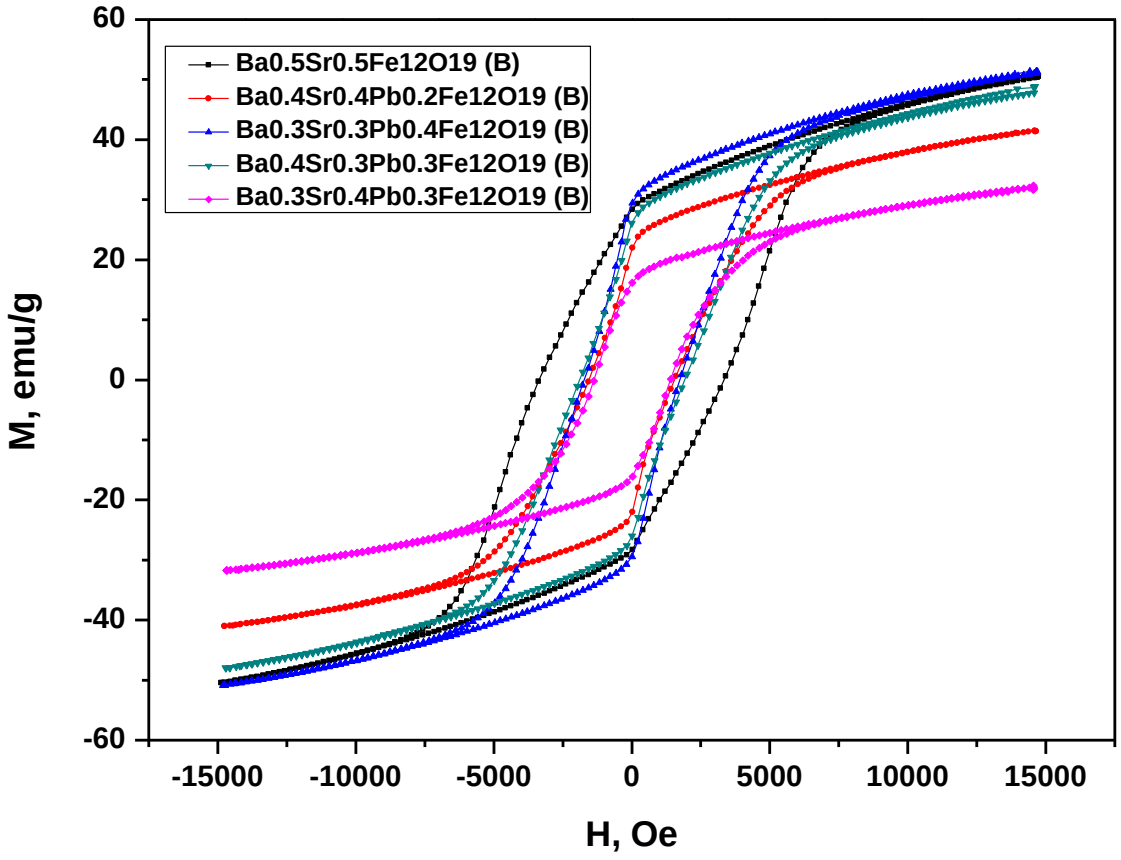

Figure 3.27 M-H hysteresis curves of Ba, Sr and Pb substituted hexaferrites.

3.4.3 MW Analysis

According to equation (3.3), calculations of RL graphs are done.

The absorption spectra of the samples between 0 and 18 GHz are shown in Figure 3.28. Ba, Sr and Pb substituted BaM samples having a thickness of 3 mm has RL peak value approximately of — 35 dB at 10 GHz with 2 GHz bandwidth at — 20 dB. The RL behaviors of all samples are very close to each other. It appeared that impedance matching occurs at around 10 GHz for all samples with 3 mm thicknesses. It has been succeeded to get quite high RL values at 10 GHz, which coincides with the working frequency of some military radars used for airborne and shipborne surveillance and navigation (Sözeri et al. 2015).

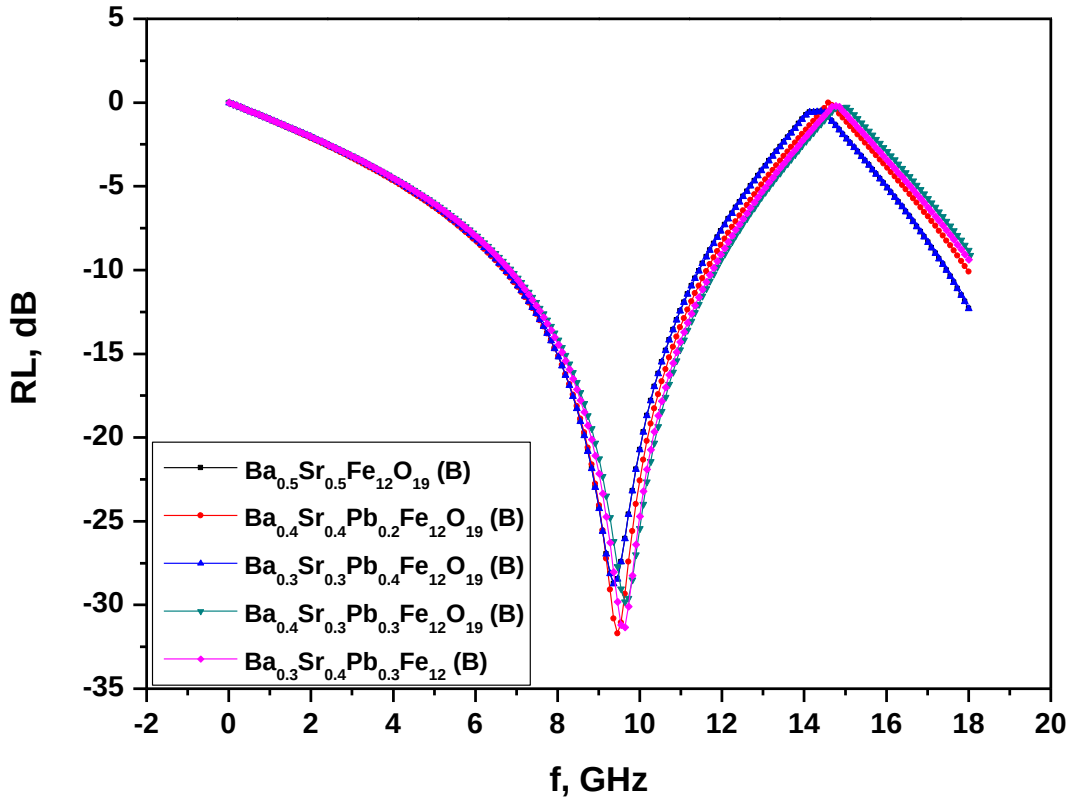

Figure 3.28 RL values of BaM, SrM and PbM substituted hexaferrite samples in 0–18 GHz range.

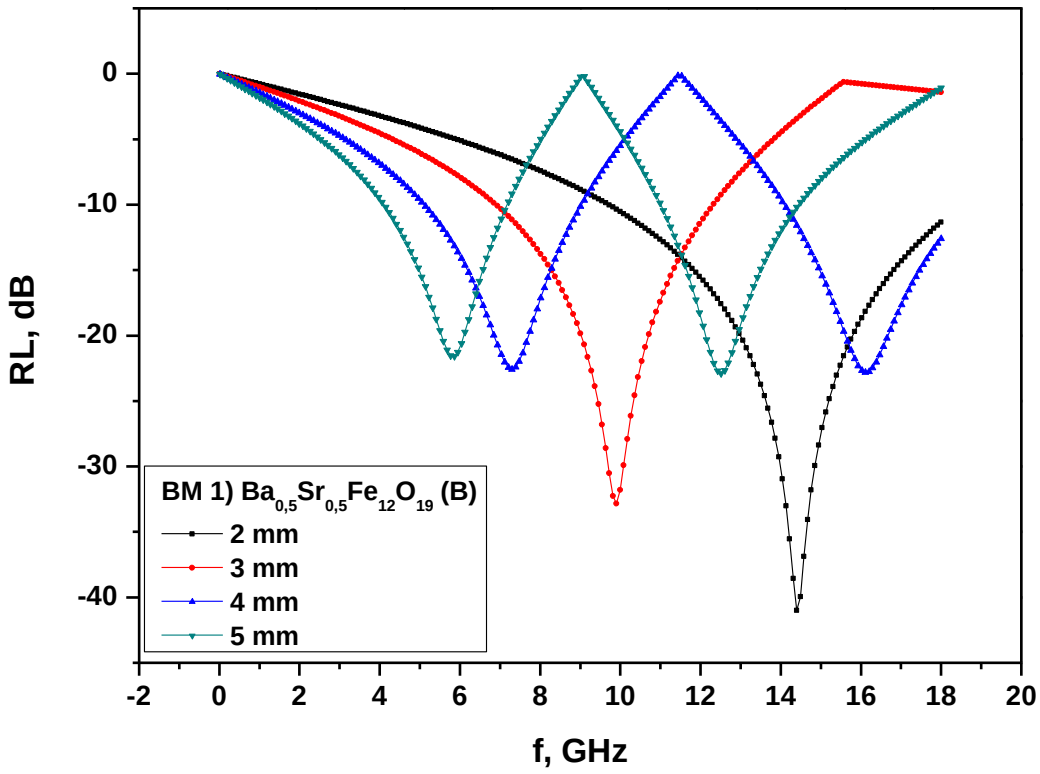

(a) $Ba_{0,5}Sr_{0,5}Fe_{12}O_{19}$ sample with boron addition and ball milled.

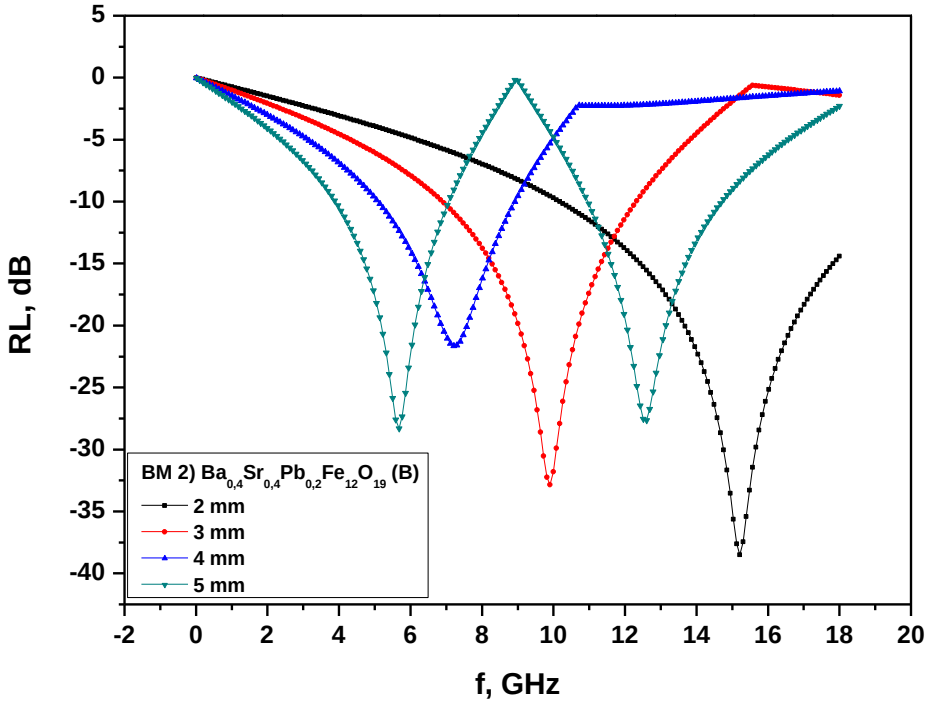

(b) $Ba_{0,4}Sr_{0,4}Pb_{0,2}Fe_{12}O_{19}$ sample with boron addition and ball milled.

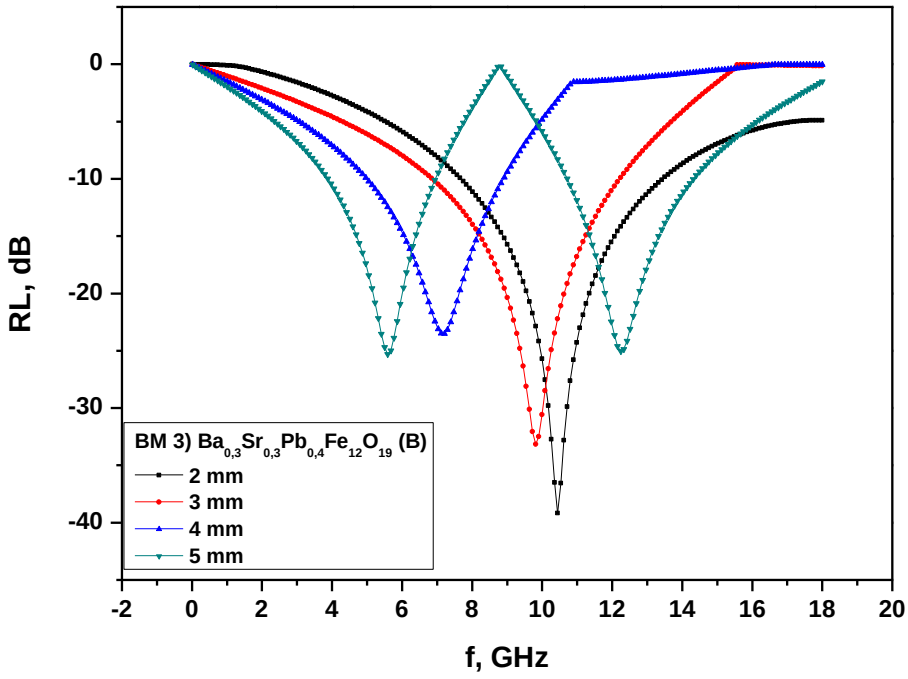

(c) $Ba_{0,3}Sr_{0,3}Pb_{0,3}Fe_{12}O_{19}$ sample with boron addition and ball milled.

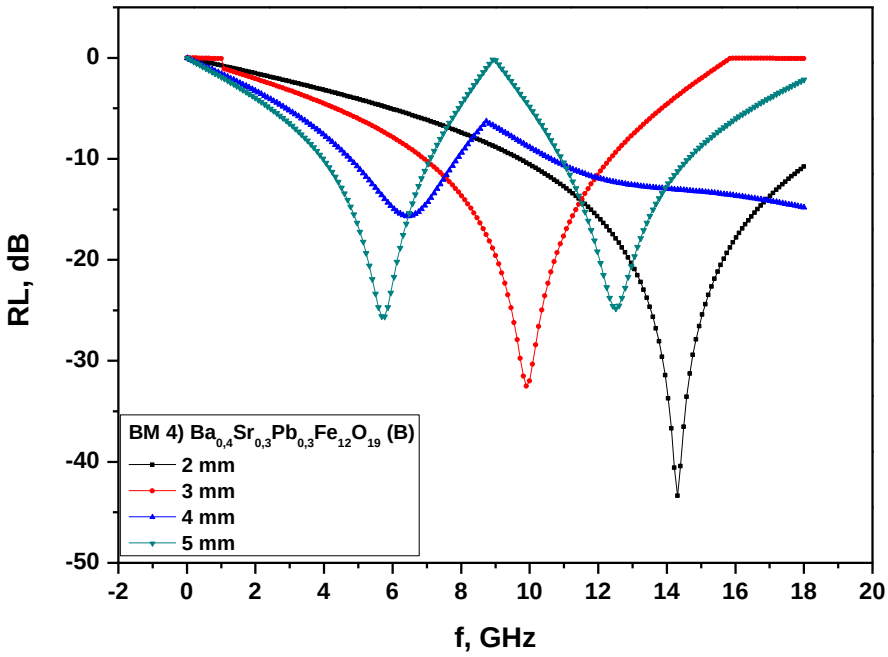

(d) $Ba_{0,4}Sr_{0,3}Pb_{0,3}Fe_{12}O_{19}$ sample with boron addition and ball milled.

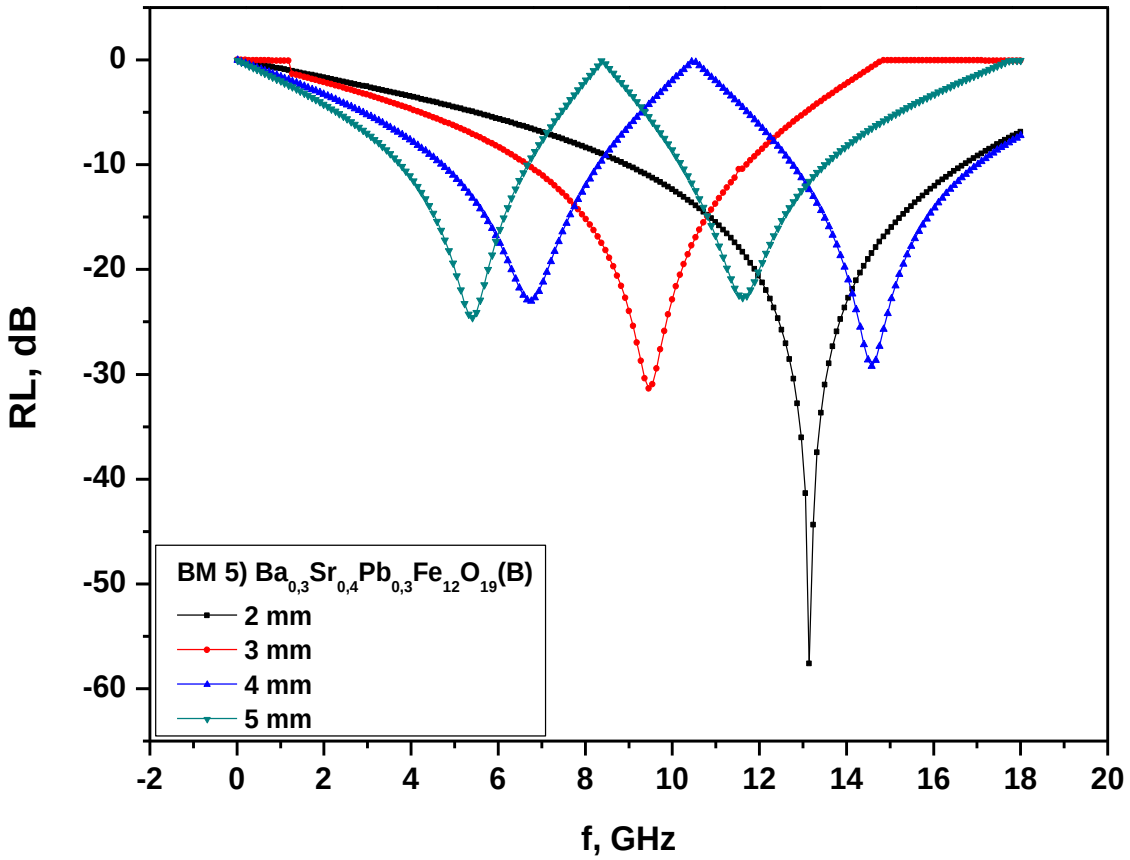

(e) $Ba_{0,3}Sr_{0,4}Pb_{0,3}Fe_{12}O_{19}$ sample with boron addition and ball milled.

Figure 3.29 RL values of Ba, Sr and Pb substituted, ball milled hexaferrite samples in 0–18 GHz range, (a) $Ba_{0,5}Sr_{0,5}Fe_{12}O_{19}$(B); (b) $Ba_{0,4}Sr_{0,4}Pb_{0,2}Fe_{12}O_{19}$(B); (c) $Ba_{0,3}Sr_{0,3}Pb_{0,3}Fe_{12}O_{19}$(B); (d) $Ba_{0,4}Sr_{0,3}Pb_{0,3}Fe_{12}O_{19}$(B); (e) $Ba_{0,3}Sr_{0,4}Pb_{0,3}Fe_{12}O_{19}$(B).

Ball milling process is applied to Ba, Sr and Pb substituted hexaferrites to get smaller domain size. For both magnetic and MW absorbing properties are depend on domain size directly. Domain-domain interaction, net magnetic dipole moment magnitude and strength are depending on domain sizes. Changing domain size may improve or diminish magnetization and MW absorption of samples. Diminish effect of ball milling process to magnetization may due to be weaker exchange interaction between domains. If destructive interference of magnetic moments for net dipole moment elimination is done by having

smaller-size domains magnetization becomes higher. For MW absorption phenomena same comments could be done with an addition, as domains get smaller, surface area and the quantities of absorbing material is increased; so, more absorbing material means higher and wider absorption values and ranges. For those of Ba, Sr and Pb substituted hexaferrites, with comparing Figure 3.29 and Figure 3.28, ball milling, smaller domain sizes, improve MW absorptions. In Figure 3.29, all samples that in Figure 3.28 are processed by ball mill (900 rpm 4 cycles 15 minute breaks 1mm zirconium balls). Ball milled samples are prepared by differing the sample thickness from 2 to 5 mm. $Ba_{0,3}Sr_{0,4}Pb_{0,3}Fe_{12}O_{19}$(B) sample having the thickness of 2 mm has a RL peak value at -57,6 dB at 13 GHz with 4 GHz bandwidth at -20 dB.

CHAPTER 4

CONCLUSIONS

In this study, BaM and SrM powders have been synthesized by solid state method in a wide range of temperature between 800 and 1200°C. High temperature provides energy to domain to have bigger size. Boron addition to those of samples makes great difference in magnetic properties. At 800°C, BaM phase is formed by means of 1% (w/w) boron addition. At 1200°C, boron added SrM sample shows soft magnetic behavior; whereas, pure SrM sample is hard magnet at same temperature. Optimum Fe/Ba and Fe/Sr ratios were determined by coercive field and saturation magnetization values. For pure BaM samples, optimum Fe/Ba ratio is 10.5, for boron added BaM samples, optimum ratio becomes 11.5; and, for SrM samples, optimum Fe/Sr ratio is 12. Optimum annealing temperature is 1000°C for both BaM and SrM samples.

Secondly, Mg, Ti and transition metal ions (Mn, Co, Ni, Cu, Zn) were replaced with one Fe^{+3} ion in BaM ($BaMg_{0.25}X_{0.25}Ti_{0.5}Fe_{11}O_{19}$). Lattice parameters of doped samples were calculated. Because of larger ionic size of Cu^{+2} ion comparing to Fe^{+3}, elongation of crystal structure was obtained. Grains did not exceed 1μm which is single domain limit. Mg-Ni-Ti and Mg-Mn-Ti substituted samples have saturation magnetization values as 60 emu/g and 50 emu/gr respectively; other samples have saturation magnetization between these two values. Strength of superexchange interaction between ions in crystal structure is determined by site preferences of doped ions. Doped ions may occupy ferromagnetically ordered tetrahedral or antiferromagnetically ordered octahedral sites; according to location of ions, saturation magnetization is affected. At about 10 GHz, all samples have RL minima varying from -27,4 dB to -34 dB due to quarter wave cancellation (matching thickness).

At k-band frequencies, Mn, Ni and Zn doped BaM samples have one more RL peak which is due to characteristic absorption. 3 mm thick Mg-Mn-Ti substituted barium hexaferrite has the best microwave absorbing properties in 2-26,5 GHz range with RL values of -30 dB at 9.6 and 19.2 GHz. Different sample thickness RL graphs were calculated by this sample. For 2 mm thick sample, -45 dB absorption can be obtained at 14.7 GHz with bandwidth of 2.7 GHz at -20 dB in 2-18 GHz range. RL minima due to quarter wave cancellation shifts from 10 GHz to lower frequencies as the thickness of samples increases to 10mm.

Thirdly, transition metal ions and Ti are replaced to boron added BaM samples with following ratios, $BaX_{0.5}Ti_{0.5}Fe_{11}O_{19}$. Cu-Ti and Zn-Ti substituted samples have higher saturation magnetization values comparing to other samples. High magnetization values can be commented according to their site preferences in hexaferrite crystal structure. All samples have RL absorption peak at around 10 GHz varying from — 24 to — 34 dB. For 2mm thick of Zn-Ti doped sample has a calculated RL minimum as — 53 dB at about 14 GHz with approximately 1.6 GHz bandwidth. Moreover, exponential varying of d (2-10 mm) with respect to f (0-26.5 GHz) is observed for larger range of frequency. Sözeri et al. investigated magnetic, dielectric and microwave properties of very similar formulation with same preparation route at 2014 (Sözeri, Deligöz et al. 2014). In that research, $BaFe_{10}M^{2+}Ti^{4+}O_{19}$ (M=Mn, Co, Ni, Cu, Zn) samples were analyzed. These samples have minimum reflection loss values slightly less than -10 dB at around 15 GHz. By rearranging the ratio of substitution, RL minimum decrease from -10 dB to -53 dB.

Finally, instead of replacing Fe ion in hexaferrite crystal structure by doped ions, Ba and Sr ions are replaced by varying ratios: $Ba_xSr_yPb_zFe_{12}O_{19}$ (x, y= 0.3, 0.4, 0.5 z= 0, 0.2, 0.3, 0.4). %1 (w/w) boron added samples were ball milled. Pb and Sr doping decrease saturation magnetization, Pb doping with decreasing Ba content make the sample have even less saturation magnetization. Due to well-known fact that Sr and Pb have lower magnetization, results were as expected. Sr rich content sample ($Ba_{0,3}Sr_{0,4}Pb_{0,3}Fe_{12}O_{19}$) has the highest purity as α-Fe_2O_3. 2mm thick ball milled $Ba_{0,3}Sr_{0,4}Pb_{0,3}Fe_{12}O_{19}$ sample has the highest calculated RL minimum as— 57 dB at about 13 GHz with approximately 1.5 GHz bandwidth.

REFERENCES

Ahmad, M., Grössinger, R., Kriegisch, M., Kubel, F., & Rana, M. U. (2012). Magnetic and microwave attenuation behavior of Al-substituted Co 2W hexaferrites synthesized by sol-gel autocombustion process. *Current Applied Physics, 12*(6), 1413-1420. doi: 10.1016/j.cap.2012.02.038

Belous, A. G., V'Yunov, O. I., Pashkova, E. V., Ivanitskii, V. P., & Gavrilenko, O. N. (2006). Mössbauer study and magnetic properties of M-type barium hexaferrite doped with Co + Ti and Bi + Ti ions. *Journal of Physical Chemistry B, 110*(51), 26477-26481. doi: 10.1021/jp064628t

Bish, D. L., & Howard, S. A. (1988). Quantitative phase analysis using the Rietveld method. *Journal of Applied Crystallography, 21*(2), 86-91. doi: doi:10.1107/S0021889887009415

Bragg, W. H. (1915). The structure of magnetite and the spinels. *Nature, 95*(2386), 561.

Carta, D., Casula, M. F., Falqui, A., Loche, D., Mountjoy, G., Sangregorio, C., & Corrias, A. (2009). A Structural and magnetic investigation of the inversion degree in ferrite nanocrystals MFe_2O_4 (M = Mn, Co, Ni). *Journal of Physical Chemistry C, 113*(20), 8606-8615. doi: 10.1021/jp901077c

Drofenik, M., Ban, I., Makovec, D., Žnidaršič, A., Jagličić, Z., Hanžel, D., & Lisjak, D. (2011). The hydrothermal synthesis of super-paramagnetic barium hexaferrite particles. *Materials Chemistry and Physics, 127*(3), 415-419. doi: http://dx.doi.org/10.1016/j.matchemphys.2011.02.037

Durmuş, Z. (2013). Synthesis and characterization of hexaferrite nanoparticles and nanocomposites. *Ph.D Thesis*, Fatih University.

González-Angeles, A., Mendoza-Suarez, G., Grusková, A., Papa´Nová, M., & Slama, J. (2005). Magnetic studies of Zn-Ti-substituted barium hexaferrites prepared by mechanical milling. *Materials Letters, 59*(1), 26-31. doi: 10.1016/j.matlet.2004.09.012

Goto, K., Ito, M., & Sakurai, T. (1980). Studies o Magnetic Domains of Small Particles of Barium Ferrite by Colloid-Sem Method. *Japanese journal of applied physics, 19*(7), 1339-1346.

Haijun, Z., Zhichao, L., Xi, Y., Liangying, Z., & Mingzhong, W. (2003). Complex permittivity and permeability dependence of Ba_4Zn_2-$CoFe_{36}O_{60}$ U-type hexaferrites prepared by citrate sol-gel on composition, annealing temperature and frequency. *Materials Science and Engineering B: Solid-State Materials for Advanced Technology, 97*(2), 160-166. doi: 10.1016/s0921-5107(02)00571-8

Haneda, K., & Morrish, A. H. (1989). Magnetic properties of $BaFe_{12}O_{19}$ small particles. *IEEE Transactions on Magnetics, 25*(3), 2597-2601. doi: 10.1109/20.24496

Hemeda, D. M., & Hemeda, O. M. (2008). Electrical, structural, magnetic and transport properties of $Zn_2BaFe_{16}O_{27}$ doped with Cu^{2+}. *Journal of Magnetism and Magnetic Materials, 320*(8), 1557-1562. doi: 10.1016/j.jmmm.2008.01.006

http://www.cttc.es/en/projects/testbeds/project/achamber.jsp/.

http://www.ecanechoicchambers.com/TB/EB-130%20-%20HFX-HC.pdf.

Iqbal, M. J., Ashiq, M. N., & Hernandez-Gomez, P. (2009). Effect of annealing temperature and substitution of Zr-Cu on magnetic properties of strontium hexaferrite nanoparticles. *Journal of Physics: Conference Series, 153*. doi: 10.1088/1742-6596/153/1/012053

Janasi, S. R., Rodrigues, D., Landgraf, F. J. G., & Emura, M. (2000). Magnetic properties of coprecipitated barium ferrite powders as a function of synthesis conditions. *Magnetics, IEEE Transactions on, 36*(5), 3327-3329. doi: 10.1109/20.908788

Kanagesan, S., Jesurani, S., Velmurugan, R., & Kalaivani, T. (2012). Preparation and magnetic properties of Ni-Zr doped barium strontium hexaferrite. *Journal of Materials Science: Materials in Electronics, 23*(4), 952-955. doi: 10.1007/s10854-011-0526-3

Kim, Y. J., & Kim, S. S. (2002). Microwave absorbing properties of Co-substituted Ni2W hexaferrites in Ka-band frequencies (26.5-40 GHz). *IEEE Transactions on Magnetics, 38*(5 I), 3108-3110. doi: 10.1109/tmag.2002.802483

Kittel, C. (1949). Physical theory of ferromagnetic domains. *Reviews of Modern Physics, 21*(4), 541-583. doi: 10.1103/RevModPhys.21.541

Kneller, E. F., & Hawig, R. (1991). The exchange-spring magnet: A new material principle for permanent magnets. *IEEE Transactions on Magnetics, 27*(4), 3588-3600. doi: 10.1109/20.102931

Li, Y., Wang, Q., & Yang, H. (2009). Synthesis, characterization and magnetic properties on nanocrystalline $BaFe_{12}O_{19}$ ferrite. *Current Applied Physics, 9*(6), 1375-1380. doi: http://dx.doi.org/10.1016/j.cap.2009.03.002

Li, Z. W., Chen, L., & Ong, C. K. (2002). Studies of static and high-frequency magnetic properties for M-type ferrite $BaFe_{12-2x}Co_xZr_xO_{19}$. *Journal of Applied Physics, 92*(7), 3902-3907. doi: 10.1063/1.1506387

Liu, W.-T., & Wu, J.-M. (2001). The effect of the vacuum extraction and the Fe/Ba ratio on the phase formation of barium ferrite thin film synthesized by sol–gel method. *Materials Chemistry and Physics, 69*(1–3), 148-153. doi: http://dx.doi.org/10.1016/S0254-0584(00)00381-3

Liu, X., Wang, J., Gan, L.-M., & Ng, S.-C. (1999). Improving the magnetic properties of hydrothermally synthesized barium ferrite. *Journal of Magnetism and Magnetic Materials, 195*(2), 452-459. doi: http://dx.doi.org/10.1016/S0304-8853(99)00123-7

Liu, Y., Drew, M. G. B., & Liu, Y. (2012). Optimizing the methods of synthesis for barium hexagonal ferrite—An experimental and theoretical study. *Materials Chemistry and Physics, 134*(1), 266-272. doi: http://dx.doi.org/10.1016/j.matchemphys.2012.02.062

Maeda, T., Sugimoto, S., Kagotani, T., Tezuka, N., & Inomata, K. (2004). Effect of the soft/hard exchange interaction on natural resonance frequency and electromagnetic wave absorption of the rare earth–iron–boron compounds. *Journal of Magnetism and Magnetic Materials, 281*(2–3), 195-205. doi: http://dx.doi.org/10.1016/j.jmmm.2004.04.105

Mali, A., & Ataie, A. (2005). Influence of Fe/Ba molar ratio on the characteristics of Ba-hexaferrite particles prepared by sol–gel combustion method. *Journal of Alloys and Compounds, 399*(1–2), 245-250. doi: http://dx.doi.org/10.1016/j.jallcom.2005.03.017

Mariño-Castellanos, P. A., Somarriba-Jarque, J. C., & Anglada-Rivera, J. (2005). Magnetic and microstructural properties of the $BaFe_{(12-(4/3)x)}Sn_xO_{19}$ ceramic system. *Physica*

B: Condensed Matter, 362(1–4), 95-102. doi: http://dx.doi.org/10.1016/j.physb.2005.01.480

Mehmedi, Z., Sözeri, H., Topal, U., & Baykal, A. (2014). Effect of Annealing Temperature and Boron Addition on Magnetic Properties of Hexaferrites Synthesized by Standard Ceramic Method. *Journal of Superconductivity and Novel Magnetism*. doi: 10.1007/s10948-014-2865-9

Meng, P., Xiong, K., Wang, L., Li, S., Cheng, Y., & Xu, G. (2015). Tunable complex permeability and enhanced microwave absorption properties of $BaNi_xCo_{1-x}TiFe_{10}O_{19}$. *Journal of Alloys and Compounds, 628*, 75-80. doi: 10.1016/j.jallcom.2014.10.163

Mu, G., Chen, N., Pan, X., Shen, H., & Gu, M. (2008). Preparation and microwave absorption properties of barium ferrite nanorods. *Materials Letters, 62*(6–7), 840-842. doi: http://dx.doi.org/10.1016/j.matlet.2007.06.074

Nakamura, T., Miyamoto, T., & Yamada, Y. (2003). Complex permeability spectra of polycrystalline Li-Zn ferrite and application to EM-wave absorber. *Journal of Magnetism and Magnetic Materials, 256*(1-3), 340-347. doi: 10.1016/s0304-8853(02)00698-4

Nishikawa, S. (1915). *Proceedings of the Mathematical and Physical Society of Tokyo, 8,* 199-209.

Okamoto, A. (2009). *The invention of ferrites and their contribution to the miniaturization of radios.* Paper presented at the 2009 IEEE Globecom Workshops, Gc Workshops 2009.

Ozah, S., & Bhattacharyya, N. S. (2013). Nanosized barium hexaferrite in novolac phenolic resin as microwave absorber for X-band application. *Journal of Magnetism and Magnetic Materials, 342,* 92-99. doi: 10.1016/j.jmmm.2013.04.050

Pullar, R. C. (2012). Hexagonal ferrites: A review of the synthesis, properties and applications of hexaferrite ceramics. *Progress in Materials Science, 57*(7), 1191-1334. doi: http://dx.doi.org/10.1016/j.pmatsci.2012.04.001

Rado, G. T. (1953). Theory of the microwave permeability tensor and faraday effect in nonsaturated ferromagnetic materials [16]. *Physical Review, 89*(2), 529. doi: 10.1103/PhysRev.89.529

Shams, M. H., Salehi, S. M. A., & Ghasemi, A. (2008). Electromagnetic wave absorption characteristics of Mg-Ti substituted Ba-hexaferrite. *Materials Letters, 62*(10-11), 1731-1733. doi: 10.1016/j.matlet.2007.09.073

Shen, X., Song, F., Yang, X., Wang, Z., Jing, M., & Wang, Y. (2015). Hexaferrite/α-iron composite nanowires: Microstructure, exchange-coupling interaction and microwave absorption. *Journal of Alloys and Compounds, 621*(0), 146-153. doi: http://dx.doi.org/10.1016/j.jallcom.2014.09.181

Singh, P., Babbar, V. K., Razdan, A., Srivastava, S. L., & Goel, T. C. (2000). Microwave absorption studies of Ca-NiTi hexaferrite composites in X-band. *Materials Science and Engineering B: Solid-State Materials for Advanced Technology, 78*(2-3), 70-74. doi: 10.1016/s0921-5107(00)00511-0

Solanki, N., Packiaraj, G., & Jotania, R. B. (2014). Effect of heat treatment on structural, magnetic and electric properties of Z-type barium cobalt hexaferrite powder *Advanced Materials Research* (Vol. 938, pp. 24-29).

Soman, V. V., Nanoti, V. M., & Kulkarni, D. K. (2013). Dielectric and magnetic properties of Mg–Ti substituted barium hexaferrite. *Ceramics International, 39*(5), 5713-5723. doi: http://dx.doi.org/10.1016/j.ceramint.2012.12.089

Sözeri, H., Baykal, A., & Ünal, B. (2012). Low-temperature synthesis of single-domain Sr-hexaferrite particles by solid-state reaction route. *Physica Status Solidi (A) Applications and Materials Science, 209*(10), 2002-2013. doi: 10.1002/pssa.201228023

Sözeri, H., Deligöz, H., Kavas, H., & Baykal, A. (2014). Magnetic, dielectric and microwave properties of M-Ti substituted barium hexaferrites (M=Mn^{2+}, Co^{2+}, Cu^{2+}, Ni^{2+}, Zn^{2+}). *Ceramics International, 40*(6), 8645-8657. doi: 10.1016/j.ceramint.2014.01.082

Sözeri, H., Durmuş, Z., Baykal, A., & Uysal, E. (2012). Preparation of high quality, single domain $BaFe_{12}O_{19}$ particles by the citrate sol–gel combustion route with an initial Fe/Ba molar ratio of 4. *Materials Science and Engineering: B, 177*(12), 949-955. doi: http://dx.doi.org/10.1016/j.mseb.2012.04.023

Sözeri, H., Küçük, İ., & Özkan, H. (2011). Improvement in magnetic properties of La substituted $BaFe_{12}O_{19}$ particles prepared with an unusually low Fe/Ba molar ratio.

Journal of Magnetism and Magnetic Materials, 323(13), 1799-1804. doi: http://dx.doi.org/10.1016/j.jmmm.2011.02.012

Sözeri, H., Mehmedi, Z., Kavas, H., & Baykal, A. (2015). Magnetic and microwave properties of $BaFe_{12}O_{19}$ substituted with magnetic, non-magnetic and dielectric ions. *Ceramics International*. doi: 10.1016/j.ceramint.2015.04.022

Stoppels, D. (1996). Developments in soft magnetic power ferrites. *Journal of Magnetism and Magnetic Materials, 160*, 323-328. doi: 10.1016/0304-8853(96)00216-8

Sürig, C., Hempel, K. A., & Sauer, C. (1996). Influence of stoichiometry on hexaferrite structure. *Journal of Magnetism and Magnetic Materials, 157–158*(0), 268-269. doi: http://dx.doi.org/10.1016/0304-8853(95)01201-X

Tabatabaie, F., Fathi, M. H., Saatchi, A., & Ghasemi, A. (2009a). Effect of Mn-Co and Co-Ti substituted ions on doped strontium ferrites microwave absorption. *Journal of Alloys and Compounds, 474*(1-2), 206-209. doi: 10.1016/j.jallcom.2008.06.083

Tabatabaie, F., Fathi, M. H., Saatchi, A., & Ghasemi, A. (2009b). Microwave absorption properties of Mn- and Ti-doped strontium hexaferrite. *Journal of Alloys and Compounds, 470*(1-2), 332-335. doi: 10.1016/j.jallcom.2008.02.094

Tehrani, M. K., Ghasemi, A., Moradi, M., & Alam, R. S. (2011). Wideband electromagnetic wave absorber using doped barium hexaferrite in Ku-band. *Journal of Alloys and Compounds, 509*(33), 8398-8400. doi: 10.1016/j.jallcom.2011.05.091

Thompson, G. K., & Evans, B. J. (1993). The structure–property relationships in M-type hexaferrites: Hyperfine interactions and bulk magnetic properties. *Journal of Applied Physics, 73*(10), 6295-6297. doi: doi:http://dx.doi.org/10.1063/1.352675

Topal, U. (2011). A simple synthesis route for high quality $BaFe_{12}O_{19}$ magnets. *Materials Science and Engineering B: Solid-State Materials for Advanced Technology, 176*(18), 1531-1536. doi: 10.1016/j.mseb.2011.09.019

Topal, U. (2012a). Improvement of the remanence properties and the weakening of interparticle interactions in $BaFe_{12}O_{19}$ particles by B_2O_3 addition. *Physica B: Condensed Matter, 407*(12), 2058-2062. doi: 10.1016/j.physb.2012.02.004

Topal, U. (2012b). Towards further improvements of the magnetization parameters of B_2O_3-doped $BaFe_{12}O_{19}$ particles: Etching with hydrochloric acid. *Journal of*

Superconductivity and Novel Magnetism, 25(5), 1485-1488. doi: 10.1007/s10948-012-1486-4

Tsutaoka, T., & Koga, N. (2013). Magnetic phase transitions in substituted barium ferrites $BaFe_{12-x}(Ti_{0.5}Co_{0.5})_xO_{19}$ (x=0-5). *Journal of Magnetism and Magnetic Materials, 325*, 36-41. doi: 10.1016/j.jmmm.2012.07.050

Tyagi, S., Verma, P., Baskey, H. B., Agarwala, R. C., Agarwala, V., & Shami, T. C. (2012). Microwave absorption study of carbon nano tubes dispersed hard/soft ferrite nanocomposite. *Ceramics International, 38*(6), 4561-4571. doi: 10.1016/j.ceramint.2012.02.034

Wejrzanowski, T., Pielaszek, R., Opalińska, A., Matysiak, H., Łojkowski, W., & Kurzydłowski, K. J. (2006). Quantitative methods for nanopowders characterization. *Applied Surface Science, 253*(1), 204-208. doi: http://dx.doi.org/10.1016/j.apsusc.2006.05.089

Wohlfarth, E. P. (1958). Relations between Different Modes of Acquisition of the Remanent Magnetization of Ferromagnetic Particles. *Journal of Applied Physics, 29*(3), 595-596. doi: doi:http://dx.doi.org/10.1063/1.1723232

Xu, G., Ma, H., Zhong, M., Zhou, J., Yue, Y., & He, Z. (2006). Influence of pH on characteristics of $BaFe_{12}O_{19}$ powder prepared by sol–gel auto-combustion. *Journal of Magnetism and Magnetic Materials, 301*(2), 383-388. doi: http://dx.doi.org/10.1016/j.jmmm.2005.07.014

Yang, Z., Wang, C. S., Li, X. H., & Zeng, H. X. (2002). (Zn, Ni, Ti) substituted barium ferrite particles with improved temperature coefficient of coercivity. *Materials Science and Engineering B: Solid-State Materials for Advanced Technology, 90*(1-2), 142-145. doi: 10.1016/s0921-5107(01)00925-4

Zhong, W., Ding, W., Zhang, N., Hong, J., Yan, Q., & Du, Y. (1997). Key step in synthesis of ultrafine $BaFe_{12}O_{19}$ by sol-gel technique. *Journal of Magnetism and Magnetic Materials, 168*(1–2), 196-202. doi: http://dx.doi.org/10.1016/S0304-8853(96)00664-6